2-24-2024

Mechanisms of Electrical Substrate Reprogramming after Cardiac Radiotherapy

David Meng Zhang
Washington University in St. Louis

WASHINGTON UNIVERSITY IN ST. LOUIS

Division of Biology and Biomedical Sciences
Molecular Cell Biology

Dissertation Examination Committee:
Stacey Rentschler, Chair
Charles Kaufman
Jeanne Nerbonne
David Ornitz
Julie Schwarz

Mechanisms of Electrical Substrate Reprogramming after Cardiac Radiotherapy

by

David Meng Zhang

A dissertation presented to
Washington University in St. Louis
in partial fulfillment of the
requirements for the degree
of Doctor of Philosophy

May 2024
St. Louis, Missouri

Table of Contents

List of Figures

List of Tables

Acknowledgements

This dissertation is dedicated to everybody who has guided and influenced my journey along the way. To my undergraduate mentor, Carlo Bartoli, thank you for your guidance at the start of my academic career. Your early lessons on experimental design, hypothesis-testing, grantsmanship, and responding to reviewers have been invaluable through this phase of my development. To my doctoral advisor, Stacey Rentschler, thank your thorough guidance and attention throughout my training. The opportunities and exposures you provided me with, from invited speaker-level talks to grant submissions and resubmissions, has greatly accelerated my academic growth. To members of my thesis committee, Charles Kaufman, Jeanne Nerbonne, David Ornitz, and Julie Schwarz, thank you for providing valuable input and feedback over the course of my doctoral research. To past and present members of the Rentschler lab, thank you for providing an encouraging and supportive academic environment. I am grateful for everyone's willingness to help with and teach new techniques in the lab, and I will miss our frequent scientific discussions over coffee or free food. To my friends in St. Louis, I am grateful for our time spend together outside of the lab. To old friends from college and high school, thank you for making time catch up in-person and virtually. To my parents, thank you for your patience and support throughout my life. To my wife, Louisa Bai, I am so grateful for your unwavering love and support. You inspire me every day with your passion and hard work, and I am excited for what to future has in store for us.

David M. Zhang

Washington University in St. Louis

May 2024

ABSTRACT OF THE DISSERTATION

Mechanisms of Electrical Substrate Reprogramming After Cardiac Radiotherapy

by

David Meng Zhang

Doctor of Philosophy in Biology and Biomedical Sciences

Molecular Cell Biology

Washington University in St. Louis, 2024

Professor Stacey Rentschler, Chair

Ventricular tachycardia (VT) is frequently associated with morbidity in patients with heart disease and can lead to sudden cardiac death, which accounts for over 350,000 deaths per year and nearly half of all cardiovascular-related deaths in the United States. Despite its status as a major public health concern, arrhythmia management strategies are severely limited in safety and efficacy. Standards-of-care include defibrillators, anti-arrhythmic drugs, and/or ablations. Implantable cardioverter defibrillators improve survival in at-risk populations but severely reduce quality-of-life and increase risks of further-declining ventricular function. Pharmacologic interventions are limited in efficacy and have dozens of off-target effects which are major sources of morbidity and mortality. Invasive radiofrequency catheter ablations frequently fail due to anatomical factors or limitations in the physics of heat transfer to create full-thickness, gap-free ablations.

Radiotherapy is a modern oncologic intervention that uses photon beams to deliver high-dose radiation, precisely and noninvasively, to any target tissue in the body. Hypothetically, ablative doses of radiation to the heart could noninvasively replicate the effect of CA, with a fibrotic response expected over months to years. Early preclinical studies that explored

radiobiology for arrhythmia treatment attempted to create ablative scar by inducing mitotic catastrophe, apoptosis, and fibrosis. In these models, extremely high doses ranging from 40-160 Gy to the myocardium were sufficient to produce moderate fibrosis over a period of several months, while lower doses and earlier timeframes doses did not achieve these effects. Recent clinical evidence has demonstrated the safety and efficacy of cardiac radiotherapy for treatment of drug-refractory VT in humans. In 2017, the first case series of cardiac RT reported a 99.9% reduction in patient VT burden after only 25 Gy radiation. A subsequent 2020 prospective Phase I/II clinical trial of 19 reported a 94% reduction in episodes of VT or premature ventricular contractions after 25 Gy in patients who had either previously failed or were not eligible for CA. Several studies have now replicated these clinical results at multiple independent medical centers. In nearly all cases, VT reduction occurred within days to weeks; thus, the onset of VT reduction is inconsistent with expected and reported timeframes of radiation-induced fibrosis. As such, the mechanisms by which 25 Gy radiation sub-acutely reduces VT are unknown. In the setting of heart disease, structural and electrical heterogeneity promote areas of slow conduction in surviving myocardium, which subsequently lead to electrical reentry from delays in impulse prorogation longer than the effective refractory period. Although radiation was presumed to prevent VT by creating radiation-induced fibrosis to homogenize scar, the anti-arrhythmic effects preventing reentry could potentially be mediated through effects on enhancement and restoration of electrical conduction.

Herein, I first asked whether radiation-induced fibrosis is an important radiobiologic effect in patients. Using post-mortem or explanted patient specimens previously treated with 25 Gy, I observed that radiation does not replicate the fibro-ablative effects of thermal catheter ablation. Irrespective of specimen fibrosis, all patients exhibited suppression of VT within 1 month of

treatment. As a follow-up, I tested a small animal model of 25 Gy cardiac radiation and detected no evidence gross fibrosis on histology or collagen deposition at 6 weeks post-treatment. To test fibrosis-independent effects of radiation to the post-mitotic heart, I evaluated murine cardiac electrophysiology and molecular biology after radiotherapy. Within 6 weeks post-treatment, irradiated hearts exhibited enhanced electrophysiologic properties on electrocardiogram and voltage optical mapping, attributed to observed upregulations in the cardiac sodium channel $Na_V1.5$ and the gap junction subunit connexin 43. These effects were observed to occur at doses as low as 15-25 Gy and persisted for a minimum of 42 weeks, akin to an electrical reprogramming of the conducting substrate. I further demonstrated that reprogramming occurs primarily in surviving border zone myocardium and not scar myofibroblasts using a surgical model of myocardial infarction. To understand cell signaling mechanisms that may contribute to these effects, I utilized unbiased RNA sequencing of the irradiated murine ventricle and observed reactivation of the Notch signaling pathway in adult cardiomyocytes as a potential mechanistic contributor. Using an adult-inducible, cardiomyocyte-specific murine model of Notch activation, I demonstrated that transient reactivation of Notch signaling in adult left ventricles alone is sufficient to upregulate $Na_V1.5$ for at least 1 year, and these effects correlated with persistently increased conduction velocities. To test whether Notch signaling is also necessary for conduction reprogramming, I utilized an adult-inducible Notch loss-of-function transgenic mouse model that reduced the overall effect size of conduction velocity reprogramming and $Na_V1.5$ upregulation by 30%. Assessment of cardiomyocyte nuclei and genome accessibility revealed larger nuclear sizes in the absence of changes to DNA content, as well as chromatin compaction of cardiomyocyte DNA at 48 hours post-treatment.

Within this dissertation, I demonstrate that cardiac radiotherapy regulates and reprograms cardiomyocyte electrophysiology without ablative fibrosis in human and mouse models. Herein, I further discuss therapeutic strategies for electrically-reprogramming ventricular cardiomyocytes to prevent reentry and tachycardia. Indeed, insights in cardiomyocyte radiobiology such as those presented within this dissertation are expected to lead to improvements and refinement in the cardiac radiation protocol, wider adoption of this emerging treatment technique, and potential expansion of therapy into greater arrhythmia populations.

Chapter 1: Introduction

1.1 Overview of cardiovascular disease and ventricular arrhythmias

Heart disease is a leading cause of death in the world[1]. For patients with cardiovascular disease, ventricular arrhythmias are a primary source of morbidity and mortality. These arrhythmias, characterized by an irregular rate and/or rhythm of the heart, encompass a spectrum of disorders that range from premature ventricular complexes to ventricular tachycardia (VT) and fibrillation (VF). Indeed, ventricular arrythmias arise from several etiologies of ischemic and nonischemic cardiomyopathies. In the setting of impaired cardiac function and structural heart disease, structural and/or electrical remodeling of the heart produces a pathologic conduction substrate, leaving patients at greater risk for ventricular arrhythmias. Left unchecked, VT progresses to VF, sudden cardiac arrest, and sudden cardiac death, which account for an estimated 350,000 deaths per year and approximately 50% of all cardiovascular deaths in the United States[2].

1.2 Heart rhythm and the cardiac conduction system

Normal heart rhythm propagates through a functional cardiac conduction system, which consists of a series impulse-propagating tissues and nodes, to orchestrate coordinated contraction and relaxation of the myocardium at a physiologic rate. These excitation-contraction cycles subsequently allow for maintenance of blood pressure and perfusion to the body. The coordinated cycles occur through rapid propagation of electrical signal at high conduction velocities, enabled

the myocardium's expression of voltage-gated sodium channels, responsible for depolarization of the cell, and gap junctions, which consist of hemichannels of connexin proteins that allow for passive diffusion of charge to neighboring cells. The conduction system can be further subdivided into pacemaker cells, including the sinoatrial and atrioventricular nodes, rapidly conducting fibrous networks, such as the His bundles and Purkinje fibers, and cardiomyocytes. Hence, cardiac arrhythmias may arise in the setting of structural or functional alterations to any of these cell types. In the heart, VT refers specifically to 3 or more arrhythmic beats of ventricular origin, at a rate greater than 100 beats per minute, may result in hemodynamic instability, and is frequency associated with structural heart disease and cardiomyocyte dysfunction.

1.3 Mechanisms of scar-related VT and electrical reentry

Indeed, propagation of sinus rhythm depends on uniform depolarization and repolarization of the myocardium that leads to a single systolic-diastolic cycle (**Figure 1.1A**). VT often arises in the setting of heart disease that causes pathologic changes to conduction, for example in the setting of post-infarct scar[3,4]. These pathologic changes are arrhythmogenic by causing premature triggers, aberrant automaticity, and reentry. While triggers and altered automaticity are often responsible for VT in the setting of acute ischemia, electrical reentry is the primary mechanism of chronic, scar-related VT[4,5].

The presence of structural and/or electrical heterogeneity in the heart increases the probability of unidirectional block[6], self-sustaining electrical reentry[7], and tachycardia after a premature stimulus (**Figure 1.1B**)[8]. Due to cellular repolarization and sodium channel gating kinetics, all cardiomyocytes exhibit a post-excitatory effective refractory period (ERP), defined as the

maximum interval of time after depolarization that prevents further propagation of a premature stimulus through the tissue (**Figure 1.1B**, top). The ERP thus serves as an evolutionarily-conserved mechanism to coordinate excitation-contraction cycles and protect against arrhythmias. However, reentrant tachycardias often occur in the presence on slowly-conducting channels of surviving cardiomyocytes within scar that allow for delays in impulse propagation that become longer than the ERP of the myocardium[5]. Conduction delays subsequently cause an electrical impulse to re-excite the ventricular substrate once it traverses the path of conduction (**Figure 1.1B**, bottom). This phenomenon requires the distance traveled while the myocardium is refractory, defined as the wavelength and determined by the mathematical product of the ERP and conduction velocity (CV), to be shorter than the length of the circuit. Hence, the presence of long, tortuous conduction pathways, fast repolarization, and slow delayed CV all predispose to reentry and VT.

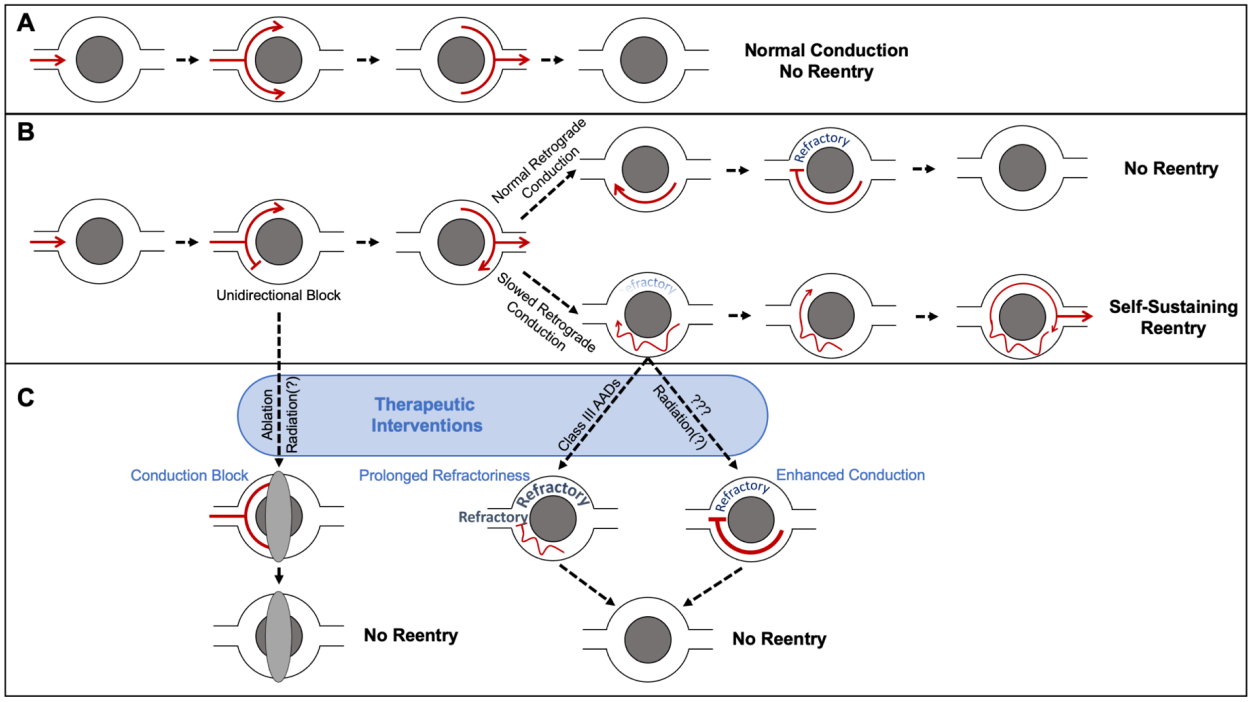

Figure 1.1 Mechanisms of scar-related VT and therapies. (A) Normal Conduction, no reentry. As the electrical impulse travels down the conduction path, the impulse uniformly excites distal

myocardium. **(B)** Unidirectional Block, Normal versus Slowed Retrograde Conduction. As the electrical impulse splits, one branch exhibits unidirectional block (for example, due to dispersion of refractoriness) while the other branch propagates distally. As the impulse travels distally, there is for retrograde conduction through the previously blocked branch. Top: In normal retrograde conduction, electrical impulses rapidly propagate to proximal myocardium that is still refractory, and conduction terminates. Bottom: In the setting of slowed retrograde conduction, the proximal myocardium is allowed time to repolarize, providing a window to re-excite proximal tissue and forming a self-sustaining, reentrant circuit. **(C)** Therapeutic strategies to prevent reentry through conduction block, prolonged refractoriness, and enhanced conduction. Abbreviations: AADs = antiarrhythmic drugs.

1.4 VT clinical treatments and mechanisms of action

Given the physiologic and structural conditions required to sustain electrical reentry, existing therapeutic strategies to prevent reentrant arrhythmias are as follows (**Figure 1.1C**): (1) identify and eliminate slow-conducting pathways within scar, as in the case of radiofrequency catheter ablations (CAs)[9]; (2) prolong the refractory period of the pathologic, slow-conducting substrate, as in the case of Class III antiarrhythmic drugs (AADs)[9,10]; or (3) enhance the conduction properties of conducting myocardium[5].

Invasive radiofrequency CAs allow for electroanatomical mapping of regions of electrical reentry within scar and subsequent delivery of ablative thermal energy to homogenize scar and eliminate reentrant circuits. However, CA is time consuming, technically challenging, and highly operator dependent. Rates of acute VT cessation and durable control are high in favorable patients treated

for the first time with adequate ventricular function and/or ischemic cardiomyopathy with focal scar[11]. However, success rates are considerably lower for patients with severely decreased ejection fraction, diffuse VT substrates, prior CA attempts, or deep reentrant circuits[12,13]. Overall, nearly half of all first-time CA patients experience some VT recurrence[9]. CA treatment failures are partly attributed to anatomical factors and to the properties of heat transfer physics to create a full-thickness, gap-free ablation[12–14].

Class III AADs, which act through inhibition of repolarizing potassium currents to prolong the action potential duration, attempt to prolong the ERP of the conducting substrate to terminate a propagating reentrant impulse. Overall, class III AADs have only modest efficacy and considerable side effects, including pulmonary fibrosis, liver disease, and paradoxical arrhythmias, which become additional sources of morbidity and mortality in these sick patient populations.

To date, there are no approved VT therapies that act through restoration or enhancement of cardiomyocyte conduction. If VT remains uncontrolled, use of implantable cardioverter defibrillators (ICDs) improve survival in at-risk populations, but at the extreme costs of reduced quality-of-life from shocks and the potential for worsening heart failure.

1.5 Radiation therapy (RT) as potential treatment for VT

Radiation therapy (radiotherapy, RT) is a technique that allows for precise delivery of high-dose radiation energy to volumes of target tissue anywhere in the body, with minimal exposure of surrounding tissue, and is standard-of-care with either curative or palliative effects in the treatment of several malignancies.

Ionizing RT has several acute and delayed effects actively dividing tissues. High-dose radiation results in direct damage to DNA and subcellular structures[15]; moreover, radiation induces indirect damage through radiolysis of water to produce reactive oxygen species (ROS)[16]. These highly unstable ROS subsequently cause oxidative stress and cell toxicity via lipid peroxidation, protein misfolding, and DNA damage[16]. Conventional RT is given in relatively small doses (≤2 Gy, or J/kg) over several weeks. However, the advent of stereotactic body RT has allowed for delivery of radiation energy to tissues with high-precision and specificity in one or more fractions, resulting in strong tumor ablative effects. Indeed, non-invasive deliver of high-dose stereotactic body RT to a specific volume of target tissue in the heart may be technically-favorable to treat VT quickly and precisely in patients, potentially circumventing longstanding limitations in accessibility or treatment depth posed by catheter-based approaches Theoretically, ablative doses of focused radiation to cardiac scar could replicate the desired effect of CA in a noninvasive manner, with a fibrotic response expected over many months to years.

Recent clinical evidence has demonstrated the safety and efficacy of cardiac RT for treatment of drug-refractory VT in humans[17–19]. After case reports of successful VT management with cardiac RT in 2014[20,21], the first case series reported that, in combination with electrophysiologic mapping, 25 Gy ionizing radiation delivered in a single fraction to arrhythmogenic foci of the heart led to a 99.9% reduction of VT burden. Interestingly, this antiarrhythmic effect was observed to occur within as early as a 6-week post-treatment blanking period[17] and persisted for at least 12 months. More recently, the first and only prospective phase I/II trial of stereotactic body RT for treatment of refractory VT, which included 19 patients, reported a 75% reduction in VT burden in 89% of

the patients and a 72% survival rate after 12 months in this high-risk population[18]. In these patients, the number of ICD shocks administered were also decreased from a median of 4 per month to a median of zero, suggesting improved quality of life.

With several dozens of patients treated globally, management of VT after 25 Gy irradiation has now been replicated across several independent medical centers[19,22–26]. These result have also suggested that cardiac RT is uniquely effective at treating VT in the setting of both ischemic and nonischemic cardiomyopathies, including refractory VT secondary to nonischemic dilated cardiomyopathy[20,24], arrhythmogenic right-ventricular cardiomyopathy[17,18,23], and unresectable cardiac fibroma[25] and lipoma[26]. While most patients continue to experience the clinical benefits of reduced VT burden and improved quality of life at least 2 years after treatment[19,27], overall rates of VT recurrence have varied across all studies and reports, and a recent prospective study reported the highest rate of VT recurrence in 5 of 5 patients, which occurred within 1-year post-treatment after initial reductions in VT burden[28]. Collectively, these early clinical results suggest that 25 Gy radiotherapy is sufficient to control VT episodes after a post-irradiation blanking period, and additional preclinical and clinical studies are warranted to better define the mechanisms and durability of this clinical effect.

Although the efficacy of this new approach for arrhythmia management is presumed to depend on late-effects of radiation-induced fibrosis to ablate conducting tissues, the precise mechanisms that contribute to its effectiveness are still unknown, especially at doses of radiation prescribed clinically. Since radiation-induced fibrosis is observed to occur gradually over the course of several months[29], the rapid and significant reductions in VT observed within of days[24] to

weeks[17,18,21] of treatment suggests alternative radiobiologic effects occurring within earlier timeframes to reduce arrhythmia burden.

Post-mortem histopathologic examinations of cardiac RT specimens have provided some insight into potential radiobiologic mechanisms of interest. In a single patient who expired from a fatal stroke at 3 weeks post-treatment, assessment of radiation-targeted myocardium on autopsy showed small-vessel ectasis at the interface of ischemic scar and myocardium, but no evidence of myocardial inflammation, acute necrosis, or fibrosis[17]. Another report that included three patient specimens described the presence of endothelial vacuolization, edematous mitochondria, and disruption of the intercalated discs in the targeted myocardium that occurred within 11-days post-treatment[30]. These observations may suggest some role for vascular injury and/or myocardial remodeling after radiation. Nevertheless, although patchy fibrosis is noted in histologic examinations of nearly all myocardial specimens[30], it is difficult to discern whether these observed fibrotic regions are due to the radiation treatment itself or from pre-existing fibrosis in the setting of scar-related VT. Overall, there remains a lack of evidence among post-radiation human cardiac specimens to demonstrate that the antiarrhythmic effects of RT occur through CA-like destruction of conducting tissues.

1.6 Preclinical effects of radiotherapy on cardiac fibrosis

To methodically investigate this emerging VT management strategy, several preclinical animal studies using cardiac RT have explored its potential mechanisms of action to decrease arrhythmias. In contrast to humans, where nearly all treatment targets were prescribed to the ventricles, preclinical studies have targeted multiple sub-cardiac structures, including the ventricles,

atrioventricular (AV) nodes, and the pulmonary veins to delineate location-dependent effects of single-fraction radiation on cardiac fibrosis and electrophysiology. Below, I discuss current preclinical findings on the effects of radiation on cardiac fibrosis, conduction block, and electrophysiologic conduction, as well as each mechanism's anticipated role in arrhythmia management.

Early preclinical studies that tested the feasibility of RT as noninvasive arrhythmia therapy hypothesized that high-dose, single-fraction cardiac RT was sufficient to cause cell death[31,32], radiation-induced fibrosis[31–36], and produce electrically inert tissue[37,38] comparable to CA-induced scar (**Figure 1.1C,** Conduction Block). This hypothesis drew parallels from the biology of tumor cell death after radiation, which is well-characterized and attributed, in-part, to senescence[39,40] and/or mitotic catastrophe and cell death[40–42] after oxidative stress and widespread DNA double-stranded breaks. Following acute cell death, fibroblast recruitment and activation leads to extracellular matrix deposition and scar. In addition, RT was associated with late-stage fibrosis in noncancerous tissues receiving incidental radiation exposure[43]. Importantly, in contrast to the wealth of existing literature on tumor radiobiology, the heart consists of vast populations of nondividing, post-mitotic cardiomyocytes which may exhibit increased radioresistance and distinct radiobiologic responses following DNA repair.

Preclinical studies that produced structural ablative lesions in the heart utilized doses in the range of 30-55 Gy to induce moderate-to-severe, but not necessarily full-thickness, fibrosis in the atrioventricular node[44–47], pulmonary veins[44,48–50], and ventricles[44,47,51] over a 6- to 24-month period. Independent of location, doses in excess of 40 Gy robustly fibrotic, nonconducting lesions

after 6 months[44,47,49–51]. Of note, these dose ranges are substantially higher than the 25 Gy dose described clinically (**Figure 1.2**), and timing of these fibrotic responses in animals[36] occured later than the observed clinical benefit in patients[19,22–26]. Indeed, while myocardial fibrosis is observed to develop on the timescale of months to years, the clinical reductions in VT burden after cardiac RT are observed within days to weeks, with additional rare case reports of acute rescue from VT storm[24,52] after cardiac RT. Several studies have since noted that the observation of antiarrhythmic effect occurs before fibrosis is expected and suggest that the therapeutic effects of radiotherapy cannot be attributed to fibrosis alone[24,28,30].

Outside of RT for arrhythmia management, myocardial fibrosis was studied in the context of cardiotoxicity and radiation-induced heart disease[53–56] after thoracic tumor radiotherapy[29,57,58]. The late effects of radiation-induced heart disease, including myocardial fibrosis, often manifest decades after thoracic tumor radiation and may be due to a variety of pathophysiologic processes[59,60]. These pathways may include radiation-induced vascular injury[61], thrombosis[62,63], myofibroblast activation, collagen deposition[33], myocardial ischemia, and cell death[53]. Following radiation, many pro-fibrotic cytokines and factors are implicated in the development of radiation-induced fibrosis[33]. Specifically, local secretion of transforming growth factor beta 1 (TGF-β1) and downstream TGF-β1/CTCF/Smads[31,64] signaling induces proliferation of collagen-producing, matrix-depositing myofibroblasts and has been described as an important mediator of myocardial fibrosis after radiation[65]. However, studies that chart the activation of these pro-fibrotic pathways in conjunction with the antiarrhythmic effect after cardiac RT are necessary to clarify the role of fibrosis in this emerging therapy.

1.7 Radiation effects on conduction block

In the absence of fibrosis, several phenotypic changes have been observed in a subset of clinical and preclinical studies, including the presence of vacuolar degeneration[30,36,46,66], nuclear atypia[17], necrosis[30], cell-junction disruption[30,66], immune cell infiltrates[46,66], and microvascular hemorrhaging[46]. These phenotypic changes are presumed result in corresponding physiologic consequences. As an alternative to structural fibrosis and scar, a functional ablation may be achieved through acute and prolonged disruption of cardiomyocyte electrical conduction without cell death. Such an effect has been observed in large animal models, but only at extremely high-dose (in excess of 100 Gy) treatments to the atrioventricular node, that immediately produced complete atrioventricular block[67,68].

The precise biology behind radiation-induced functional ablation is unclear but may be attributed to some combination of oxidative stress, mitochondrial dysfunction[30,69,70], endoplasmic reticulum dysfunction[32,71,72], inflammation[33,66,73], and/or dysregulated intercellular coupling[30,66]. Excessive ROS production after radiotherapy can alter mitochondrial membrane stability, create local redox imbalances, and cause substantial mitochondrial dysfunction and genomic instability. While long-term mitochondrial dysfunction may lead to cytochrome *c* release and induction of apoptosis[66,74,75], as evidenced by the detection of caspase-3 in porcine ventricles treated with >30 Gy after 12-16 weeks[47], short-term dysfunction may cause an acute conduction block in highly-metabolic cardiomyocytes. These potential mechanisms may be consistent with several of the phenotypic changes described to-date, and the progression from these subacute observations to collagen deposition and scar formation is still under investigation[47].

Radiation causes chronic interruptions in electric conduction in the dose ranges of 20-55 Gy[44,45,48,50,66,75–78], and robust conduction block was consistently observed at higher dose ranges **(Figure 2)**. Yet, these observations are primarily reported in studies that targeted the AV node and pulmonary vein. Whether delivery of 25 Gy to the ventricles, which is the most common dose used clinically, produces complete conduction block effect remains unclear. More recently, 25 to 35 Gy-equivalents (GyEs) of carbon and proton beam radiation to rabbit left ventricles were reported to produce apoptosis, mild fibrosis, and accompanying conduction delay by 3 and 6 months[75]. To-date, only one large-animal study has reported a complete functional conduction block in the left ventricle, and these regions were treated with 40 Gy[44].

1.8 Gap junction remodeling after cardiac radiation

Dysregulation and/or dysfunction of cardiac conduction are common in the setting of heart disease and arrhythmias[79–81], and these derangements result in local decreases to conduction velocity and subsequently create arrhythmogenic substrates **(Figure 1.1B)**. Conversely, therapies which improve or enhance conduction protein function and expression are expected to restore electrical conduction and prevent re-entry[82,83] (**Figure 1.1C,** Enhanced Conduction). Large animal studies have already demonstrated that this therapeutic approach has a strong antiarrhythmic effect[84–86]. Indeed, adenoviral-mediated upregulation of skeletal muscle sodium channel SkM1[86,87] and Cx43[85] to infarcted canine and porcine hearts, respectively, reduced ventricular arrhythmia inducibility by locally increasing conduction velocity to prevent electrical reentry. However, there are currently no clinically-available VT therapies that are known to act through increasing local conduction.

A unique radiobiologic effect previously observed in cancer therapy is the increase in intercellular communication and gap junction formation after radiation to a variety of cell and tissue types[65,88–93]. Gap junctions play important roles in a variety of cellular functions, including intercellular communication, cell adhesion, signal transduction, and homeostasis[79,94]. Although the mechanism of post-irradiation upregulation of gap junctions is unclear, this effect is presumed to increase functional intercellular coupling, including electrical coupling[95], and play a role in the radiation bystander effect[96–100].

Preclinical studies that explored the phenomenon of radiation-induced cellular coupling for arrhythmia management hypothesized that this radiobiologic effect may upregulate functional gap junctions in the heart to increase electrical coupling and conduction velocity[95]. These studies showed that heavy ion radiation, as low as 10-25 Gy, was sufficient to increase expression[92,93,95,101,102] and lateralization of connexin 43 (Cx43, the major ventricular gap junction subunit)[95,101,102], increase local conduction velocity[95], and homogenize substrate repolarization[95,102]. These changes were detected within 2 weeks post-treatment[95,101] and lasted for a minimum of 1 year[101,102]. Furthermore, these studies showed that radiation-induced upregulation of Cx43 was associated with decreased inducibility of ventricular arrhythmias in rabbit[95] and dog[102] infarct models. Importantly, these electrophysiologic changes were observed in the absence of radiation-induced fibrosis. The observed effect of conduction protein upregulation on reducing VT inducibility is supported by previous studies that demonstrated an antiarrhythmic effect after cell- or adenoviral-mediated overexpression of cardiac conduction proteins, including Cx43, in several animal models [84,85,87]. However, higher-dose proton and carbon ion studies (25-35 GyE) have shown decreases in relative Cx43 expression after radiation [48,75], although these effects may

occur secondary to observed increases in fibrosis and decreases in cardiomyocytes [48,75]. The potential pro-conductive effects of radiotherapy, in the absence of observed functional conduction block and prior to an expected fibrosis response, may explain mechanisms of both acute and persistent antiarrhythmic benefits conferred to refractory VT patients after treatment with doses in the range of 25 Gy after gamma radiation. Additional studies are required to explore the effects of conduction protein upregulation in cardiomyocytes and further understand the mechanisms of electrical conduction reprogramming after cardiac RT.

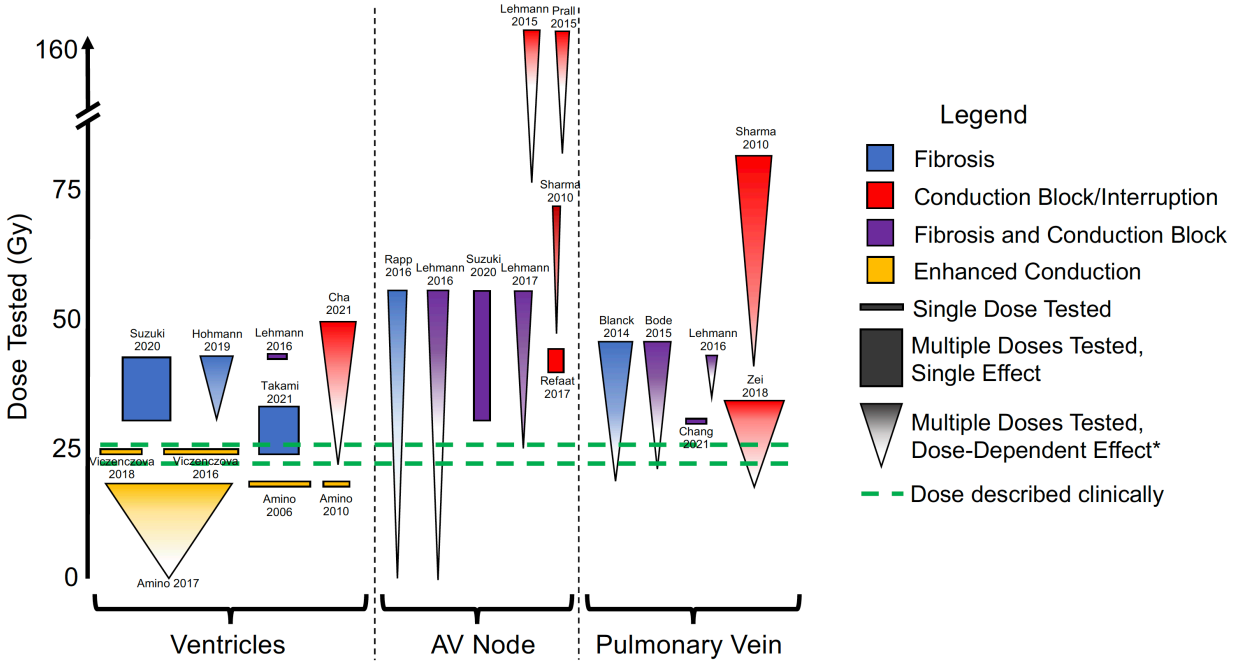

Figure 1.2. Preclinical cardiac radiobiology effects previously described. Dose-dependent cardiac radiobiologic effects on fibrosis (blue), conduction block/interruption (red), fibrosis plus conduction block (purple), and enhanced conduction (yellow) described in preclinical studies. Effects are further stratified by tested tissue types (ventricles, AV node, pulmonary vein). Studies are identified by Reference number in the text/References section. Symbol widths reflect the relative study-size for each preclinical study. Solid Line: single dose tested; Solid Rectangle:

multiple doses tested, single effect observed; Gradient Triangle: multiple doses tested, dose dependent response. *Whited-out regions of triangle gradients denote pertinent negative observations. The dose range described clinically that is associated with substantial VT reduction is highlighted by the dashed green lines for comparison. Abbreviations: AV = atrioventricular.

1.9 Notch signaling in the radiation response

Existing clinical and preclinical data suggest that the antiarrhythmic effect of RT may not primarily be attributed to a fibrosis effect at the doses (of 25 Gy) and timeframes (weeks) described clinically. Ample preclinical data suggests that achieving dense, fibrotic lesions that mimics clinical CA is possible with cardiac RT, but this biologic endpoint likely requires ablative doses in excess of 40 Gy and timescales in excess of several months. A clinical study previously noted that 25 Gy may result in underdosing to achieve tissue destruction[28]. Instead, cardiomyocytes survive in the long term in a post-radiation state. To explore the potential interplay between the radiation response and cardiac biology, sections within this dissertation investigate the role of cardiac Notch signaling, an evolutionarily-conserved developmental signaling pathway implicated in cardiac development and the radiation response. Importantly, an emerging paradigm in cancer cell research directly implicates Notch in the DNA damage response. In the setting of radiation-induced endoplasmic reticulum oxidative stress, Notch1 upregulation conferred cellular protection from apoptosis in glioblastoma cells[103,104]. Indeed, Notch signaling has been reported to activate in a variety of tissue types after radiation[105–107], including tumor vasculature[107], breast cancer stem cells[106,108], and non-small cell lung cancer[104]. Whether Notch is reactivated in adult cardiomyocytes after 25 Gy radiotherapy remains unknown.

Notch signaling acts via a juxtracrine mechanism to drive cell fate, renewal, and proliferation decisions. In mammals, Notch signaling involves a family of Jagged (Jag) or Delta-like (Dll) ligands (Jag1, Jag2, Dll1, Dll3, and Dll4) presented by signal sending cells and a family of Notch receptors (Notch1, Notch2, Notch3, and Notch4) present on signal-receiving cells. Upon ligand-receptor interaction, Notch signal transduction occurs via proteolytic cleavage of the Notch intracellular domain (NICD) of any Notch receptor and its translocation to the nucleus, where it binds to transcriptional coactivators to elicit direct and indirect Notch-mediated effects. To induce downstream effects, the NICD must interact with a family of transcriptional coactivators necessary for formation of a functional DNA-binding complex to activate Notch-specific transcription. These transcriptional co-activators include the DNA-binding protein CSL, the MAsterMind-Like protein 1 (MAML1), and the histone acetyltransferase P300. Though there is potential for several unique Notch ligand to receptor-binding interactions, there is little to no evidence to suggest that specific ligand-receptor combinations yield distinct downstream effects, and previous studies have demonstrated that the NICDs of different Notch receptors yield the same effects. Instead, Notch related target genes are highly dependent upon cell state and cell type at the time of Notch activation[109–112].

1.10 Notch signaling in the developing and adult hearts

In the heart, Notch signaling drives cardiogenic fate decisions during development[113,114]. Several studies have now demonstrated that early perturbation to members of the Notch signaling pathway during heart development, including ligands, receptors, and transcriptional co-activators, lead to congenital heart defects[115,116] or early embryonic death[117,118]. In addition to its structural effects, Notch signaling plays an important role in conduction system development, where embryonic

overexpression of Notch signaling promotes ectopic expression of cardiac conduction tissue at the atrioventricular junction akin to the accessory conduction pathway that leads to ventricular preexcitation in Wolff-Parkinson-White syndrome[119]. Importantly, overexpression of cardiomyocyte Notch signaling during development was shown to drive changes in both gene expression and electrophysiology to resemble the phenotype of Purkinje cells of the cardiac conduction system[111,120].

Though it is dynamically activated during heart embryogenesis and conduction system development, Notch signaling becomes quiescent in post-mitotic, adult mammalian cardiomyocytes[121]. Recent evidence has suggested that Notch reactivation in the adult heart may occur in response to cardiac injury[111,121–125]. For example, Notch activation after cardiac injury in (nonmammalian) zebrafish induces proliferation of differentiated cardiomyocytes to allow for post-injury regeneration[124,125]. In mammals, however, Notch reactivation in cardiomyocytes may improve cell survival and cardiac function in the absence of cell proliferation. Recent evidence has suggested that Notch reactivation in the adult heart confers electrophysiologic changes. In the adult atrial chambers, transient induction of Notch signaling atria was associated with long-term electrical reprogramming effects[126]; furthermore, Notch was differentially upregulated in left atrial cardiomyocytes in the setting of atrial fibrillation in humans[112]. Importantly, the electrophysiologic effects of reactivation of Notch in the adult mammalian ventricles is unknown.

1.11 Objective of the Dissertation

Since cardiac RT first emerged as a noninvasive, treatment option for VT management, preclinical and clinical studies focused primarily on its "ablative" effect, based on a wealth of existing literature on tumor radiobiology. Although radiation-induced DNA damage causes cell death in rapidly-dividing tumor cells, post-mitotic cells are relatively radioresistant due to their capacity for DNA repair through non-homologous end joining[127]. Adult cardiomyocytes are post-mitotic and senescent, and thus resistant to classic mechanisms of cell death after DNA damage. Overall, the effects of RT on adult, mammalian cardiomyocytes remain uncharacterized. Defining these effects are expected to provide insight to how single-fraction cardiac RT reduces VT. Though radiation has been presumed to stop VT by creating radiation-induced fibrosis in arrhythmogenic scar, its antiarrhythmic properties may be mediated through effects on conduction. Within this dissertation, I evaluate cardiac radiobiology effects after ionizing on the mammalian ventricle to define mechanisms of electrical substrate reprogramming after DNA damage. I test whether the 25 Gy dose of radiation, used clinically in most studies to date, was sufficient to achieve catheter ablation-like scar in explanted patient samples. In humans and adult mice, I explore whether ionizing radiation increases levels of cardiac conduction proteins and enhances ventricular conduction and whether these lead to durable transcriptional and epigenetic changes. Through gain- and loss-of-function approaches, I identify cardiomyocyte Notch signaling as a potential mechanism whereby radiation may reprogram conduction. Furthermore, I present evidence to suggest that radiotherapy influences cardiomyocyte nuclear structure and chromatin dynamics. Additionally, I present of electrical substrate reprogramming after radiation in VT patients. Herein, I discuss therapeutic strategies for reprogramming ventricular cardiomyocytes to a pro-conduction phenotype to prevent electrical reentry.

Chapter 2: Cardiac Radiotherapy Effects on Patient Histopathology and VT

2.1 Single-fraction radiation does not increase cardiac fibrosis in patients, despite marked decreases in VT burden

I first investigated the association between radiation and cardiac fibrosis in 4 VT patients who received cardiac RT and provided heart specimens after death or heart transplant (**Table 2.1**). Specimens targeted with 25 Gy radiation were stained with Masson's trichrome to visualize fibrosis and compared with nontargeted remote specimens within the same hearts (**Figure 2.1a, 2.1b,** and **Figure 2.2**). Across samples, remote specimens received less than 5 Gy exposure. Patient A previously underwent (unsuccessful) radiofrequency CA that did not control subsequent VT episodes, and this catheter-ablated myocardium was used for comparison (**Figure 2.1c** and **Figure 2.2)**.

At baseline, individual hearts exhibited distinct levels of underlying fibrosis. Given that anatomic scarring is an important consideration for prescribing treatment locations and volumes[17], greater fibrosis is expected in radiation-targeted regions even prior to treatment. Image-segmented analysis detected nonsignificant differences in fibrosis between matched targeted and nontargeted regions of patients' hearts, and fibrosis was lower in all radiation-targeted myocardium when compared to CA myocardium (**Figure 2.1d)**. Independent of fibrosis, all 4 patients experienced substantial reductions in VT episodes in the 6 months following RT (**Figure 2.1e)**.

Representative contrast-enhanced magnetic resonance imaging (MRI) scans of Patient E revealed no change in gadolinium enhancement and preserved myocardial tissue between baseline and at 3-month follow-up in the RT-targeted region (**Figure 2.1f)**, and there was no evidence of increased fibrosis on MRI post-RT in any patient. These clinical findings are consistent with previous preclinical studies that required doses in excess of 40 Gy to produce scar[47,49,68,78]. Collectively, these data strongly suggest that fibrosis alone cannot explain the clinical timeline and magnitude of reduced VT burden observed after RT.

Variable	**Patients A-J**
Median Age (year) [Range]	66 [49-84]
Sex (n)	
Female	2
Male	8
NYHA Class (n)	
I (1)	1
III (7)	7
IV (2)	2
Cardiomyopathy (n)	
ICM	4
NICM*	8
Median BMI [Range]	31.7 [23.8-48.6]
Comorbidities (n)	
CHF	9
COPD	1
CKD	2
CVA	2
DM	4
HD	1
MI	4

Median AADs [Range]	2 [1-2]
Median Prior CAs [Range]	2 [0-3]

Table 2.1. Summary of the clinical information of cardiac RT patients included in the present study. NYHA = New York Heart Association heart failure classification; ICM = ischemic cardiomyopathy; NICM = nonischemic cardiomyopathy; BMI = body mass index; CHF = congestive heart failure; COPD = chronic obstructive pulmonary disease; CKD = chronic kidney disease; CVA = cerebrovascular accident; HD = hepatic disease; DM = diabetes mellitus; MI = myocardial infarction; AAD = anti-arrhythmic drug; CA = catheter ablation

*Includes 2 patients with NICM prior to MI

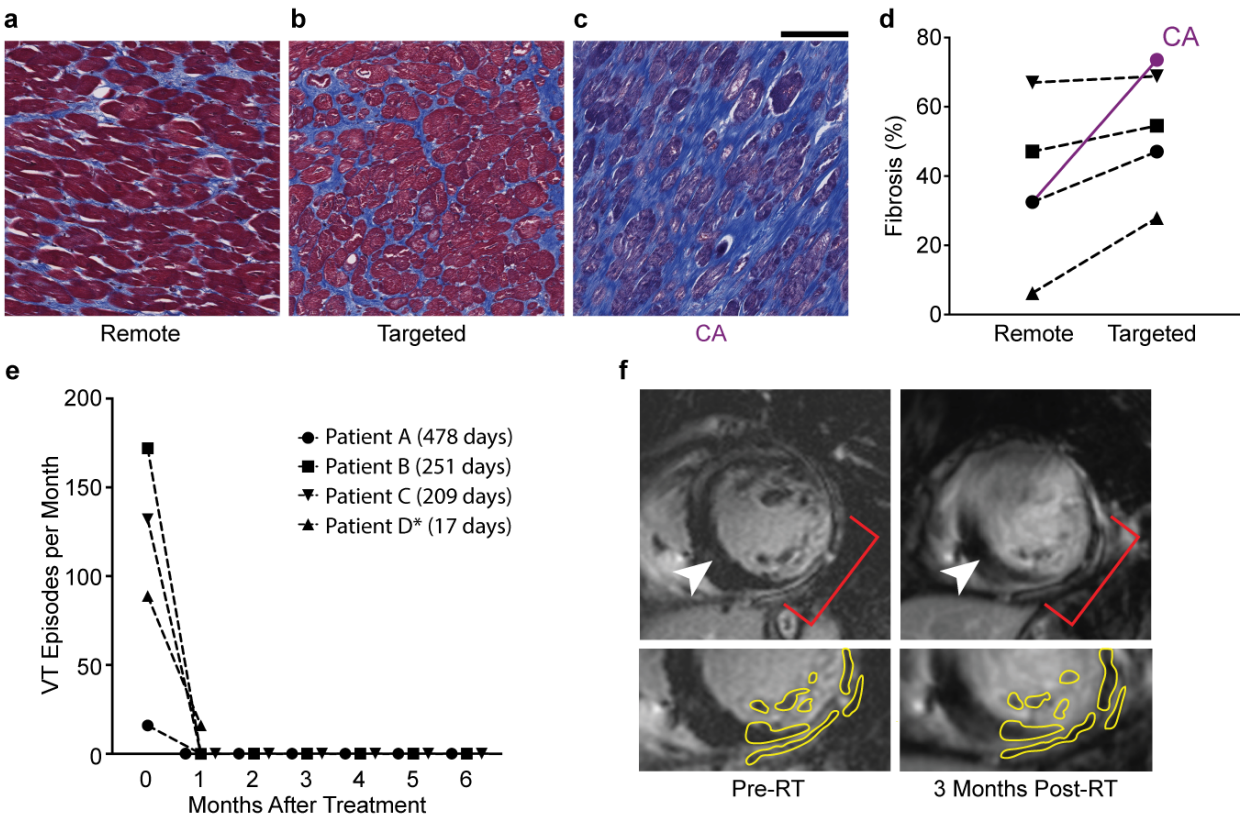

Figure 2.1. Cardiac fibrosis alone cannot account for the timing and effect of VT reduction after RT. (a-c) Representative Masson's trichrome stains of regions of remote (a), targeted (b), and failed CA (c) myocardium in the same patient who received 25 Gy ionizing radiation for treatment of refractory VT. Scale bars = 500 μm. Experiment was independently repeated once on the same patient samples and produced similar results. **(d)** Percent fibrosis at time of heart explant from 4 patients who received 25 Gy RT in control (left) and targeted (right) regions of myocardium. Percent fibrosis of the CA region for Patient A is shown in purple. **(e)** Defibrillator-recorded episodes of VT in the month before treatment and the 6 months after treatment for each patient. Days post-treatment until specimen collection are shown in the legend. *Patient D's values are divided by 20 to allow for comparisons on the same scale. **(f)** Gadolinium-enhanced MRI of a cardiac RT patient at baseline (left) and 3 months post-treatment (right). Top: The left ventricle

with patchy, gadolinium-enhanced scar was transmurally targeted with 25 Gy between 3- and 6-o'clock (red brackets). Nonenhanced, remote myocardium is adjacent to target region (white arrowhead). Bottom: Surviving nonenhanced myocardium within the same images are visible in the targeted region at baseline and 3 months post-treatment (yellow outline).

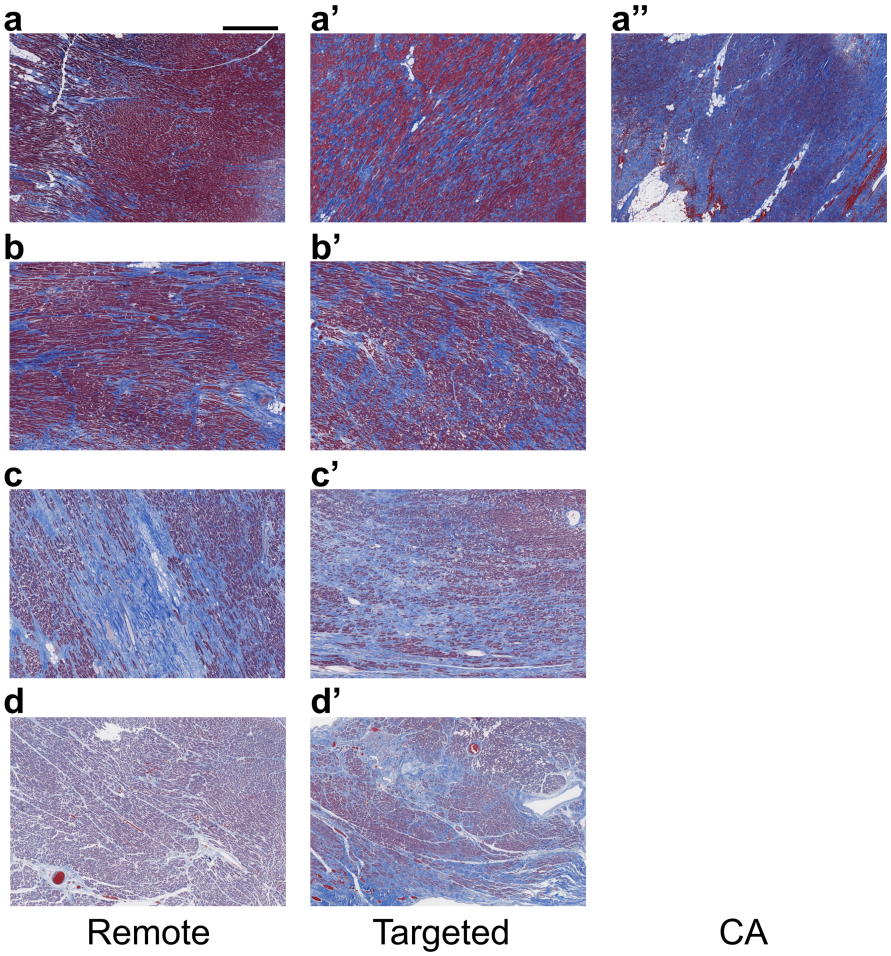

Figure 2.2. Cardiac RT does not create catheter ablation-like scar. Left column: Nontargeted regions of cardiac RT patient hearts. Middle column: targeted regions of hearts that received 25 Gy ionizing radiation in the same patients for treatment of VT. **(a, a', a'')** Representative trichrome images from remote, IR-targeted, and radiofrequency ablation regions of Patient A's explanted heart, respectively. Patient A received heart transplant 478 days after RT treatment and previously

underwent failed radiofrequency CA. **(b, b'**) Representative trichrome images from remote and IR-targeted regions of Patient B's postmortem heart, respectively. Patient B expired 251 days after RT, and heart failure progression is suspected as the cause of death. **(c, c')** Representative trichrome images of remote and IR-targeted regions of Patient C's postmortem heart. Patient C expired 209 days after RT, and the cause of death was chronic amiodarone-induced pulmonary fibrosis. **(d, d')** Representative images of targeted and nontargeted regions of Patient D's postmortem heart. Patient D expired 17 days after therapy due to an acute ischemic stroke. Scale bars = 1 mm.

Chapter 3: Radiotherapy-Induced Cardiac Electrical Reprogramming *in vivo*

3.1 Adult murine hearts rapidly recover from 25 Gy radiation

Most patients who received cardiac RT survive with reduced VT burden for years after treatment. Because of the durability of this emerging therapy, available post-mortem samples remain limited, further emphasizing the need for preclinical cardiac RT studies. Given the limitations in available postmortem samples, I utilized a translational adult murine model of whole-heart radiation to further evaluate effects of 25 Gy irradiation (IR) to the heart . To test whether post-mitotic adult mammalian cardiomyocytes recover from 25 Gy radiation-induced DNA damage, irradiated mice were sacrificed acutely at 30 mins, 3h, and 24h post-IR for histology. Frozen sections of irradiated hearts were stained for phosphorylated histone H2AX (γH2AX), a marker of double-stranded DNA breaks[128]. Acutely after 25 Gy treatment, histone H2AX is phosphorylated to demarcate regions of double-stranded DNA breaks in the genome. On immunofluorescence, both percentages of γH2AX-positive nuclei and mean γH2AX intensity decreased with respect to time, with the majority of damage-associated intensity resolving by 3 hours post-RT (**Figure 3.1**). The ability for the murine heart to rapidly resolve its post-RT γH2AX foci represents a property of radioresistant tissues and indicates rapid DNA repair and survival[129].

At 6 weeks post-IR, I performed Masson's trichrome staining to assess for gross evidence of fibrosis at a longer timepoint when substantial reductions in VT burden were observed clinically. Within these samples, there was no evidence of collagen staining in either treatment condition

after 6 weeks (**Figure 3.2a**). Furthermore, there was no observed difference in basement membrane deposition or collagen content between treated and untreated murine ventricles after 6 weeks post-IR, as determined by quantitative hydroxyproline assay (**Figure 3.2b**). Collectively, these data suggest that fibrosis may not play an immediate role in the radiation response or antiarrhythmic effect of the post-mitotic heart.

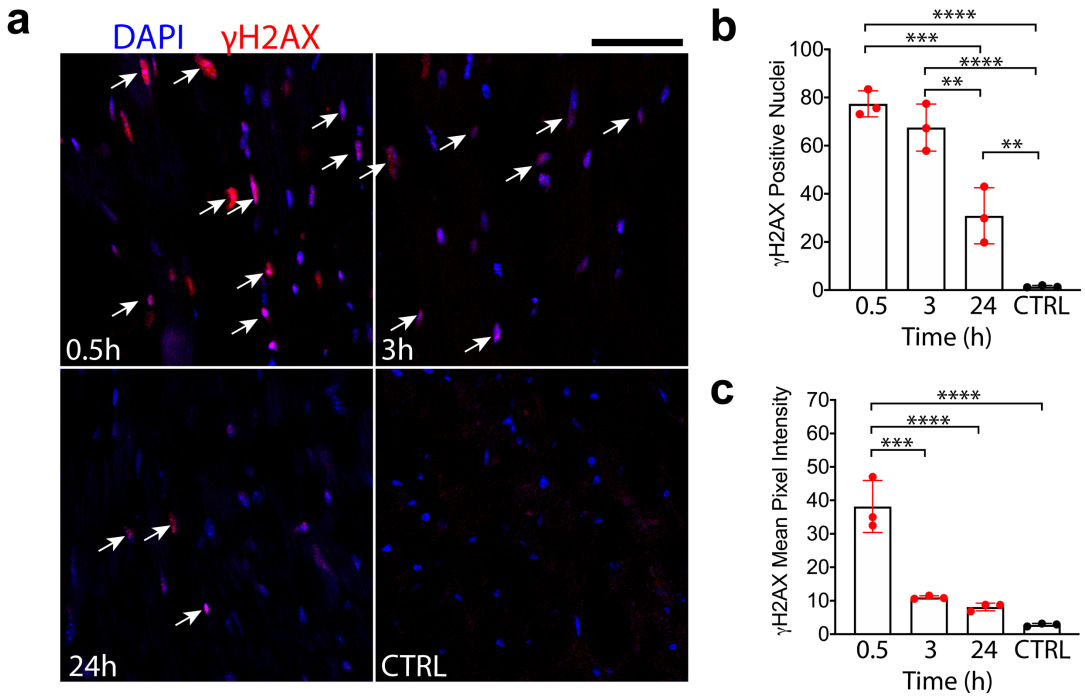

Figure 3.1. The adult mammalian heart rapidly recovers from radiation-induced DNA damage as detected by γH2AX. (a) Immunostaining of hearts for γH2AX (red) and DAPI (blue) after 25 Gy ionizing radiation at 0.5h, 3h, and 24h post-IR, or sham control. Dual-positive nuclei are highlighted with white arrows. **(b)** Quantification of percent γH2AX-positive nuclei in each irradiated (red) or control (black) condition. n = 3 biologically independent specimens per condition; $^{**}P$ = 0.0023 (3h vs 24h) and 0.0091 (24h vs CTRL); $^{***}P$ = 0.0005 (0.5h vs 24h); $^{****}P < 0.0001$ (0.5h vs CTRL and 3h vs CTRL). **(c)** Quantification of mean γH2AX-foci intensity in each irradiated (red) or control (black) condition. (n = 3 biologically independent

sample per condition); ***$P = 0.0001$ (0.5h vs 3h); ****$P < 0.0001$ (0.5h vs 24h and 0.5 vs CTRL). All images were taken with the same microscope settings. Scale bars = 50 µm. Statistical analysis consisted of a one-way ANOVA followed by one-sided Tukey post-hoc test of multiple comparisons. All bar graphs are represented as mean ± SD.

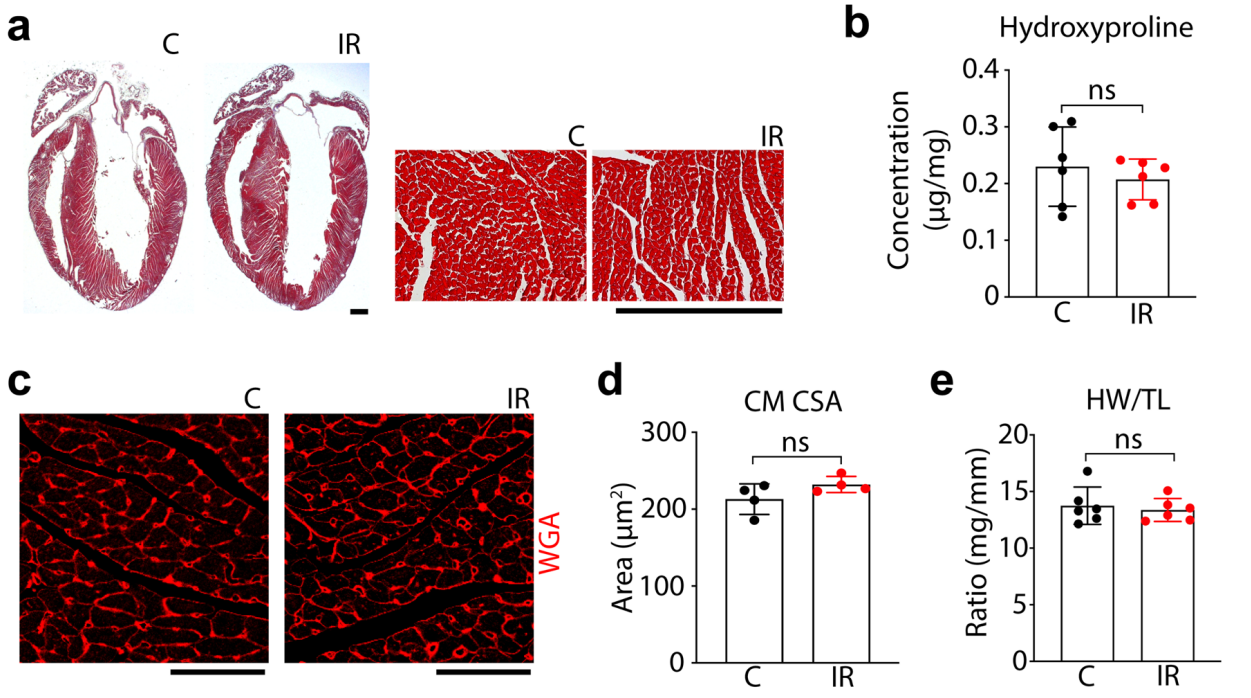

Figure 3.2. Radiation does not affect gross cardiac morphology at 6w post-IR. (a) Two magnifications of Masson's trichrome stains of control and IR mouse hearts at 6 weeks post-IR. Scale bars = 500 µm. Experiment was replicated three times in biologically independent mice and produced similar results. **(b)** Hydroxyproline content of control and IR hearts after 6 weeks ($n = 6$ biologically independent samples per condition; $P = 0.50$). **(c)** Representative WGA staining of control (left) and IR mouse (right) hearts at 6 weeks post-IR. Scale bars = 100 µm. Experiment was replicated four times in biologically independent mice and produced similar results. **(d)** Quantification of cardiomyocyte cross sectional area at 6 weeks post-IR reveals no difference (*n*

= 4 biologically independent specimens per condition; $P = 0.14$). **(e)** Heart weight to tibia length ratios at 6 weeks post-IR ($n = 6$ biologically independent samples per condition; $P = 0.63$). P values determined by two-way unpaired t-test. All bar graphs are represented as mean ± SD.

3.2 Twenty-five Gy radiation enhances cardiac conduction and reprograms electrophysiology

Electrophysiologic and structural remodeling both contribute to arrhythmogenic substrates in the setting of disease. Because RT reduces VT in the absence of profound CA-like structural change, I evaluated potential electrophysiologic mechanisms by which IR may prevent reentry. Specifically, I tested the effects of 25 Gy IR on adult murine cardiac electrophysiology at the clinically-efficacious timepoint of 6 weeks post-IR, when a 99.9% reduction in VT burden was reported in patients[17].

While previous preclinical studies reported heart block after IR in the 40-160 Gy dose range[44,67,78], 25 Gy radiation did not cause atrioventricular delay as measured by PR interval on ECG (**Figure 3.3a, 3.3b**). However, a significantly shortened QRS interval was observed in IR mice compared to sham controls (**Figure 3.3a, 3.3c**), while heart rate and other ECG intervals were unchanged (**Figure 3.4a-c**).

To measure functional effects associated with QRS shortening, I Langendorff-perfused and optically mapped irradiated mouse hearts. At 6 weeks post-IR, ventricular CVs were significantly increased in IR mice compared to sham controls (**Figure 3.3d, 3.3e,** and **Figure 3.4d**). Epicardial

pacing and restitution further demonstrated that APD at 80% repolarization (APD_{80}) and ERP were unchanged in these same hearts (**Figure 3.3f, 3.3g,** and **Figure 3.4e**). Together, these results suggest that 25 Gy radiation increases CV in the absence of profound changes to electrical repolarization, which may favorably alter conditions against electrical reentry.

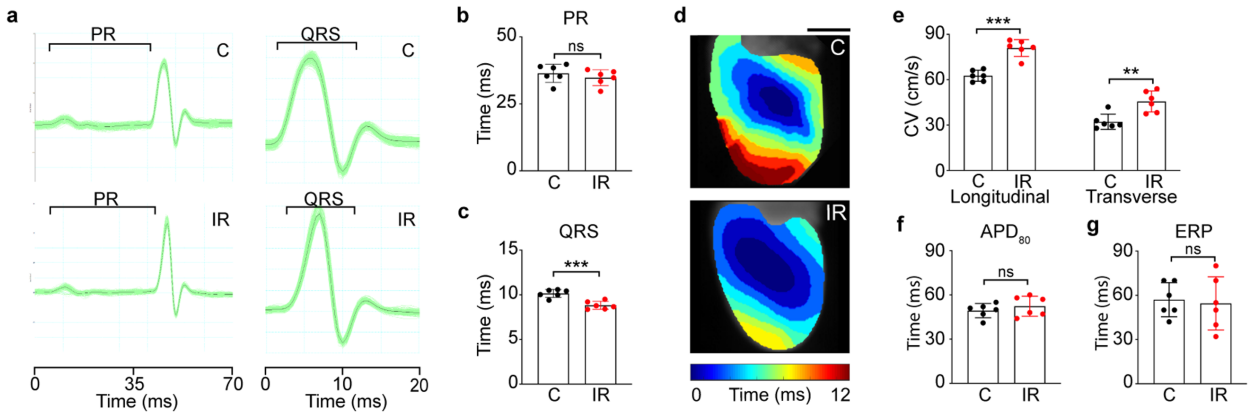

Figure 3.3. Cardiac IR enhances adult murine ventricular conduction. (a) Representative ECGs from control (top) and IR mice (bottom) highlighting PR and QRS intervals. **(b** and **c)** Effect of radiation on PR ($P = 0.39$) and QRS ($^{**}P = 0.00043$) intervals in control (black) versus IR (red) mice ($n = 6$ biologically independent animals per condition). (**d**) Representative ventricular activation maps from control and IR mice. Scale bars = 3 mm. (**e**) Effect of RT on ventricular CV($n = 6$ biologically independent animals per condition; $^{***}P = 0.00005$; $^{**}P = 0.0034$). (**f** and **g**) APD_{80} ($P = 0.39$) and ERP ($P = 0.78$) in control versus IR mice ($n = 6$ biologically independent animals per condition).

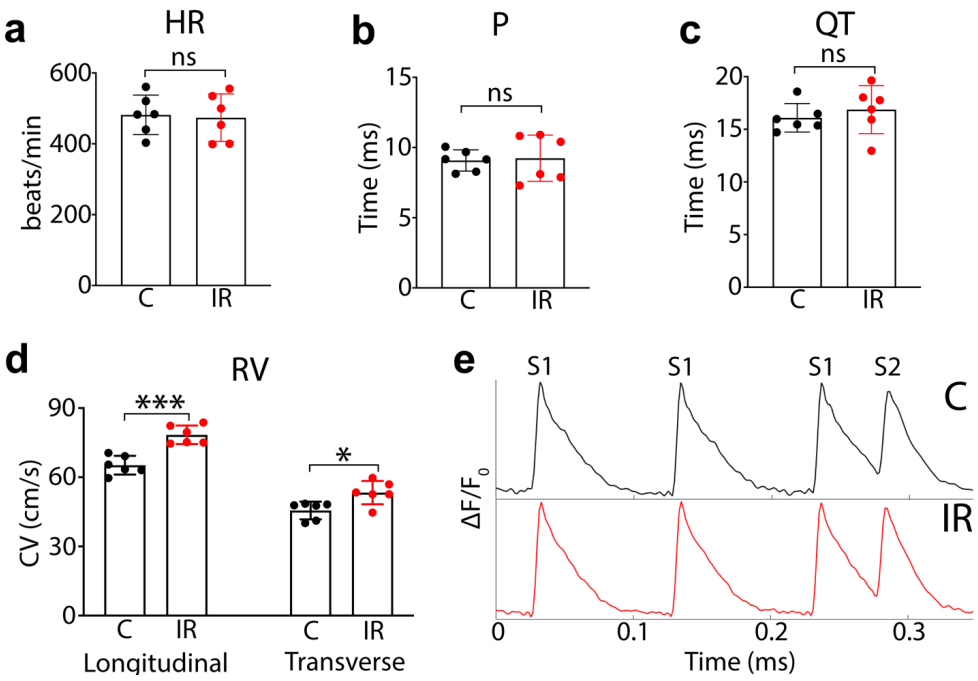

Figure 3.4. Cardiac IR increases conduction parameters in mice without affecting repolarization or other rhythm parameters. (a to **c)** Heart rate (HR, $P = 0.82$), P interval ($P = 0.83$), and QT interval ($P = 0.49$) of control versus IR mouse hearts at 6 weeks post-IR as measured by ECG reveal no differences ($n = 6$ biologically independent samples per condition). **(d)** Right-ventricular conduction velocities of control versus irradiated mouse hearts at 6 weeks post-IR ($n = 6$ biologically independent samples per condition; ***$P = 0.00022$; *$P = 0.014$,) demonstrate similar conduction increases as seen in the left ventricle. (**e**) Representative optical action potentials from control (top) and IR (right) during S1-S2 ventricular stimulation. Representative S1-S2 cycle lengths for each mouse was within 5 ms of recorded ventricular effective refractory periods. *P* values determined by two-way unpaired *t*-test. All bar graphs are represented as mean ± SD.

3.3 Ionizing radiation increases expression of cardiac conduction proteins

To understand how ionizing radiation may mechanistically increase cardiac conduction, I sequentially assessed for the effects of radiation on four known major molecular determinants of cardiac conduction: (1) fibrosis, which influences intercellular coupling and conduction propagation; (2) cardiomyocyte cell size, which affects intracellular resistance; (3) the cardiac sodium channel, responsible for phase 0 depolarization of cardiomyocytes; and (4) cardiac gap junctions, which allow for passive diffusion of charge. As described above, 25 Gy IR did not influence fibrosis or collagen deposition in murine hearts at 6w post-IR (**Figure 3.2a, 3.2b**). Using wheat germ agglutinin (WGA) staining to label cardiomyocyte cell borders, I detected no differences in cardiomyocyte cross sectional area between treatment groups (**Figure 3.2c, 3.2d**), and furthermore, the heart weight to tibia length ratio, a surrogate marker of hypertrophy, was unchanged **(Figure 3.2e)**.

To determine whether ion channel determinants of CV are differentially expressed after cardiac IR, I performed quantitative gel electrophoresis and immunoblotting on IR tissue lysates. Densitometric quantification showed an approximately 80% increase in $Na_V1.5$, the pore-forming alpha subunit of the cardiac sodium channel, within IR ventricles compared to controls (**Figure 3.5a**). Immunoblotting for connexin 43 (Cx43), the major subunit of the ventricular gap junction, revealed an approximately 2-fold relative increase in levels of Cx43 in the same hearts (**Figure 3.5b)**. Immunohistochemistry demonstrates that these proteins maintain normal physiologic

distributions within cardiomyocytes with no change in channel localization between groups (**Figure 3.5c, 3.5d**).

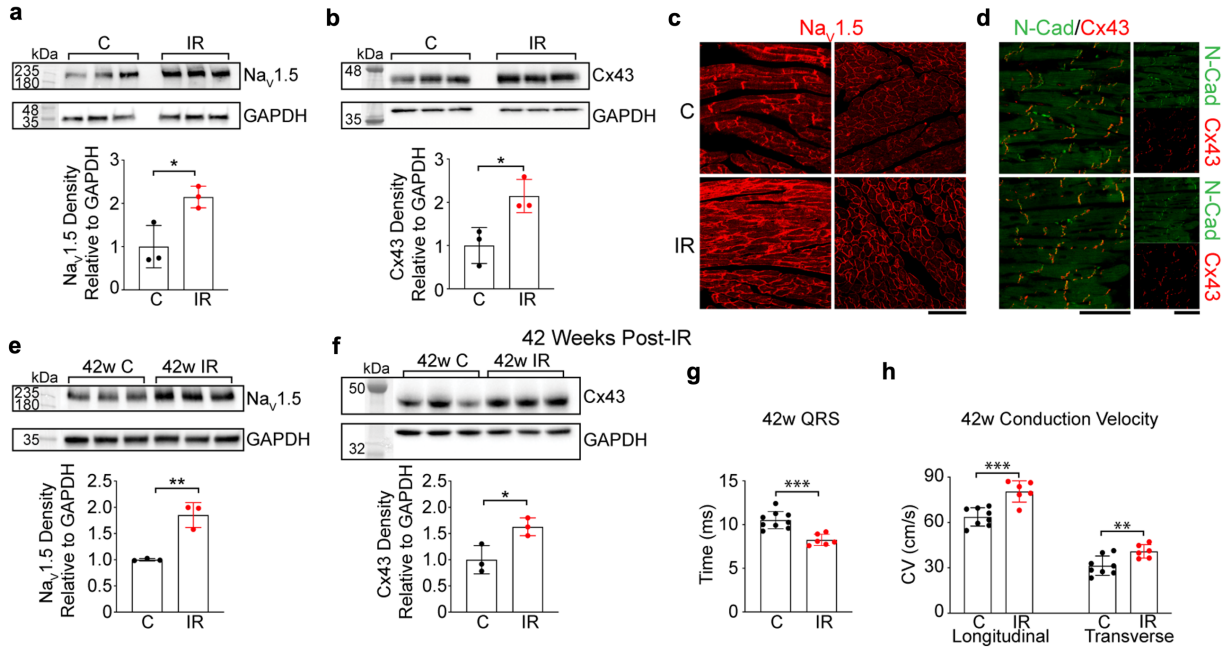

Figure 3.5. Radiation persistently upregulates cardiac conduction proteins to reprogram ventricular conduction. (**a** and **b**) Western blots of Na$_V$1.5 (**P* = 0.022) and Cx43 (**P* = 0.025) in control and IR ventricles (*n* = 3 biologically independent samples per condition). (**c**) Immunostaining of control (top) and IR (bottom) myocardium for Na$_V$1.5 and **(d)** co-stained for Cx43 (red) and N-Cadherin (green). Scale bars = 70 μm. (**e** and **f**) Western blots of Na$_V$1.5 (***P* = 0.0034) and Cx43 (**P* = 0.027) after 42 weeks post-IR (*n* = 3 biologically independent samples per condition). (**g**) Effect of RT on QRS intervals in control versus IR mice after 42 weeks (****P* = 0.00027; C, *n* = 9; IR, *n* = 6). (**o**) Left ventricular CVs in control (*n* = 9 biologically independent animals) versus IR (*n* = 6 biologically independent animals) mice at 42 weeks post-IR (****P* = 0.00042; ***P* = 0.0092,). All *P* values determined by two-way unpaired *t*-test. Bar graphs are represented as mean ± SD.

3.4 Single fraction radiation durably reprograms the cardiac electrical substrate

Patients receiving cardiac RT experience persistent reductions in VT burden[18,19,27]; therefore, I hypothesized that radiation-induced effects on cardiac conduction may persist over time. To better understand the chronic implications of single-fraction radiation for VT therapy, I asked whether CV, $Na_V1.5$ levels, and Cx43 levels remain persistently elevated. In an aged cohort of mice at 42 weeks post-IR, IR hearts continued to express increased $Na_V1.5$ and Cx43 (**Figure 3.5e, 3.5f)**, and the QRS also remained shortened (**Figure 3.5g** and **Figure 3.6a-d)**. These persistent molecular effects translated into persistently upregulated CVs (**Figure 3.5h** and **Figure 3.6e**). These findings importantly highlight a potential role for radiation-induced electrical reprogramming of the cardiac conduction substrate. Taken together, one single-fraction 25 Gy dose of IR is sufficient to achieve persistent electrical reprogramming of the heart, consistent with reports of patients with reduced VT burden 2 years after their RT treatment[18,27].

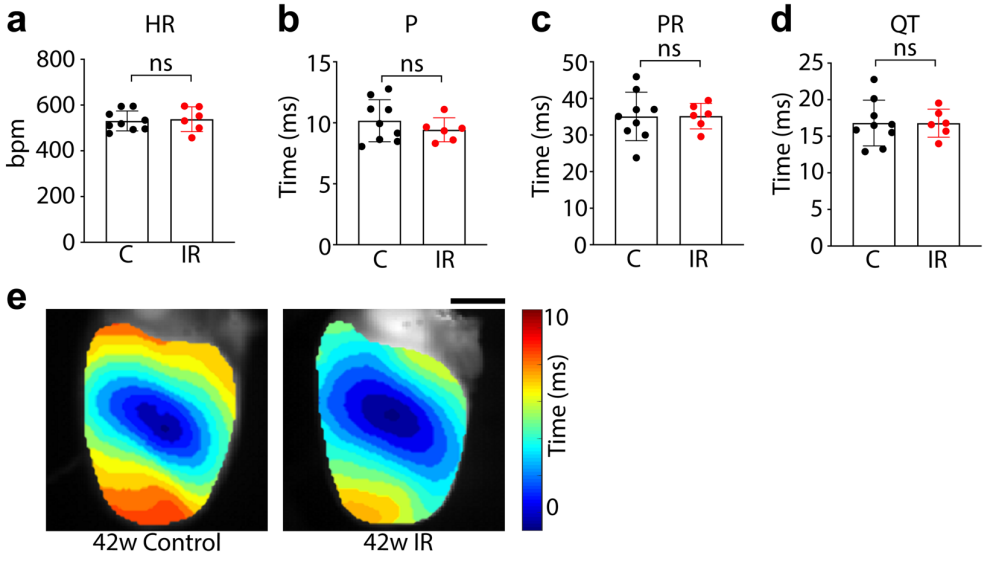

Figure 3.6. Cardiac IR persistently increases conduction and shortens the QRS interval without affecting other ECG parameters. (**a** to **d**) Heart rate (HR, $P = 0.77$), P interval ($P =$

0.36), PR interval ($P = 0.97$), and QT interval ($P = 0.99$) of control ($n = 9$ biologically independent animals) versus irradiated ($n = 6$ biologically independent animals) mouse hearts at 6 weeks post-IR as measured by ECG. (**e**) Representative ventricular activation maps from control (left) and IR (right) mice 42 weeks post-IR. Scale bars = 3 mm. *P* values determined by two-way unpaired *t*-test. All bar graphs are represented as mean ± SD.

3.5 Dose-dependent effects of radiation on conduction reprogramming

Clinically, doses of cardiac RT that demonstrate robust therapeutic efficacy in refractory VT patients are in the range of 24-25 Gy. This dose range was selected based on data from preclinical studies that attempted to create radiation-induced fibrosis[78]. Given that the mechanism of RT could be mediated through electrophysiologic reprogramming, I asked whether doses lower than 25 Gy would also be sufficient to achieve radiation-induced electrical changes to improve cardiac RT safety while maintaining efficacy. Using a dose de-escalation approach in 5 Gy increments, I observed significantly faster CVs and shorter QRS durations in IR hearts treated with 20 Gy and 15 Gy, while doses of 10 Gy or 5 Gy did not result in significant differences (**Figure 3.7a, 3.7b)**. As expected, ECG intervals were comparable among treatment groups prior to IR treatment (**Figure 3.8**), and I did not observe dose-dependent differences in other ECG intervals or murine heart rate at 6 weeks post-IR (**Figure 3.9**). Overall, the magnitude of conduction increase measured by CV and QRS tended to be greater in the 20 Gy group than in the 15 Gy group, though this study was not designed to detect differences between these two groups. Consistent with the functional dose response, Western blotting of protein lysates revealed dose-dependent upregulation of both

$Na_V1.5$ and Cx43 protein (**Figure 3.7c, 3.7d**). Although the largest biological effects were seen at 25 Gy, these findings suggest that lower doses of ionizing radiation, between 15 Gy and 20 Gy, may also be sufficient to achieve therapeutic electrophysiologic effects of RT on VT reduction.

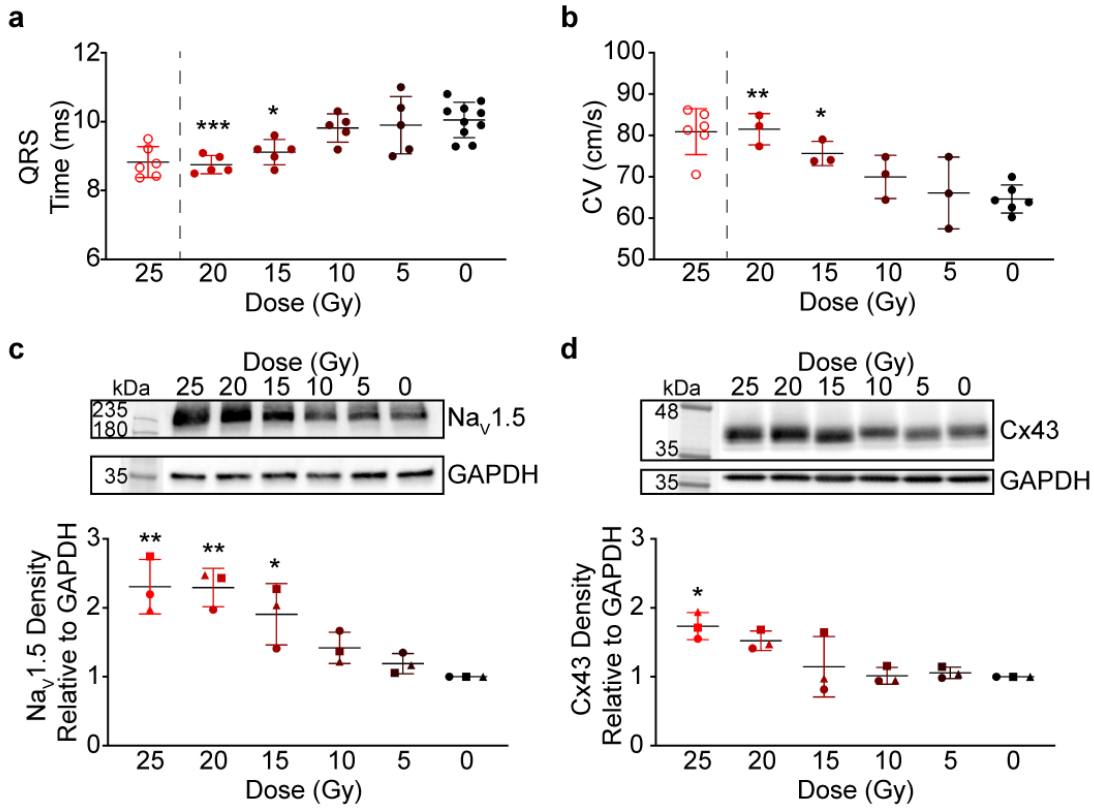

Figure 3.7. Conduction velocity reprogramming may be achieved at lower doses of radiation. (**a**) Dose-dependent effects of radiation on QRS interval at 6 weeks post-IR (n = 5 biologically independent animals per IR condition; n = 10 biologically independent 0 Gy control animals; ***P = 0.0009, twenty Gy versus 0 Gy; *P = 0.023, 15 versus 0 Gy). (**b**) Dose-dependent effects of radiation on longitudinal conduction velocity (n = 3 biologically independent animals per IR condition; n = 6 biologically independent 0 Gy control animals; **P = 0.0023, 20 versus 0 Gy; *P = 0.046, 15 versus 0 Gy). (**c**) Dose-dependent effects of radiation on $Na_V1.5$ protein levels by Western blot (n = 3 biologically independent sample per condition over 3 independent

experiments; **P = 0.0014, 25 versus 0 Gy; **P = 0.0016, 20 versus 0 Gy; *P = 0.023, 15 versus 0 Gy;). (**d**) Dose-dependent effects of radiation on $Na_V1.5$ protein levels by Western blot (n = 3 biologically independent per condition over 3 independent experiments; *P = 0.011, 15 versus 0 Gy). Values plotted from Westerns were obtained from three independent Western blots each denoted by a closed square, circle, and triangle. Twenty-five Gy QRS interval and CV values from Figure 3 are plotted for reference (open circles) and are not used in statistical comparisons. Statistical analysis of all subpanels consisted of a one-way ANOVA followed by one-sided Tukey post-hoc test of multiple comparisons. All bar graphs are represented as mean ± SD.

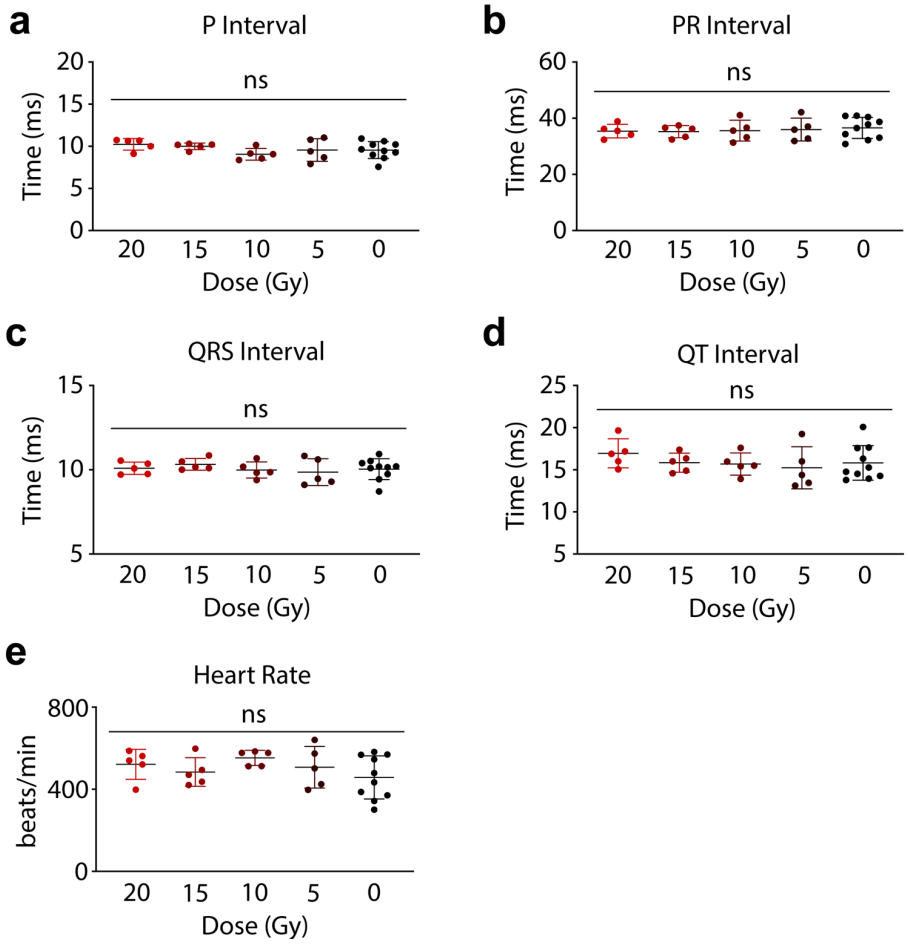

Figure 3.8. Baseline murine ECGs are comparable across treatment conditions. Baseline ECG intervals prior to dose-dependent treatment. **(a)** P interval (P = 0.31), **(b)** PR interval (P =

0.95), **(c)** QRS interval ($P = 0.69$), **(d)** QT interval ($P = 0.85$), and **(e)** heart rate (HR, $P = 0.34$) at 6 weeks post IR ($n = 5$ biologically independent animals per IR condition; $n = 10$ biologically independent 0 Gy control animals). Nonsignificant statistics determined by ordinary one-way ANOVA. All bar graphs are represented as mean ± SD.

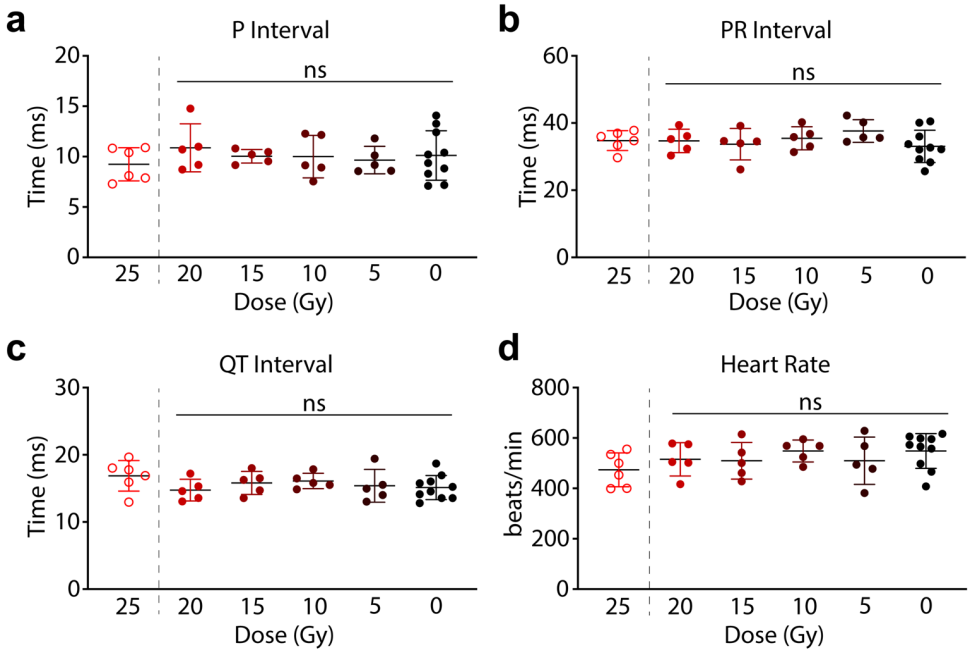

Figure 3.9. Dose-dependent effects of radiation on murine ECG intervals. (**a-d**) Dose-dependent effects of radiation on **(a)** P interval ($P = 0.91$), **(b)** PR interval ($P = 0.38$), **(c)** QT interval ($P = 0.75$), and **(d)** heart rate (HR, $P = 0.72$) at 6 weeks post IR ($n = 5$ biologically independent animals per IR condition; $n = 10$ biologically independent 0 Gy control animals). Values from an earlier twenty-five Gy cohort are plotted for reference (left, open circles, from Figure 3.4.) and were not used in statistical comparisons. Nonsignificant statistics determined by ordinary one-way ANOVA. All bar graphs are represented as mean ± SD.

3.6 Radiation uniquely increases conduction within surviving myocardium in the setting of injury

To further translate my findings in health adult murine hearts to individuals with cardiovascular disease, I next tested effects of radiation on cardiac conduction in the setting of injury and fibrosis, which better represents the myocardial substrate of the cardiac RT patient population. To this end, I utilized a surgical model of myocardial infarction (MI), in which the proximal left anterior descending (LAD) artery is permanently ligated, causing acute infarction of the apical left ventricle and subsequent replacement of apical myocardium by myofibroblasts and scar over a 2-week period[130]. At 2 weeks post-MI, mice were randomly subjected to either 25 Gy radiation or sham treatments, followed by downstream optical mapping experiments at 6 weeks post-IR.

Consistent with electrically-inert myofibroblasts within scar[131], direct stimulation of the scar region did not result in electrical capture or propagation of impulse in any heart (**Figure 3.10a**, grey region). Border zone (BZ) myocardium above the LAD ligation was subsequently stimulated, and CV through viable myocardium was quantified, including the anatomic BZ region, defined in this study as the 2mm segment of tissue scar junction. However, these impulses did not further propagate into the scar region (**Figure 3.10a**, grey region, and **Figure 3.11a**). In conducting myocardium, 25 Gy radiation significantly increased both longitudinal and transverse CVs (**Figure 3.10a, 3.10b**), which included isochrones in the anatomic BZ near the scar (**Figure 3.10a,** inset). Based on these observations, I postulated that increases to levels of $Na_V1.5$ and Cx43 occur primarily in surviving cardiomyocytes after injury and not scar myofibroblasts. To further delineate whether specific zones differentially upregulate $Na_V1.5$ and Cx43 after IR, ventricles

from MI and MI+IR mice were dissected into distinct regions of mid-basal BZ myocardium and apical scar. As expected, the presence of ion channel proteins was much higher in the conducting BZ myocardium than in the electrically-inert scar region at baseline (**Figure 3.11b, 3.11c**). Western blotting of protein lysates from the conducting BZ myocardium revealed increased expression of $Na_V1.5$ and Cx43 in MI+IR hearts compared to MI controls (**Figure 3.10c, 3.10d**), while these effects were not observed in regions of electrically inert scar tissue in the same hearts (**Figure 3.10e, 3.10f**). Together, these results in a surgical model of MI and cardiac injury reveal that high dose radiation uniquely reprograms surviving cardiomyocytes after injury.

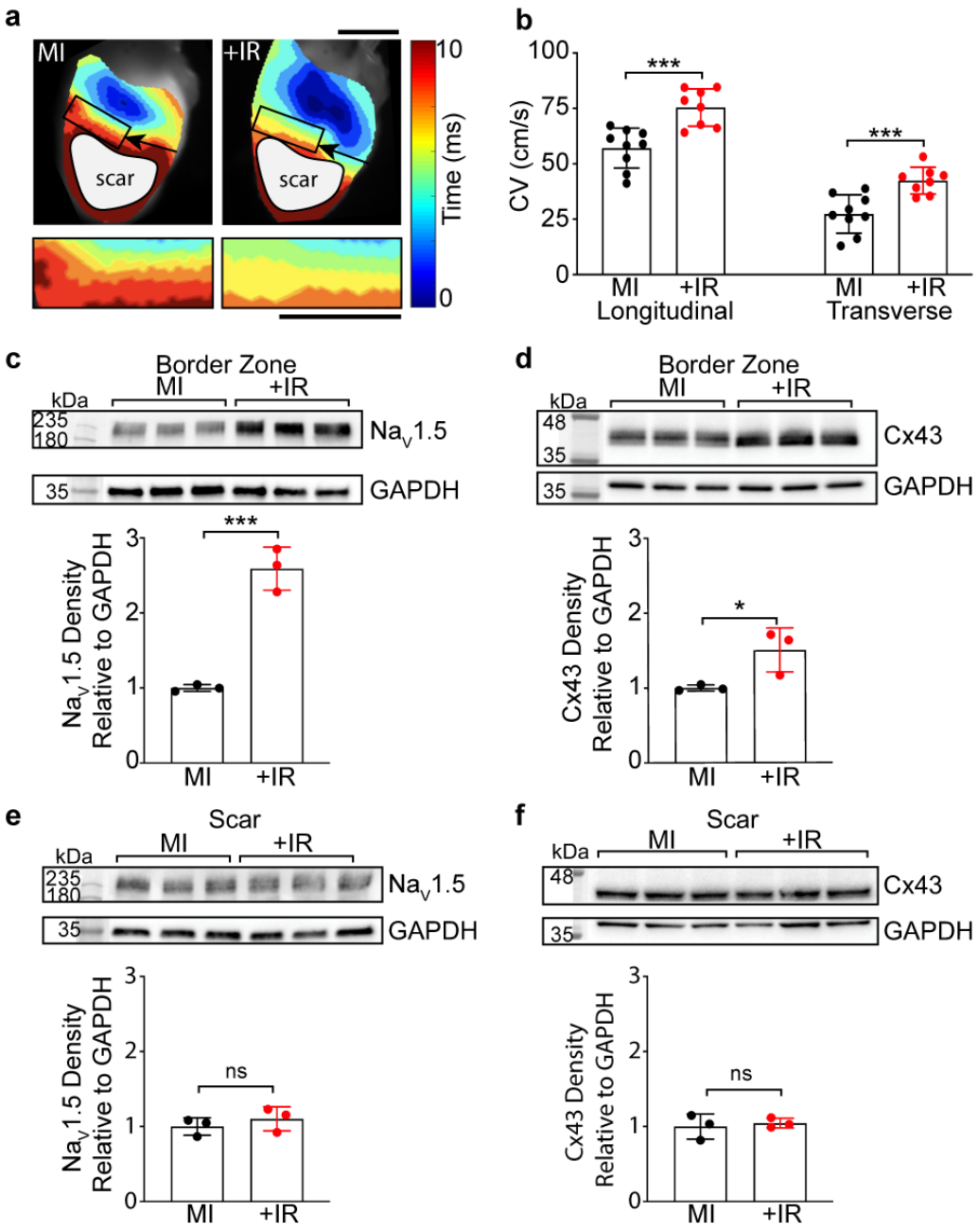

Figure 3.10. Radiation specifically reprograms the border zone myocardium in a murine model of myocardial infarction. (a) Top: Representative ventricular activation maps from control myocardial infarction (MI, left) and irradiated MI (MI+IR, right) mice at 8 weeks post-MI, 6 weeks post-IR. Black arrows point to location of left anterior descending (LAD) artery ligation. Black box denotes approximate 2 mm border zone at the scar/myocardium interface. Regions of scar

that were epicardially-stimulated but did not capture are denoted by grey circles. Magnified isochrones in the border zone region used to calculate transverse conduction velocities. Scale bars = 5 mm. **(b)** Left ventricular conduction velocities in MI (black) versus MI+IR (red) hearts (MI *n* = 9 biologically independent animals; MI+IR *n* = 8 biologically independent animals; longitudinal ***P = 0.0006; transverse ***P = 0.0009;). **(c** and **d)** Western blot (top) and quantified density (bottom) of $Na_V1.5$ (***P = 0.0007) and Cx43 (*P = 0.041) protein in MI and MI+IR border zone myocardium superior to the LAD ligation (n = 3 biologically independent samples per condition). **(e** and **f)** Western blot (top) and quantified density (bottom) of $Na_V1.5$ (P = 0.42) and Cx43 (P = 0.68) protein in MI control and MI+IR apical scars (n = 3 biologically independent samples per condition). All P values determined by two-way unpaired *t*-test. All bar graphs are represented as mean ± SD.

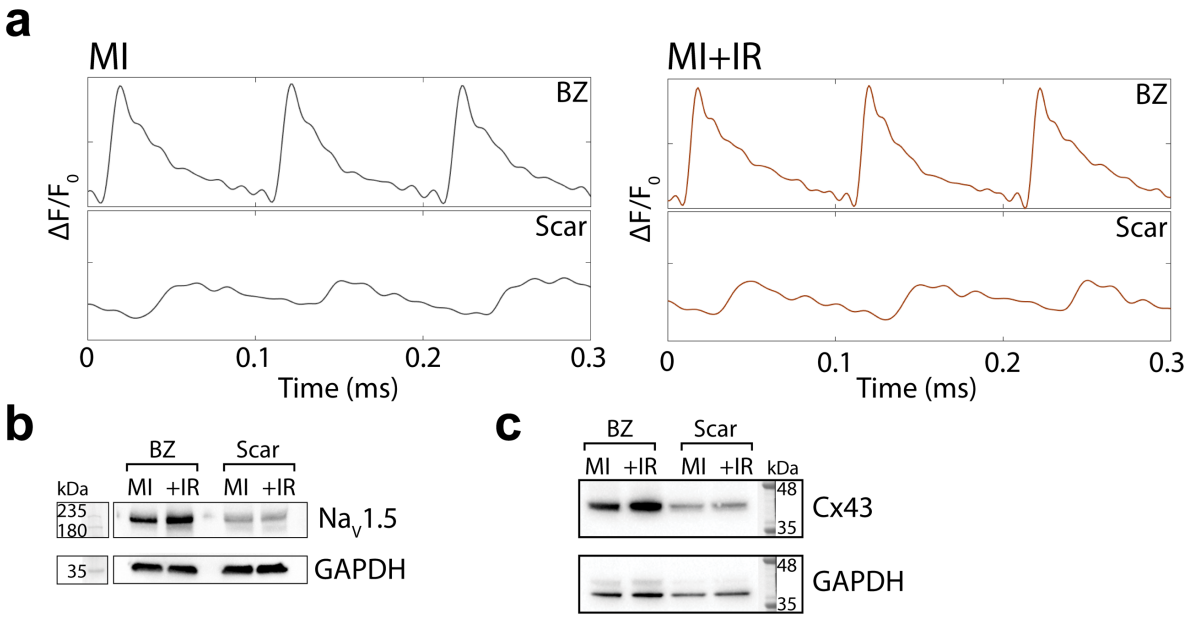

Figure 3.11. Cardiac IR in a murine model of large myocardial infarction. (**a**) Representative OAPs from MI (left) and MI+IR (right) hearts in BZ myocardium (top) and scar regions (bottom) during S1 ventricular stimulation. Optical signal from BZ exhibit OAPs with large-magnitude, fast depolarization and slow repolarization, while scar regions exhibit small electrostatic deflections, and low peak optical voltage (<50% BZ peak optical voltage), due to isodepolarization of nearby BZ myocardium. (**b** and **c)** Representative Western blots comparing $Na_V1.5$ and Cx43 protein in border zone versus scar zone myocardium in MI and MI+IR murine hearts demonstrating less conduction proteins in scar compared to BZ. Western blot experiments were replicated three times in biologically independent samples and produced similar results.

Chapter 4: Radiation-Induced Notch Reactivation Reprograms Cardiomyocyte Conduction

4.1 Differential gene expression and Notch signaling define the irradiated heart

While several DNA damage pathways have been previously implicated in the acute radiation response of a variety of tissue types[132], signaling pathways specific to the radiation response in the adult mammalian heart are not defined. To identify genes and pathways differentially expressed in the heart after IR, I profiled the ventricular transcriptome by bulk RNA sequencing (RNA-seq) in sham control mice and at 2- and 6-weeks post-IR. Overall, 509 genes were differentially expressed across sample groups (log fold change >1 and Benjamini-Hochberg adjusted significance of $P < 0.05$), and the greatest number of expression changes were observed comparing control and 6-week time points (**Figure 4.1a, 4.1b**). Generally, there was an observed bias towards increases in transcription at 6 weeks post-IR among differentially-expressed genes. In Gene Set Enrichment Analysis (GSEA) using MSigDB hallmark gene sets, proinflammatory and canonical stress response pathways were elevated at both timepoints **(Figure 4.2a)**. Within these response pathways, I observed that several of the most differentially-expressed genes were implicated in tissue stress responses to radiation **(Table 4.1)**, and many genes have either known pro- or anti-fibrotic functions in the heart **(Figure 4.1c, 4.1d)**. The presence of competing pro- and anti-fibrotic pathways after RT may help explain the lack of gross evidence of fibrosis at the clinically-efficacious timepoint of 6 weeks post-treatment.

Within the top 20 most overrepresented signaling response pathways, I also explored pathways previously implicated in the modulation of cardiac conduction. The Notch signaling pathway, which plays an important role in conduction system development[119,120,133], was present at both timepoints **(Figure 4.2a)**. Furthermore, leading edge analysis revealed Notch pathway-associated genes (*Cdkn1a*, *Jag1*, *Jag2*, and *Notch2*) driving enrichment of multiple pathways in GSEA. Given that Notch signaling becomes quiescent in resting adult cardiomyocytes, I investigated in detail the differential expression of all genes associated with the murine Notch signaling pathway gene ontology (GO) term. Unsupervised hierarchical clustering of Notch GO genes grouped samples into their respective timepoints, and each pairwise comparison showed significant changes in Notch genes, with a trend towards Notch activation at later timepoints **(Figure 4.2b)**. Specifically, the ligands *Jag1* and *Jag2* appeared be most prominently expressed at 6 weeks post-IR. Given this broad signal, I also investigated gene expression within Notch pathway functional classes, using genes with known relevance to cardiomyocytes, which further suggested cardiac Notch activation **(Figure 4.2c)** and pointed to the potential role for IR-induced Notch reactivation in the heart.

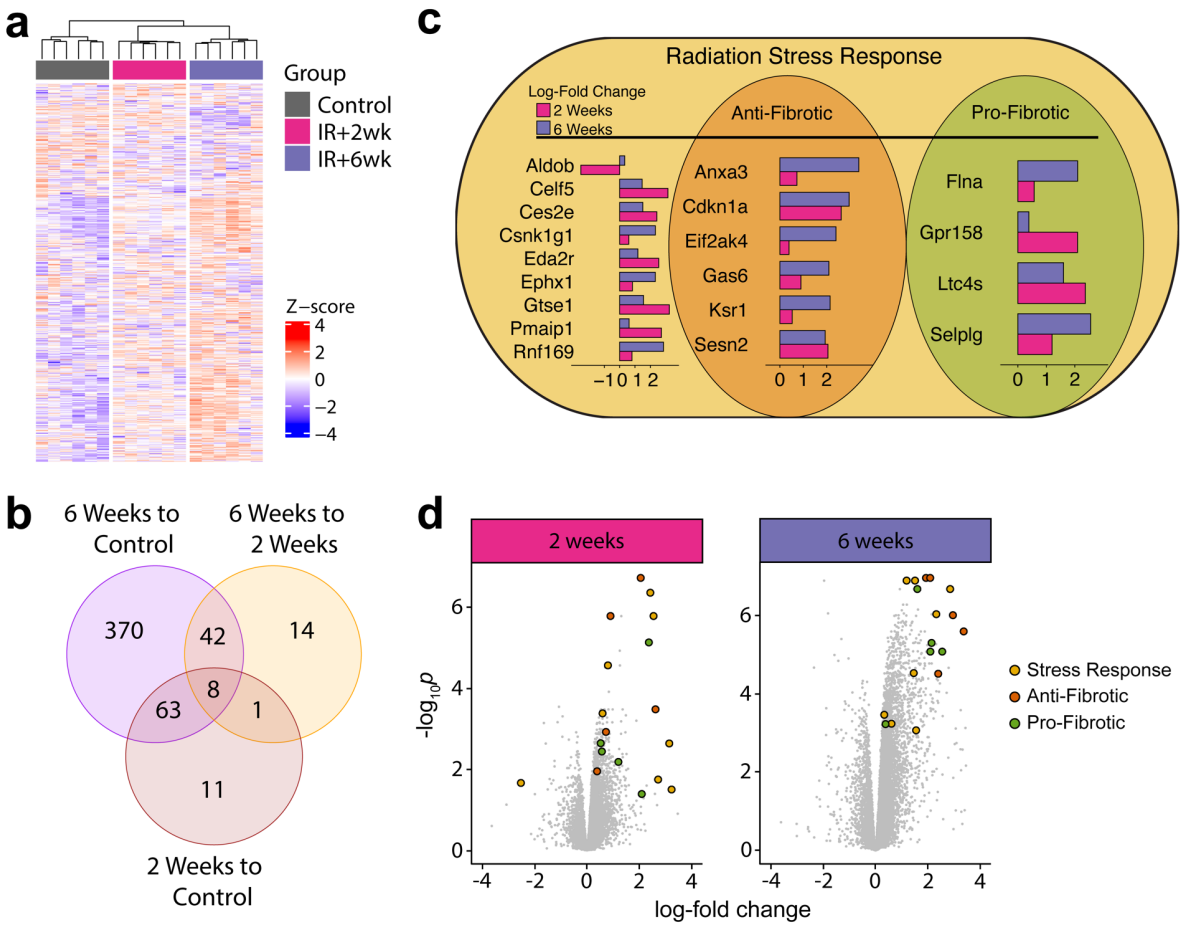

Figure 4.1. Post-IR states are differentiated by gene expression changes. (a) Heat map of all 509 differentially expressed genes at 2 weeks and 6 weeks post-IR. Samples are grouped by hierarchical clustering of gene states. (**b)** Venn-diagram of differentially-expressed genes at 2 weeks and 6 weeks post-IR across all comparisons. Gene expression changes present at 2 weeks tended to remain present at 6 weeks, and greatest number of expression changes were observed comparing control and 6-week time points. **(c)** Log-fold expression changes in radiation stress response genes. Genes are grouped by their potential pro- and anti-fibrotic activity based on prior publications (Supplementary Table 2). **(d)** Volcano plots showing fold-change and significance for all genes. Stress response genes from panel (c) are highlighted. Figure generated by Jeff Szymanski.

Gene	Role in Radiation Stress	Citation DOI	Role in Fibrosis	Citation DOI
Aldob	Suppresses G6PD activity in complex with p53	10.1038/s43018-020-0086-7	NA	NA
Anxa3	Activates JNK	10.1016/j.stemcr.2015.05.013	Inhibits PI3K/Akt	10.1002/jcp.27717
Ccl8	NA	NA	NA	NA
Cdkn1a	Anti-proliferative p53 target	10.1158/0008-5472. CAN-04-3995	Blocks angiotensin II	10.1016/j.peptides.2016.07.003
Celf5	p53 target		NA	NA
Ces2e	p53 target	10.1016/j.ebiom.2017.05.017	NA	NA
Csnk1g1	Inhibits p53 phosphorylation	10.1186/1476-4598-13-231	NA	NA
Eda2r	p53 target, binds extodysplasin EDA-A2	10.1126/science.290.5491.523	NA	NA
Eif2ak4	Induces p21 expression	10.1371/journal.pgen.1005212	Reduces collagen deposition	10.1161/JAHA.116.004453
Ephx1	NA	NA	NA	NA
Flna	BRCA scaffold	10.1530/ERC-13-0364 jk	ECM production	10.1536/ihj.17-446
Gas6	AXL ligand	doi:10.1172/JCI85610	Anti-apoptotic	10.1016/j.exger.2019.01.029
Gpr158	PI3K-AKT activation after DNA damage	10.1038/nrd3320	Increases collagen deposition	10.1161/CIRCGENETICS.114.000537

Table 4.1. Differentially-expressed stress and fibrosis response genes after IR. Top genes by adjusted P-value (limited to log-fold change >2) for comparisons of 2 weeks post-IR versus control and 6 weeks post-IR versus control and their roles in radiation stress and fibrosis.

NA = not available; DOI = digital object identifier

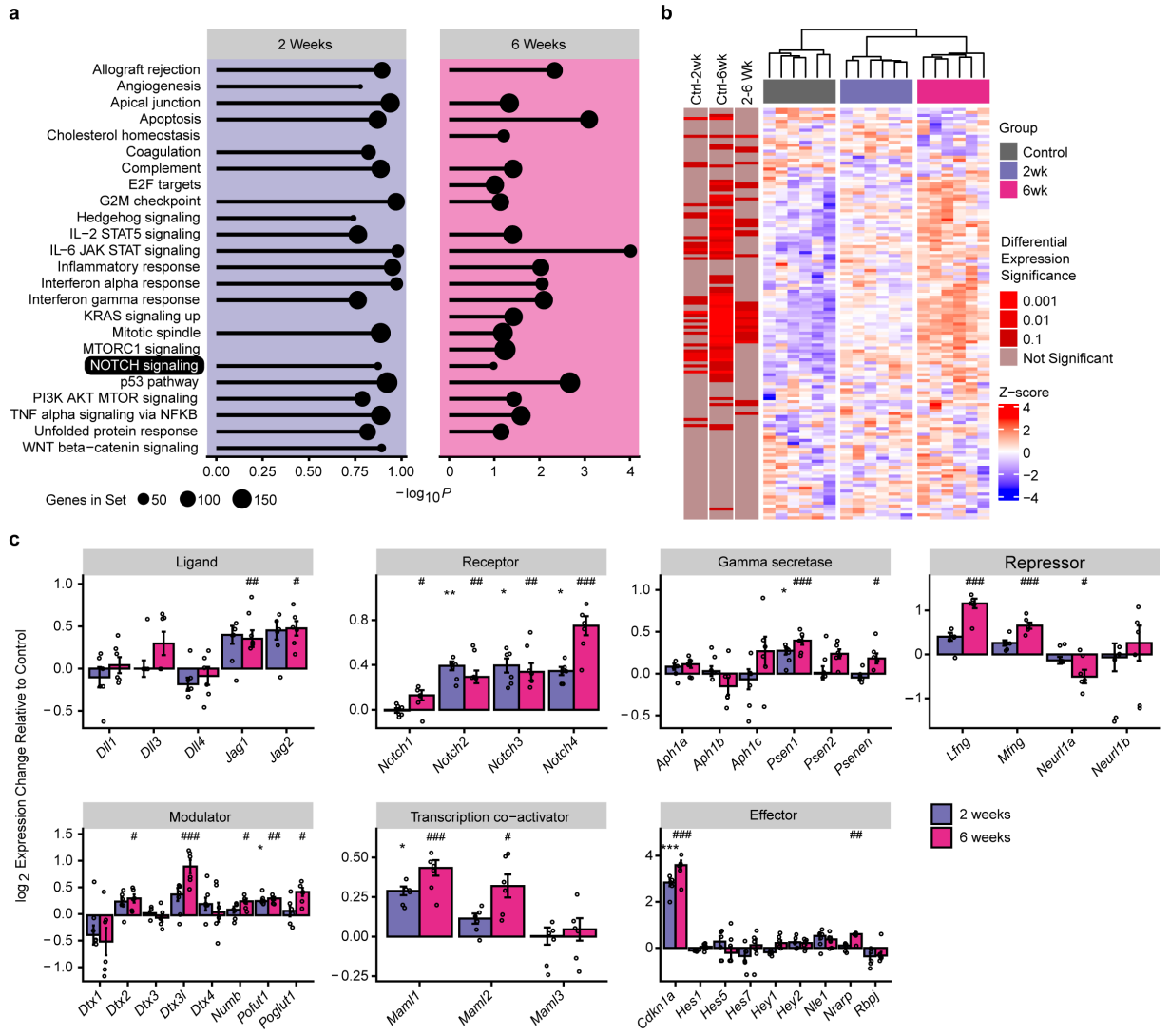

Figure 4.2. Post-IR states exhibit distinct transcriptional signatures and activation of the Notch signaling pathway. (a) Top 20 transcriptionally over-represented hallmark pathways at 2- and 6-weeks post-IR. The Notch signaling pathway is present at both timepoints, and Notch pathway-associated genes *Cdkn1a, Jag1*, *Jag2*, and *Notch2* were drivers of enrichment in other over-represented pathways. **(b)** Heatmap of Notch GO term genes. Samples group by hierarchical clustering of Notch GO gene expression. **(c)** Cardiac-related Notch pathway members grouped by function. Bar graphs represent $\log_2$-fold change at 2 weeks or 6 weeks post-IR relative to sham control state and error bars represent standard error (n = 6 biologically independent samples per

treatment group, *indicates comparisons of 2 weeks post-IR versus control, #indicates comparisons of 6 weeks post-IR versus control, */#$P < 0.10$, **/##$P < 0.01$, ***/###$P < 0.001$). *Jag1* ##$P = 0.0049$; *Jag2* #$P = 0.03$; *Notch1* #$P = 0.076$; *Notch2* **$P = 0.0066$, ##$P = 0.0012$; *Notch3* *$P = 0.014$, ##$P = 0.0019$; *Notch4* *$P = 0.015$, ###$P = 7.2E-6$; *Psen1* *$P = 0.051$, ###$P = 0.00078$; *Psenen* #$P = 0.024$; *Lfng* ###$P = 1.0E-6$; *Mfng* ###$P = 0.00023$; *Neurl1a* #$P = 0.092$; *Dtx2* #$P = 0.051$; *Dtx3l* ###$P = 0.00014$; *Numb* #$P = 0.061$; *Pofut1* *$P = 0.019$, ##$P = 0.0049$; *Poglut1* #$P = 0.020$; *Maml1* *$P = 0.016$, ###$P = 0.00031$; *Maml2* #$P = 0.010$; *Cdkn1a* ***$P = 0.00033$, ###$P = 2.5E-6$; *Nrarp* ##$P = 0.0019$. Adjusted *P* value statistics determined by Benjamini-Hochberg procedure applied to two-sided limma differential expression values to control false discovery from multiple comparisons. Figure generated by Jeff Szymanski.

4.2 Transient Notch reactivation in adult murine cardiomyocytes persistently reprograms the ventricular electrical substrate

Previously, our lab reported that transient cardiomyocyte Notch activation resulted in persistent epigenetic and electrophysiologic changes that produced a conduction-like phenotype[111,120]. In these studies, Notch activation upregulated *Scn5a*, which encodes for $Na_V1.5$, and increased sodium current (I_{Na})-mediated cardiomyocyte membrane excitability[111]. To further determine whether cardiomyocyte Notch signaling can increase cardiac conduction, I utilized the Tet-on transgenic system to transiently and selectively express an inducible NICD (iNICD) to activate Notch in adult cardiomyocytes (*αMHC-rtTA*; *tetO_NICD*)[111,126]. Adult iNICD mice were fed doxycycline chow for 3 weeks to transiently activate Notch, followed by a minimum of 16 weeks

washout for iNICD turnover. This doxycycline pulse was chosen to sufficiently activate Notch while mimicking a transient dose of radiotherapy-induced activation.

When compared to littermate controls, longitudinal CVs of iNICD ventricles were significantly increased after 16-week washout (**Figure 4.3a, 4.3b**). However, the magnitude of this effect appeared to be smaller than the effect of radiation on conduction velocity, and there was no observed effect of iNICD expression on transverse conduction. In a separate cohort, mice were sacrificed after a 52-week washout to test whether Notch activation may be responsible for long-term, persistent upregulation of cardiac conduction proteins observed after IR. Western blotting revealed that transient activation of Notch signaling was associated with persistent increases in ventricular $Na_V1.5$ (**Figure 4.3c**), but not Cx43 (**Figure 4.3d**). These findings suggest that transient Notch activation may partially contribute to radiation-induced persistent upregulation of the cardiac sodium channel and are important to understanding a mechanism whereby a single dose of radiation could lead to permanent changes in the electrical substrate.

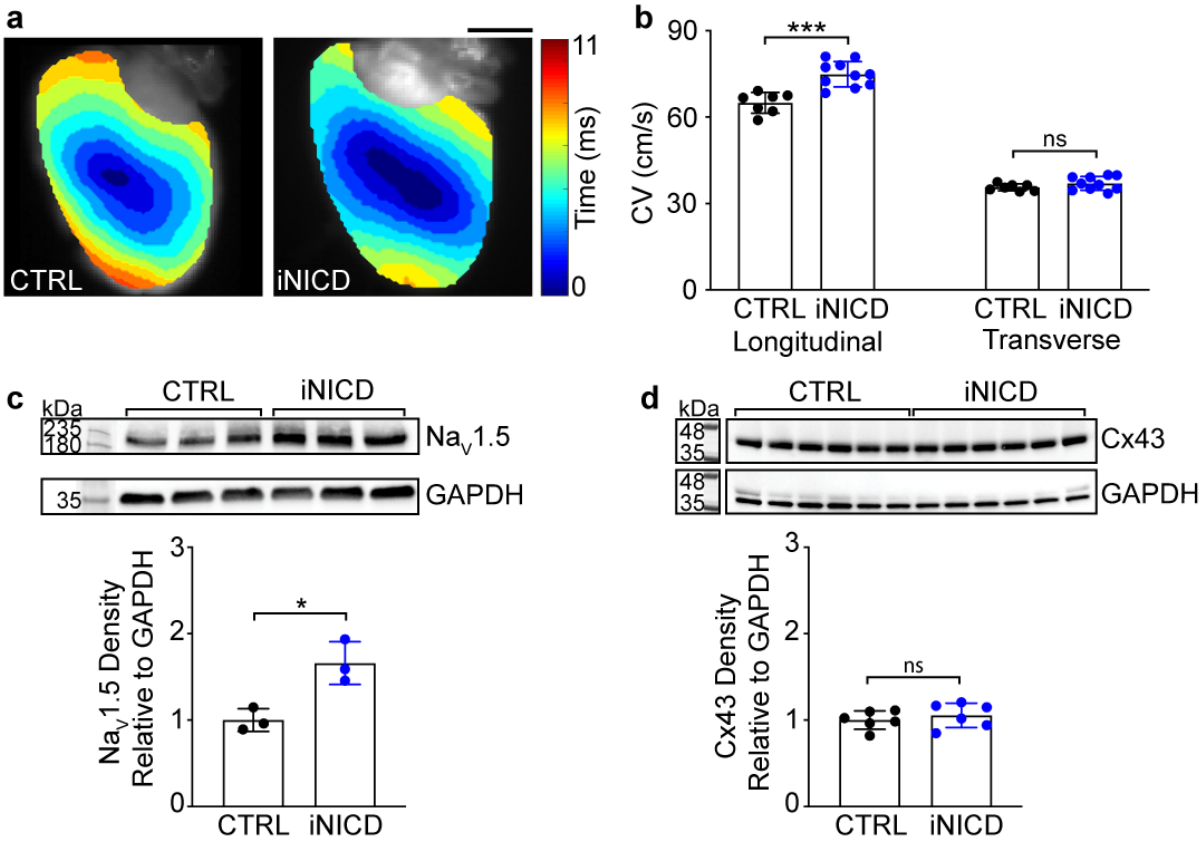

Figure 4.3. Transient iNICD-mediated, cardiomyocyte-specific Notch activation persistently increases conduction velocity and Na$_V$1.5 expression. (a) Representative activation maps and **(b)** conduction velocity measurements of control (CTRL, black) *αMHC-rtTA*; *tetO_NICD* (iNICD, blue) murine hearts after 3-week doxycycline induction and 16-week washout (n = 7 biologically independent CTRL mice; n = 9 biologically independent iNICD mice; Longitudinal ***P = 0.00019, Transverse P = 0.18). **(c-d)** Western blot and quantified densitometry from CTRL versus iNICD hearts after 3-week doxycycline induction, 52-week washout for Na$_V$1.5 (n = 3 biologically independent samples per condition, *P = 0.026) and Cx43 (n = 6 biologically independent samples per condition, P = 0.47, ladder was run in parallel on a separate gel to allow for quantitative comparisons on the same blot). All P values determined by two-way unpaired t-test. Optical mapping performed by Yun Qiao in the Rentschler Lab.

4.3 Loss of cardiomyocyte Notch signaling partially rescues conduction reprogramming after 25 Gy radiation

Notch signal transduction occurs following cleavage of the NICD and its translocation to the nucleus, where it binds to multiple transcriptional coactivators to elicit direct and indirect Notch-mediated effects. For these effects to occur, binding of NICD with a family of mastermind-like (MAML) transcriptional coactivators is necessary for formation of a functional DNA-binding complex to activate Notch-specific transcription. To test whether cardiomyocyte Notch signaling is not only sufficient but also necessary for reprogramming conduction after radiation, I utilized a cardiomyocyte-specific, inducible Notch loss-of-function (Notch iLOF) transgenic mouse model (*αMHC-MerCreMer* and $R26r^{dnMAML/+}$). Notch iLOF mice express a tamoxifen-inducible Cre recombinase under the cardiomyocyte-specific myosin heavy chain promoter, as well as a loxP-flanked STOP cassette upstream a dominant-negative mutant of the mastermind-like Notch transcriptional coactivator (*dnMAML*), which represses nuclear transactivation of the NICD[110]. Upon tamoxifen-induced Cre recombination, Notch iLOF mice permanently express *dnMAML* in cardiomyocytes to effectively and specifically knock out Notch signaling in a cell-autonomous manner[111]. Littermates expressing *αMHC-MerCreMer* and receiving tamoxifen but lacking the *dnMAML* mutant were used as controls.

Mice were treated with tamoxifen chow for ten days followed by a 28-day washout to resolve any potential transient cardiomyopathy induced by tamoxifen-mediated Cre activation in the *αMHC-MerCreMer* transgenic mouse lines, as previously described[134]. Following tamoxifen-induced Cre recombination and washout, Notch iLOF mice and intact littermate controls were subjected to 25

Gy radiation. In non-irradiated sham mice, there was no baseline difference in CV between control and Notch iLOF groups **(Figure 4.4a**), suggesting that loss of cardiomyocyte Notch signal transduction has not phenotypic effect at baseline. This finding is consistent with the longstanding consensus that Notch signaling becomes quiescent in adult cardiomyocytes. Indeed, 25 Gy radiation was associated with increases in CV, $Na_V1.5$, and Cx43 in both control and Notch iLOF mice, suggesting that loss of Notch signaling does not completely block the reprogramming effect (**Figure 4.4b, 4.4c, 4.4d**). However, Notch iLOF attenuated the overall effect size of the post-IR conduction increase by approximately 30%, resulting in significantly decreased CVs in Notch iLOF mice compared to littermate controls (**Figure 4.5a, 4.5b,** and **Figure 4.4e**). Following radiation, Notch iLOF mice expressed significantly decreased $Na_V1.5$ protein expression (**Figure 4.5c**) compared to irradiated littermate controls. Interestingly, there was no observed effect of loss of Notch signaling in Cx43 expression (**Figure 4.5d and Figure 4.4f**).

From this observed partial rescue, these data suggest that radiation-induced electrical reprogramming is partially regulated by Notch-induced upregulation of the cardiac sodium channel and not connexins. Indeed, intact Notch signaling is necessary for complete upregulation of *Scn5a* and $Na_V1.5$ in cardiomyocytes after 25 Gy IR.

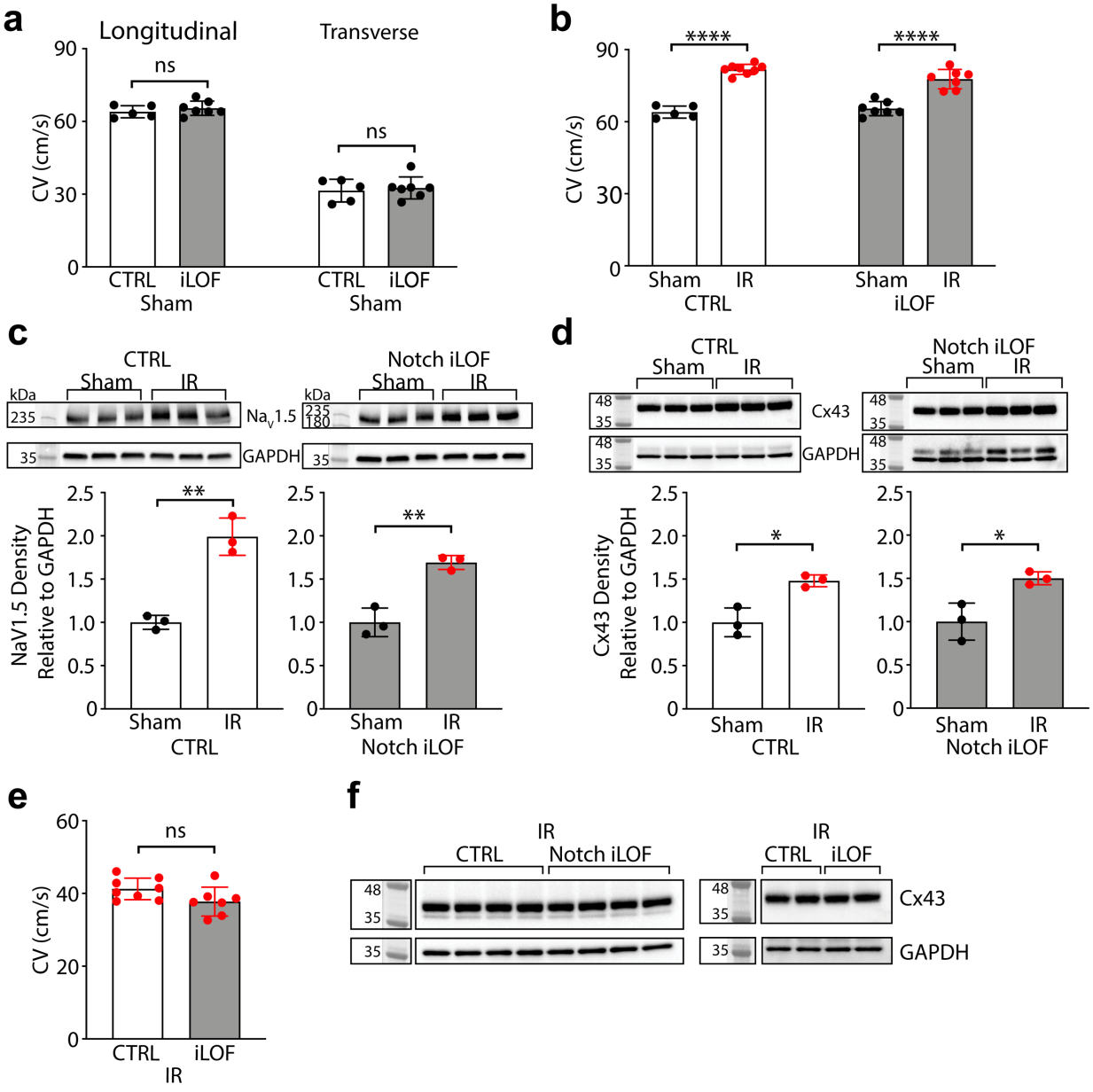

Figure 4.4. Loss of cardiomyocyte Notch does not fully prevent radiation-induced electrical reprogramming. (a) Conduction velocities of nonirradiated (sham) littermate control (CTRL, white bar, $n = 5$ biologically independent animals) and Notch iLOF (grey bar, $n = 7$ biologically independent animals) hearts reveal no baseline difference in conduction (Longitudinal $P = 0.38$; Transverse $P = 0.69$). **(b)** Longitudinal conduction velocities in sham (black points) versus IR (red dots) CTRL (sham, $n = 5$ biologically independent animals; IR, $n = 8$ biologically independent

animals; ****$P < 0.0001$) and Notch iLOF (sham, $n = 7$ biologically independent mice, versus IR, $n = 7$ biologically independent mice, ****$P < 0.0001$) mice. Values from Figure 7b and Figure 4.4a have been replotted for sham versus IR comparisons. **(c)** $Na_V1.5$ in CTRL and Notch iLOF mice in the presence and absence of radiation ($n = 3$ biologically independent samples per condition; CTRL **$P = 0.0017$; iLOF **$P = 0.0028$). **(d)** Cx43 in CTRL and Notch iLOF mice in the presence and absence of radiation ($n = 3$ biologically independent samples per condition; CTRL, *$P = 0.010$; iLOF *$P = 0.019$). **(e)** Transverse conduction velocity measurements of CTRL ($n = 8$ biologically independent animals) and Notch iLOF (n = 7 biologically independent animals) hearts at 6 weeks post-IR ($P = 0.072$). **(f)** Full Western blots of $n = 6$ biologically independent samples for Cx43 values plotted in Figure 7d. All bar graphs are represented as mean ± SD.

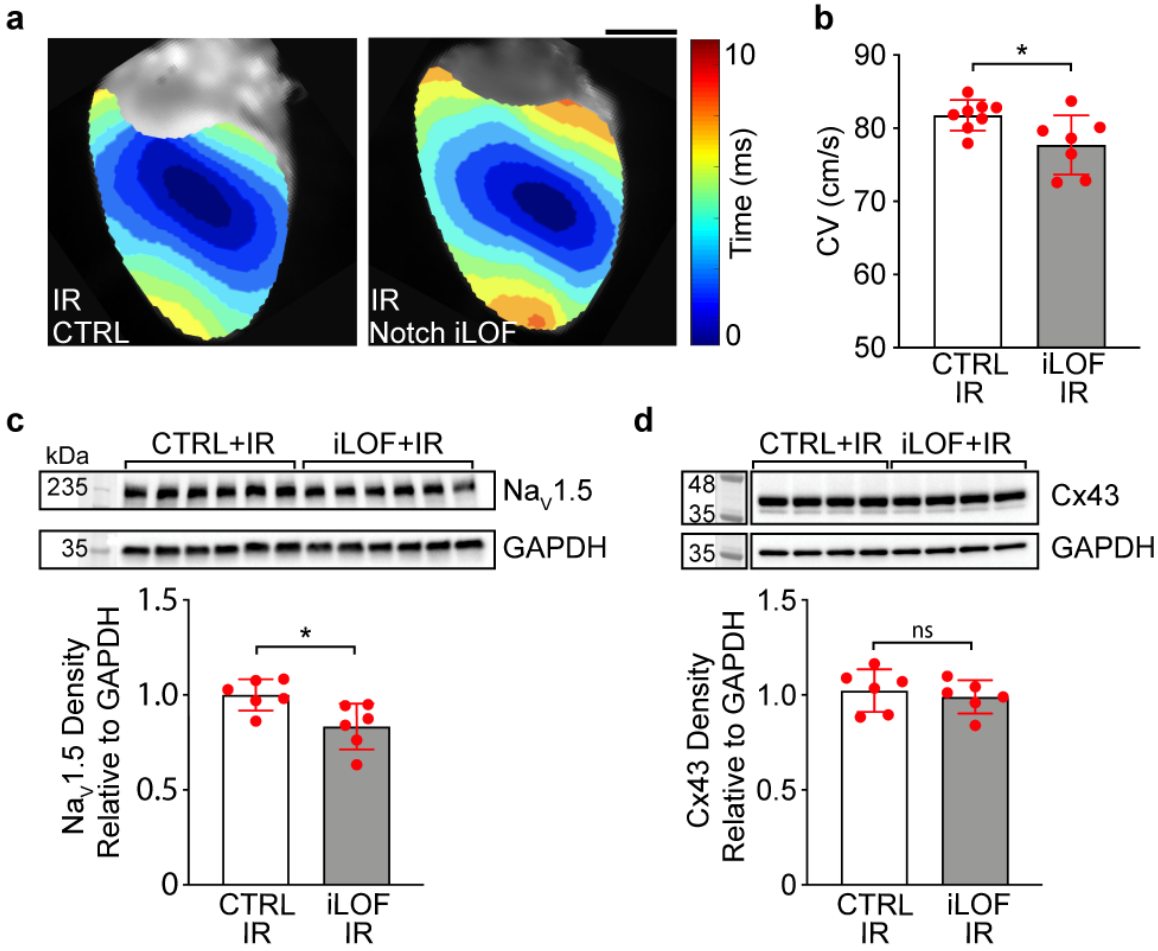

Figure 4.5. Loss of cardiomyocyte Notch signaling partially inhibits radiation-induced conduction reprogramming. (a) Representative activation maps and **(b)** longitudinal conduction velocity measurements of irradiated littermate control (left, CTRL, white bars) and *αMHC-MerCreMer*; *R26r*$^{dnMAML/+}$ (right, iLOF, grey bars) murine hearts at 6 weeks post-IR. $n = 8$ biologically independent CTRL mice; $n = 7$ biologically independent iLOF mice; $^*P = 0.027$. **(c-d)** Western blot and quantified densitometry of $Na_V1.5$ ($n = 6$ biologically independent samples per condition, $^*P = 0.012$) and Cx43 ($n = 6$ biologically independent samples per condition across two blots run in parallel, $P = 0.59$,). All P values determined by two-way unpaired t-test. All bar graphs are represented as mean ± SD.

Chapter 5: RT Effects on Cardiomyocyte Nuclear Morphology and Genome Accessibility

5.1 Twenty-five Gy IR upregulates *Scn5a* mRNA in cardiomyocytes and induces nuclear morphological changes

Because of the abundance of noncardiomyocyte cell types in the heart, I utilized RNA fluorescence *in situ* hybridization (FISH) targeting *Scn5a* and the cardiac ryanodine receptor *Ryr2* to supplement my bulk RNA sequencing results and quantify cardiomyocyte-specific transcriptional changes to sodium channel expression after radiotherapy. At 6 weeks post-IR, RNA FISH revealed an approximately 40% increase in the ratio of *Scn5a* to *Ryr2* messenger RNA within cardiomyocytes (**Figure 5.1a**). Additionally, there was a distinct increase in the number of *Scn5a* foci to nuclei in irradiated hearts compared to sham littermate controls (**Figure 5.1b**). Importantly, these data demonstrate that radiation- and/or Notch-mediated $Na_V1.5$ upregulation may be partially due to transcriptional reprogramming of *Scn5a* expression.

During analysis, irradiated nuclei appeared notably larger compared to sham controls. In mammals, postnatal cardiomyocytes quickly lose cytokinetic ability and transition to polyploid and/or multinuclear states[135,136]. Furthermore, cardiomyocyte nuclear ploidy increases in both aging and injury conditions[137,138]. It remains unclear whether changes in ploidy are adaptive or maladaptive, although it is presumed that increased DNA synthesis leads to increased transcriptional output. Due to the broad DNA-damaging effects of ionizing radiation, a nuclear

atypia has been described in many tumor types after radiotherapy[139,140]. Additionally, the presence of boxcar nuclei have been reported following cardiac RT[17], but it is unknown whether ventricular cardiomyocytes undergo specific changes in nuclear DNA content after ionizing radiation. Quantification of post-RT nuclear size revealed a significant increase in mean nuclear area as well as bimodal distribution of nuclear sizes at 6 weeks post-IR (**Figure 5.1c**).

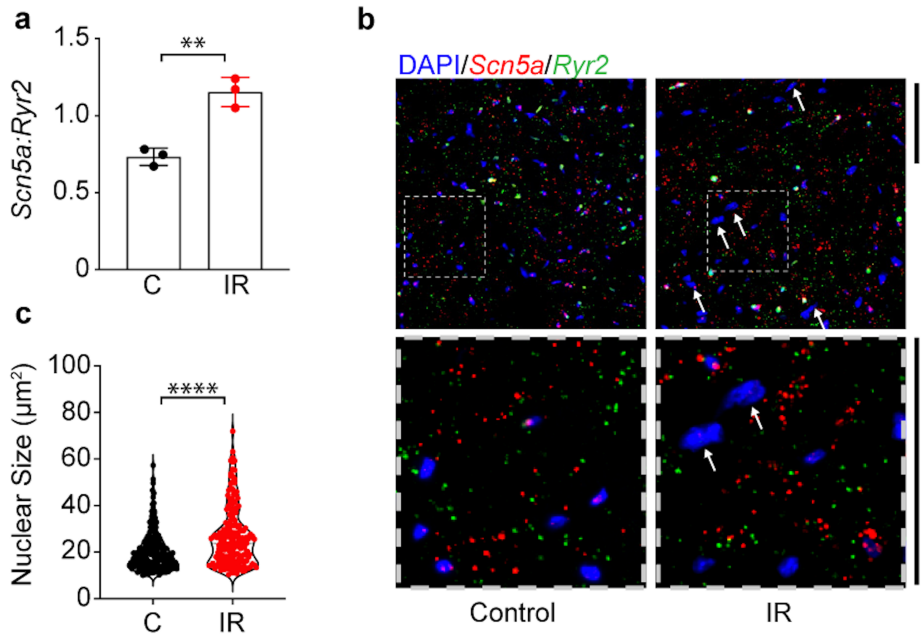

Figure 5.1 Twenty-five Gy IR upregulates *Scn5a* mRNA and increases cardiac nuclear size. **(a)** Ratio of *Scn5a* to *Ryr2* mRNA foci in control versus IR hearts at 6w post-IR by RNA ISH (n = 3 biological replicates per condition, $^{**}P$ = 0.0028). **(b)** RNA ISH for *Scn5a* (red) and *Ryr2* (green) mRNA in control (left) versus IR (right) murine hearts, co-stained with DAPI. Scale bars = 40 μm **(c)** Nuclear cross sectional areas in control versus IR hearts at 6w post-IR by DAPI fluorescence (n = 200 nuclei from 3 biologically independent replicates per condition, $^{****}P <$ 0.0001).

5.2 Radiation does not induce polyploidization of cardiomyocyte nuclei despite morphological changes

Indeed, if observed increases in nuclear size correlate with increases in nuclear DNA content and cardiomyocyte ploidy, these morphological changes may explain the observed post-RT bias toward increased transcription among DEGs on RNA-seq (**Figure 4.1a**). Importantly, cardiomyocytes account for only 40-50% of nuclei in the heart[112] but 70% of the volume and transcriptional output. To work around this limitation, dounce homogenization followed by fluorescence activated sorting for PCM1 present on cardiomyocyte nuclei is frequently utilized to profile cardiomyocyte-specific changes[112,141,142]. To test whether 25 Gy RT specifically affects cardiomyocyte nuclear DNA content and ploidy, I performed cardiomyocyte nuclei isolation using PCM1- and DAPI-based fluorescence-activated nuclei sorting (FANS) to enrich for cardiomyocyte nuclei[141–143] and quantify nuclear content. Previously, our lab used this technique to quantify increased ploidy distributions in the settings of heart failure and atrial fibrillation[112].

Surprisingly, FANS results revealed no difference in cardiomyocyte ploidy between IR and sham control hearts at 6 weeks post-IR in the PCM1-positive population (**Figure 5.2a, 5.2b**). To confirm that changes in nuclear size observed on RNA FISH occurred within cardiomyocyte nuclei, I performed follow-up immunofluorescent staining for PCM1 and DAPI on 6 week irradiated hearts to quantify the nuclear size distribution of PCM1-postive cardiomyocyte nuclei. In contrast to the RNA FISH images prepared from formalin-fixed, paraffin-embedded slides, immunolabeling with PCM1 was performed on unfixed, frozen sections due to technical limitations of PCM1 immunofluorescent staining on fixed tissue and resulted in slightly different distributions and

averages in nuclear size. Nonetheless, both PCM1-positive and PCM1-negative nuclei mean nuclear sizes were significantly increased compared to littermate controls, while PCM1-positive cardiomyocytes also exhibited and a bimodal distribution in nuclear sizes (**Figure 5.2c**). Overall, post-RT effects on nuclear size and shape were more apparent among PCM1-positive nuclei (**Figure 5.2c**, **5.2d**). Given that the observed changes in nuclear structure occur in the absence of changes in ploidy distribution, these findings suggest that the observed changes in nuclear shape/size may be due to differences in chromatin arrangement, rather than chromatin content.

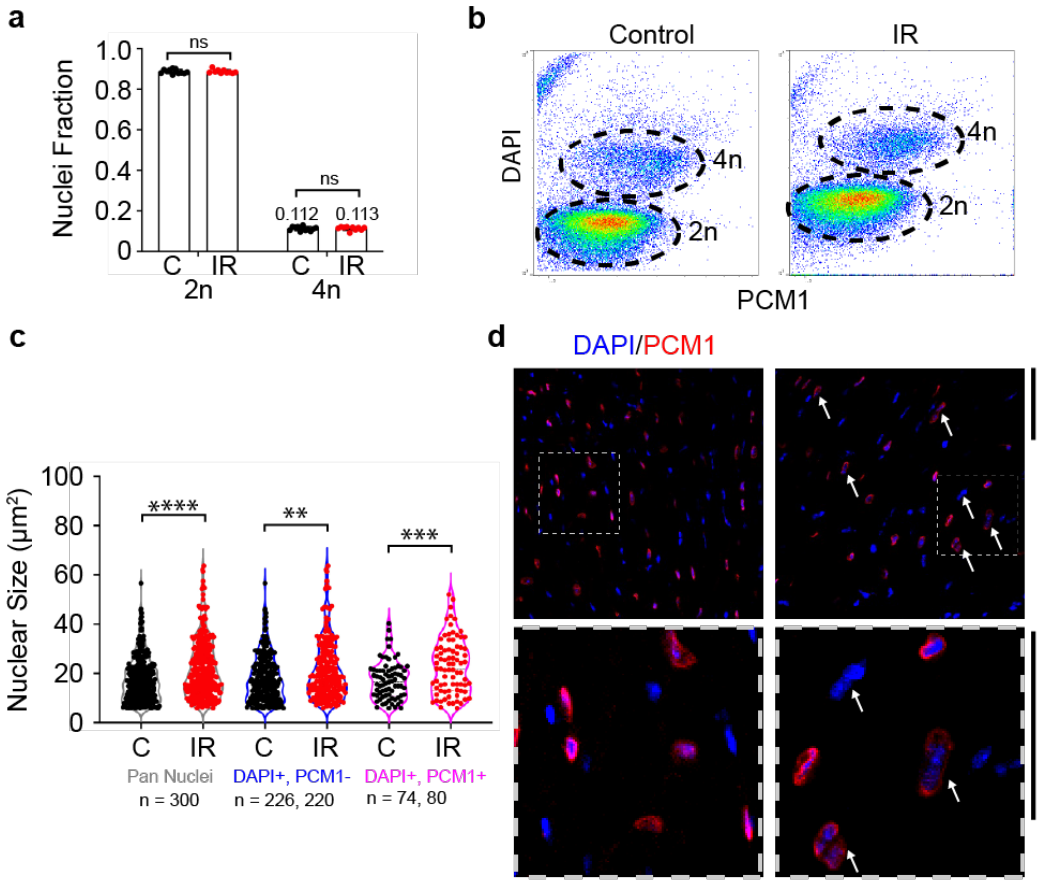

Figure 5.2. Twenty-five Gy IR does not increase cardiomyocyte nuclei ploidy despite increases in cardiomyocyte nuclear size. Cardiomyocyte nuclei were isolated from murine hearts at 6w post-IR and compared with littermate controls. **(a)** Nuclear ploidy distribution of control

versus irradiated PCM1-sorted nuclei (n = 12 biologically independent replicates per condition, P = 0.91) **(b)** Representative distribution of 2n (lower DAPI) versus 4n (higher DAPI) nuclei in the PCM1-positive population in control (left) versus IR (right) ventricles. **(c)** Nuclear cross sectional areas in control versus IR hearts at 6w post-IR by DAPI fluorescence subdivided into pan-nuclei (****P < 0.0001), DAPI-positive, PCM1-negative nuclei (**P = 0.0011), and DAPI-positive, PCM1-positive cardiomyocyte nuclei (***P = 0.00030). **(d)** Representative immunostaining of Control (left) versus IR (right) mouse hearts at 6w post-IR for PCM1 (red) and co-stained with DAPI (blue). Scale bars = 40 μm

5.3 The adult cardiomyocyte nuclear genome is compacted after DNA damage and repair

After cardiomyocyte DNA damage repair, it is unclear whether the pre-existing epigenomic landscape of the heart is fully restored or whether DNA-damage induced chromatin "scars" ultimately cause cardiomyocyte reprogramming. To determine whether radiation directly affects cardiomyocyte chromatin accessibility after DNA repair, I combined cardiomyocyte FANS with an Assay for Transposase-Accessible Chromatin with next-generation sequencing (ATAC-seq) approach. ATAC-seq was performed at 48h post-RT to assess for subacute chromatin accessibility after DNA repair is complete. Furthermore, 48h post-RT was chosen to maximize cardiomyocyte-specificity on FANS due to the expectation that 25 Gy IR would be sufficient to ablate most dividing, tissue-resident noncardiomyocytes. Tagmentation and sequencing of PCM1-positive cardiomyocyte nuclei at 48h post-RT revealed compaction of cardiomyocyte chromatin accessibility (**Figure 5.3a**), with a 15% decrease in overall genome accessibility, measured by

accessible megabases, in post-RT cardiomyocyte nuclei compared to sham controls (**Figure 5.3b**). This observed genome compaction appeared to be global, with differential compaction annotated to promoter, intronic, exon, and distal intergenic regions of DNA (**Figure 5.3c** and **Table 5.1**). While chromatin compaction is known to occur in response to ATM signaling shortly after radiation (minutes to hours)[144,145], continued compaction at 48h after DNA repair was not previously tested. Previously, a 30% decrease in overall accessibility was reported at 6h after lower-dose, ultraviolet radiation exposure to NIH3T3 fibroblast cell lines[145]. Ongoing bioinformatics studies in the Rentschler lab are attempting to identify transcription factor binding using HOMER analysis. To test whether effects of RT on cardiomyocyte chromatin accessibility were persistent or dynamic, I attempted to repeat this FANS+ATAC-seq approach at 6w post-IR. Unfortunately, though PCM1 is the *de facto* cardiomyocyte nuclei marker for al *in vivo* studies, PCM1-based sorting was only sufficient to enrich for cardiomyocyte nuclei without complete exclusion of noncardiomyocyte. Consequently, the PCM1-based sorting still included up to 10% of noncardiomyocyte nuclei based on previous single-nuclei RNA sequencing approaches[146]. Due to the strong inflammatory response observed in the heart at 6w post-IR by RNA-seq (**Figure 4.2a**), PCM1-sorted ATAC-seq libraries at this 6w experimental timepoint were confounded by the presence of noncardiomyocyte nuclei, despite multiple rounds of technical optimization, and thus limited the reliability of subsequent analysis (data not shown). Overall, these results suggest that cardiomyocyte nuclear chromatin accessibility is highly sensitive to DNA damage and repair in the acute phase. Further studies are warranted in pure populations of post-mitotic cardiomyocyte, and/or in the absence of post-IR inflammation, to test the durability and dynamics of cardiomyocyte nuclear chromatin accessibility after single-fraction, high dose IR.

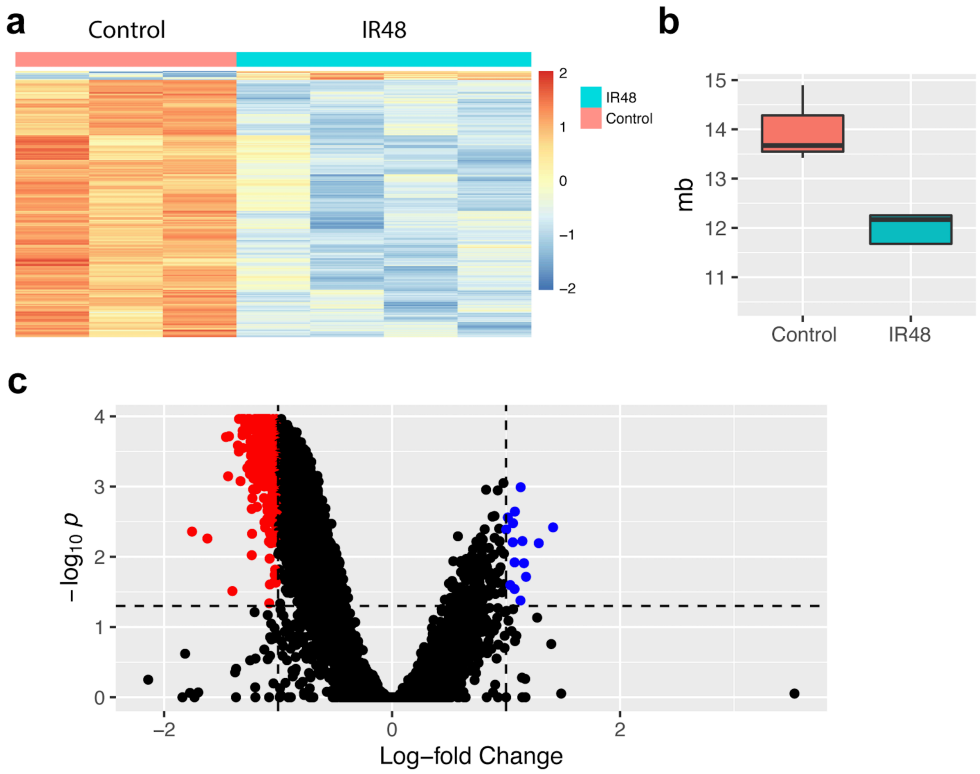

Figure 5.3. The cardiomyocyte nuclear genome is globally compacted after radiation-induced DNA damage and repair. (a) Heat map of all differentially accessible domains in control versus IR cardiomyocyte nuclei at 48h post-IR. **(b)** Open genome in megabases derived from MACS2 broad peak calls in control (left, red) versus 48h post-IR (IR48, right, blue) nuclei. **(c)** Volcano plot showing fold change and significance of all chromatin domains. Statistically-significant increases or decreases in accessibility are highlighted in red and blue, respectively.

Gene	Gene Name	logFC	Padj	annotation
Smco2	single-pass membrane protein with coiled-coil domains 2	-4.085	5.990E-13	Distal Intergenic
Ppfibp1	PTPRF interacting protein, binding protein 1 (liprin beta 1)	-3.235	7.292E-13	Promoter (<=1kb)
Ppfibp1	PTPRF interacting protein, binding protein 1 (liprin beta 1)	-3.379	5.265E-10	Intron
LOC115486561	U6 spliceosomal RNA	-2.734	4.899E-09	Promoter (1-2kb)
LOC115486562	U6 spliceosomal RNA	-2.071	7.732E-07	Distal Intergenic
Trim55	tripartite motif-containing 55	2.174	7.941E-07	Intron
Srsf3	serine/arginine-rich splicing factor 3	-2.087	1.291E-06	Promoter (<=1kb)
Dynlrb2	dynein light chain roadblock-type 2	-2.148	1.528E-06	Intron
2810001G20Rik	RIKEN cDNA 2810001G20 gene	-2.125	2.818E-06	Distal Intergenic
Gm14410	predicted gene 14410	-1.936	8.829E-06	Promoter (<=1kb)
Fkbp5	FK506 binding protein 5	-1.907	9.415E-06	Intron
Mthfr	methylenetetrahydrofolate reductase	-2.256	9.415E-06	Promoter (<=1kb)
Gtf2h4	general transcription factor II H, polypeptide 4	-2.682	3.339E-05	Promoter (<=1kb)
Etfrf1	electron transfer flavoprotein regulatory factor 1	2.685	3.339E-05	Promoter (<=1kb)
Slco5a1	solute carrier organic anion transporter family, member 5A1	1.869	4.517E-05	Intron
Carmil1	capping protein regulator and myosin 1 linker 1	-1.741	4.241E-04	Intron
Mc3r	melanocortin 3 receptor	1.670	6.192E-04	Distal Intergenic
Vps13d	vacuolar protein sorting 13D	-1.574	1.433E-03	Promoter (<=1kb)
Enpp4	ectonucleotide pyrophosphatase/phosphodiesterase 4	-1.751	1.503E-03	Distal Intergenic
Stk38	serine/threonine kinase 38	-1.611	1.552E-03	Promoter (<=1kb)
Tmtc1	transmembrane and tetratricopeptide repeat containing 1	-1.597	1.552E-03	Intron
Rab7	RAB7, member RAS oncogene family	-1.604	1.742E-03	Distal Intergenic
Tardbp	TAR DNA binding protein	1.659	1.886E-03	Promoter (<=1kb)
Ppara	peroxisome proliferator activated receptor alpha	-1.492	2.578E-03	Intron

Gm5114	predicted gene 5114	-1.659	3.030E-03	Promoter (1-2kb)
Spsb1	splA/ryanodine receptor domain and SOCS box containing 1	-1.655	3.142E-03	Promoter (<=1kb)
Pibf1	progesterone immunomodulatory binding factor 1	-1.534	4.154E-03	Intron
Txnip	thioredoxin interacting protein	-1.463	4.273E-03	Promoter (<=1kb)
St3gal6	ST3 beta-galactoside alpha-2,3-sialyltransferase 6	-1.532	5.317E-03	Intron
Nampt	nicotinamide phosphoribosyltransferase	-1.539	5.477E-03	Distal Intergenic
Wdr45b	WD repeat domain 45B	-1.447	8.926E-03	Intron
Cers6	ceramide synthase 6	-1.471	9.255E-03	Exon
Mir7219	microRNA 7219	-1.463	9.906E-03	Intron
Tcp11	t-complex protein 11	2.215	1.068E-02	Distal Intergenic
Tgfbr3	transforming growth factor, beta receptor III	-1.442	1.084E-02	Intron
LOC115486954	uncharacterized LOC115486954	-1.428	1.084E-02	Intron
Ube4b	ubiquitination factor E4B	-1.779	1.120E-02	Downstream (<1kb)
Zfyve21	zinc finger, FYVE domain containing 21	-1.407	1.363E-02	Intron
Slc25a13	solute carrier family 25 (mitochondrial carrier, adenine nucleotide translocator), member 13	-1.395	1.524E-02	Intron
Bcl2l1	BCL2-like 1	-1.353	1.539E-02	Intron
Mxd4	Max dimerization protein 4	-1.291	1.829E-02	Intron
Mt1	metallothionein 1	-1.372	1.829E-02	Distal Intergenic
Gpr157	G protein-coupled receptor 157	-1.392	1.956E-02	Promoter (<=1kb)
Tacc2	transforming, acidic coiled-coil containing protein 2	-1.375	2.021E-02	Intron
Olfr554	olfactory receptor 554	1.702	2.149E-02	Distal Intergenic
Hhat	hedgehog acyltransferase	-1.353	2.234E-02	Intron
Rnf144b	ring finger protein 144B	-1.359	2.234E-02	Intron
Ankrd33b	ankyrin repeat domain 33B	-1.300	2.234E-02	Intron
Agtpbp1	ATP/GTP binding protein 1	-1.349	2.487E-02	Intron
Ppp2r3a	protein phosphatase 2, regulatory subunit B", alpha	-1.374	2.487E-02	Promoter (1-2kb)
LOC115487700	U5 spliceosomal RNA	-1.335	2.636E-02	Intron
Erich3	glutamate rich 3	-1.349	2.636E-02	Intron

Lepr	leptin receptor	1.363	2.636E-02	Promoter (1-2kb)
Rptor	regulatory associated protein of MTOR, complex 1	-1.317	2.917E-02	Intron
Tacc2	transforming, acidic coiled-coil containing protein 2	-1.323	2.942E-02	Intron
Swt1	SWT1 RNA endoribonuclease homolog (S. cerevisiae)	-1.324	2.953E-02	Promoter (<=1kb)
Fstl4	follistatin-like 4	-1.330	2.953E-02	Intron
Filip1l	filamin A interacting protein 1-like	-1.315	2.953E-02	Intron
Fam205a2	family with sequence similarity 205, member A2	-1.328	2.953E-02	Distal Intergenic
Zfp82	zinc finger protein 82	-1.331	2.953E-02	Promoter (<=1kb)
LOC115486561	U6 spliceosomal RNA	-1.468	2.953E-02	Intron
Foxo3	forkhead box O3	-1.329	3.024E-02	Intron
Mir30c-2	microRNA 30c-2	-1.271	3.143E-02	Distal Intergenic
Mir7212	microRNA 7212	-1.313	3.172E-02	Intron
Kif28	kinesin family member 28	-1.313	3.318E-02	Exon
LOC115489780	U6 spliceosomal RNA	-1.309	3.337E-02	Promoter (2-3kb)
Dhx16	DEAH (Asp-Glu-Ala-His) box polypeptide 16	-1.427	3.361E-02	Promoter (<=1kb)
Tgfbr2	transforming growth factor, beta receptor II	-1.344	3.447E-02	Distal Intergenic
Cryzl2	crystallin zeta like 2	-1.258	3.463E-02	Distal Intergenic
Podn	podocan	-1.273	3.613E-02	Promoter (1-2kb)
Tcp11l2	t-complex 11 (mouse) like 2	-1.308	3.686E-02	Intron
Ppargc1a	peroxisome proliferative activated receptor, gamma, coactivator 1 alpha	-1.357	3.686E-02	Promoter (<=1kb)
Foxp1	forkhead box P1	-1.197	3.686E-02	Intron
Rps4l	ribosomal protein S4-like	-1.358	3.686E-02	Intron
Dhrs3	dehydrogenase/reductase (SDR family) member 3	-1.276	3.724E-02	Distal Intergenic
Pdk4	pyruvate dehydrogenase kinase, isoenzyme 4	-1.334	3.724E-02	Distal Intergenic
Chrna2	cholinergic receptor, nicotinic, alpha polypeptide 2 (neuronal)	-1.259	3.900E-02	Promoter (<=1kb)
LOC115488707	U1 spliceosomal RNA	-1.350	3.900E-02	Distal Intergenic
Mdc1	mediator of DNA damage checkpoint 1	-1.409	4.016E-02	Promoter (<=1kb)
Zfp873	zinc finger protein 873	-1.399	4.023E-02	Distal Intergenic

Tctn1	tectonic family member 1	-1.254	4.135E-02	Exon
Sparc	secreted acidic cysteine rich glycoprotein	-1.185	4.137E-02	Promoter (<=1kb)
Cobll1	Cobl-like 1	-1.309	4.261E-02	Intron
BB218582	expressed sequence BB218582	-1.334	4.261E-02	Promoter (1-2kb)
Ank3	ankyrin 3, epithelial	-1.285	4.483E-02	Intron
Fntb	farnesyltransferase, CAAX box, beta	-1.277	4.483E-02	Promoter (2-3kb)
Got1	glutamic-oxaloacetic transaminase 1, soluble	-1.174	4.483E-02	Distal Intergenic
Gm15441	predicted gene 15441	-1.279	4.483E-02	Promoter (2-3kb)
Tbc1d1	TBC1 domain family, member 1	-1.279	4.483E-02	Intron
Rasd2	RASD family, member 2	-1.270	4.483E-02	Distal Intergenic
Myzap	myocardial zonula adherens protein	-1.119	4.483E-02	Intron
Kcnh2	potassium voltage-gated channel, subfamily H (eag-related), member 2	-1.224	4.603E-02	Promoter (1-2kb)
4933413L06Rik	RIKEN cDNA 4933413L06 gene	-1.405	4.820E-02	Intron
Scn3a	sodium channel, voltage-gated, type III, alpha	-1.362	4.820E-02	Distal Intergenic
Ppargc1a	peroxisome proliferative activated receptor, gamma, coactivator 1 alpha	-1.303	4.820E-02	Intron
Agtpbp1	ATP/GTP binding protein 1	-1.191	4.982E-02	Intron
Trib1	tribbles pseudokinase 1	-1.120	4.982E-02	Distal Intergenic
Fkbp5	FK506 binding protein 5	-1.305	4.982E-02	Intron
E130215H24Rik	RIKEN cDNA E130215H24 gene	-1.231	5.029E-02	Intron
Neu1	neuraminidase 1	-1.494	5.329E-02	Promoter (<=1kb)
Ppp1r11	protein phosphatase 1, regulatory inhibitor subunit 11	-1.775	5.329E-02	Promoter (<=1kb)

Table 5.1 Top 100 genes of differential chromatin accessibility at 48h post-IR. Top differentially accessible genes and domain annotations by adjusted *P* value in control versus 48h post-IR nuclei. Negative logFCs denote decrease in chromatin accessibility.

Chapter 6: Molecular and Functional Effects of RT in Human Electrophysiology

Within this dissertation thus far, I have presented substantial evidence to suggest that single-fraction, high dose IR to post-mitotic cardiomyocytes in the heart induces rapid electrical conduction reprogramming in the absence of transmural fibrosis. Indeed, these effects described may prevent arrhythmias by restoring electrical conduction to prevent reentry. To translate my preclinical findings into patients receiving RT for treatment of VT, I asked whether radiation is sufficient to upregulate $Na_V1.5$ and/or Cx43 in a patient's explanted heart previously targeted with 25 Gy, compared to a nontargeted remote region within the same failing heart. At the time of Patient F's heart transplant due to refractory nonischemic heart failure (965 days post-RT), I collected the superior portion of the basal left ventricle (American Heart Association, Segment 1), which was previously targeted with 25 Gy, for flash freezing, and I used the inferior-mid left ventricle (American Heart Association, Segment 10), which received less that 5 Gy radiation exposure (**Figure 7.1**), as a nontargeted control **(Figure 7.2a)**.

6.1 Cardiac RT durably upregulates $Na_V1.5$ in one explanted nonischemic cardiomyopathic heart

To control for potential baseline regional differences in protein expression, matched tissue from segments 1 and 10 were collected from 2 non-failing donor hearts that were rejected for transplantation. Overall, I observed that the level of $Na_V1.5$ in the nontargeted region (Segment 10) of this nonischemic failing heart was much lower than in analogous segments of nonfailing

donor hearts **(Figure 7.2b)**, consistent with known reductions in $Na_V1.5$ in the setting of HF[81,147–149]. After 965 days post-RT, I observed 3-fold higher levels of $Na_V1.5$ within the targeted myocardium when compared to the remote region in Patient F's heart, restoring $Na_V1.5$ in the targeted region to levels analogous to non-failing ventricles (**Figure 7.2b**). In this nonischemic cardiomyopathy, there was no observed decrease in levels of Cx43 at baseline, and likewise no observed difference in Cx43 between the targeted and nontargeted segments (**Figure 7.2c**). Differential expression between $Na_V1.5$ and Cx43 within these regions could potentially be explained by heterogeneous gap junction remodeling in nonischemic HF when compared to ischemic HF[150].

6.2 Radiation-induced electrical reprogramming in patients may be detected by QRS durations on electrocardiogram

Next, our group analyzed serial surface ECGs of patients who received cardiac RT. In contrast to the mouse, where the whole heart is irradiated, only the arrhythmogenic region of a patient's heart is targeted. Thus, not all RT patients would be expected to exhibit a shortened QRS duration. Even still, a statistically nonsignificant difference in QRS durations within the 19-patient cohort was observed by 6 weeks post-RT (149 ± 34 ms pre-RT versus 139 ± 32 ms post-RT, $n = 19$, $P = 0.072$, **Figure 7.2d**). Overall, compared to baseline intervals, post-RT QRS durations were shorter in 13 patients and longer in 5 patients **(Figure 7.2d)**. As an example, Patient G's QRS shortened from 165 ms with left bundle branch block (LBBB) to a QRS interval of 130 ms without LBBB, and this QRS remained shorted for at least 6 months (**Fig 7.2e**). Consistent with the preclinical data

presented in mice, these ECG changes may be potential examples of radiation-induced functional electrical reprogramming in humans.

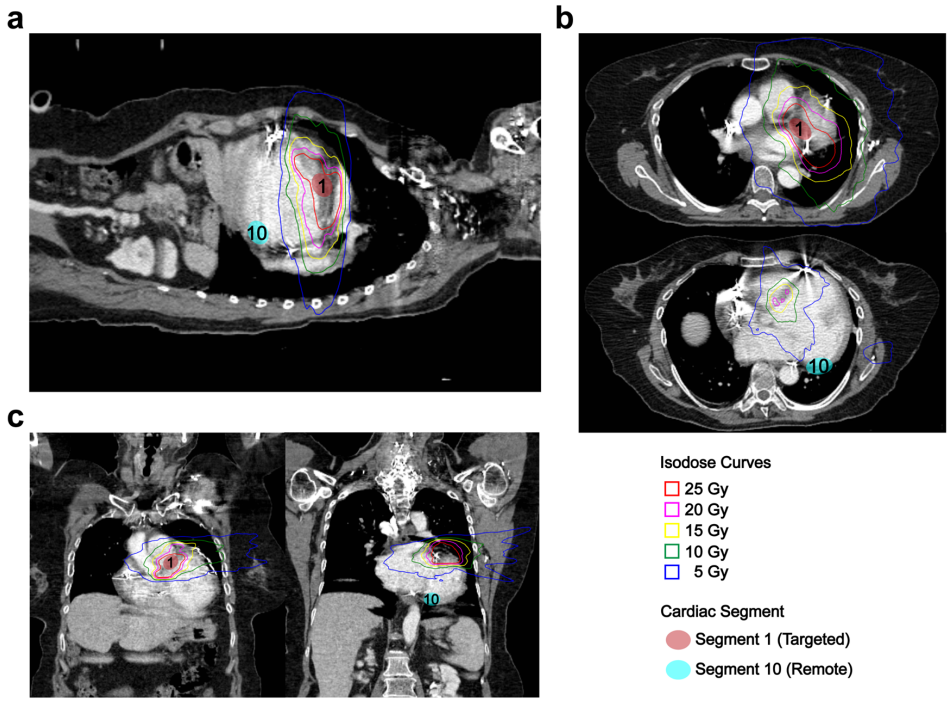

Figure 6.1. Remote, nontargeted heart specimens collected from cardiac RT patients received minimal radiation exposure. (a-c) Orthogonal views of Patient F's radiation treatment plan overlayed with isodose curves. The anterior basal LV, corresponding to Segment 1, was previously treated with 25 Gy and collected at time of explant; the posterior mid-LV, corresponding to Segment 10, was collected as a remote, nontargeted control. Segment 1 was within the 25 Gy isodose line (red), while Segment 10 was outside of the 5 Gy isodose line (blue).

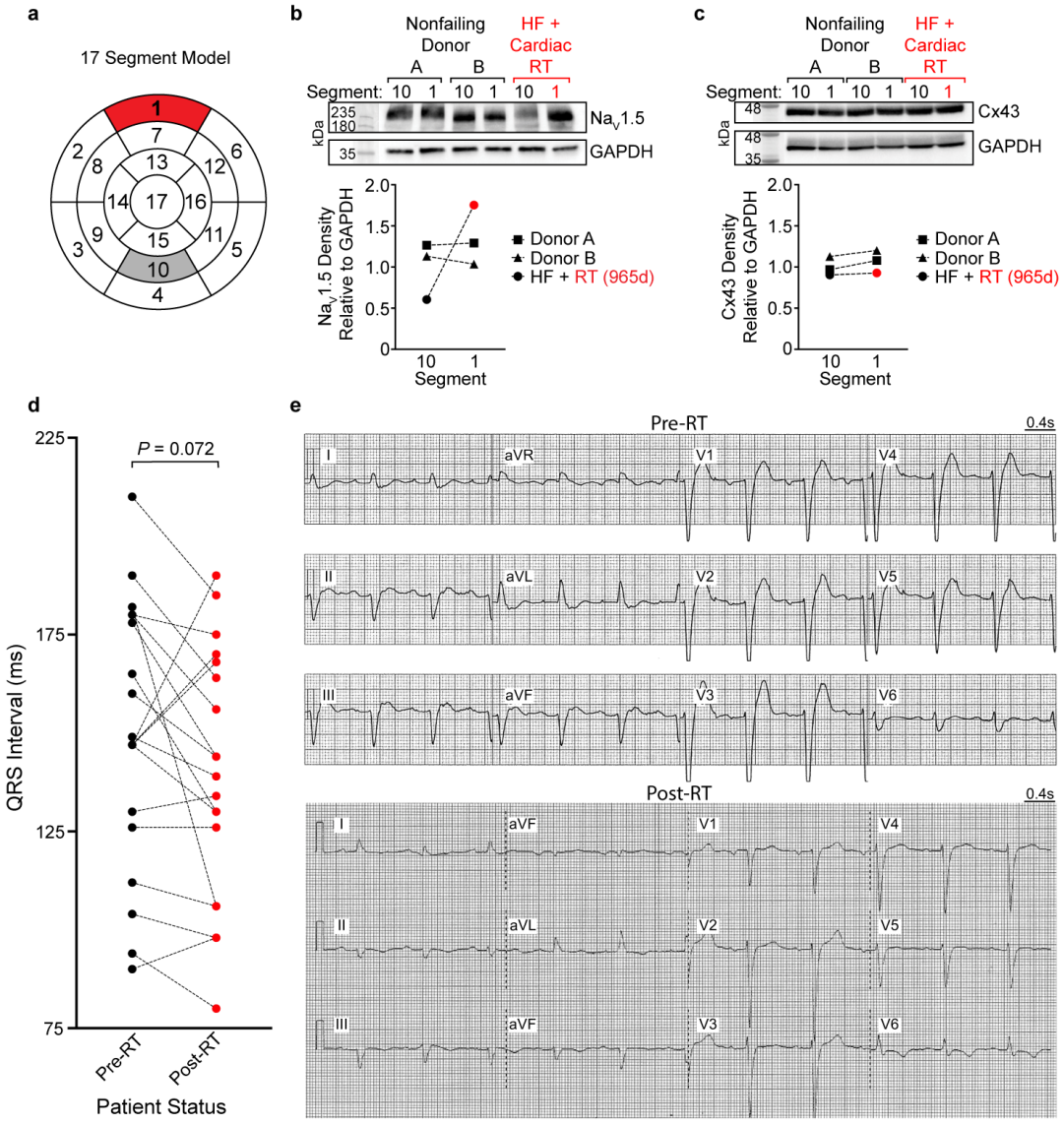

Figure 6.2. Reprogramming in VT patients treated with 25 Gy RT. (a) American Heart Association's cardiac 17-segment model illustrating 25 Gy targeted (Segment 1, red) and remote nontargeted (Segment 10, grey) myocardium collected from a heart failure patient with nonischemic cardiomyopathy and VT (Patient F), who previously received cardiac RT. The nontargeted Segment 10 received less than 5 Gy radiation exposure. For comparison, corresponding Segments 1 and 10 were collected from 2 nonfailing, non-RT donor hearts rejected for transplantation. **(b)** Western blot and quantified densitometry of Na$_V$1.5 in Segment 10 versus

Segment 1 of nonfailing (Donors A and B) and RT-treated (HF+Cardiac RT, red) hearts. (**c)** Western blot and quantified densitometry of Cx43 in Segment 10 versus Segment 1 of nonfailing and RT-treated hearts. **(d)** Matched QRS durations in the ENCORE-VT patient cohort at baseline (pre-RT, 149 ± 34 ms) versus 6-week post-RT (139 ± 32 ms) timepoints (n = 19 paired individual patients, P = 0.072 by two-tailed Wilcoxon signed-rank test). **(e)** Representative twelve-lead ECG of robust QRS shortening recorded from Patient G at the time of RT treatment, with a baseline QRS of 165 ms and presence of LBBB, and then after 6 months post-RT, exhibiting shortened QRS (130 ms) and resolution of LBBB.

Chapter 7: Materials and Methods

7.1 Study design

This dissertation aimed to determine the structural, electrophysiologic, molecular, and epigenetic effects of single fraction ionizing radiation on the adult mammalian heart. To this end, I utilized several experimental approaches. In fibrosis studies, I characterized levels of fibrosis in irradiated human and murine myocardium. In electrophysiologic studies, I studied effects and mechanisms of cardiac ventricular conduction increase following 25 Gy ionizing radiation in healthy and diseased murine myocardium and following doxycycline-induced activation of Notch signaling and tamoxifen-induced loss of Notch signaling in cardiomyocytes. I also studied the effects of radiation on cardiomyocyte nuclear atypia and ploidy and explored subacute effects of radiation on cardiomyocyte chromatin accessibility and reprogramming. I also show examples of sodium channel upregulation in 1 of 1 and potential QRS duration changes in VT patients treated with 25 Gy RT.

In patients, total sample size was powered to demonstrate acute safety and preliminary efficacy of noninvasive radiation therapy for treatment of refractory ventricular tachycardia under the Electrophysiology-guided Noninvasive Cardiac Radioablation for VT (ENCORE-VT, NCT02919618) clinical trial, a single-arm Phase I/II trial, in which 19 patients were enrolled and treated[18]. Patients with refractory ventricular tachycardia (VT) (i.e. failed at least one catheter ablation or was contraindicated to catheter ablation and failed/became intolerant to at least one anti-arrhythmic medication) and met all inclusion/exclusion criteria were enrolled into the study.

Patient-level data were restricted to paired, binary intra-patient comparisons (non-targeted versus targeted and/or pre-treatment versus post-treatment).

For studies in mice, power analyses were used to determine minimum group sizes *a priori*. These power calculations were performed using G*power (v.3.1.9). The sample size calculation for each cohort was based on a *t*-test to observe changes in CV or ERP. A study with an effect size of 0.25 and a power of 80% required a minimum of $n = 6$ per group to test this difference at 5% significance using a two-tailed test. Mice were randomized to treatment condition and both male and female littermates were used for all experiments. For experiments which used aged mice or when surgery was performed, I initially overpowered these cohorts in anticipation of procedure-related death such that there would be adequate power at the experimental endpoint. For Western blot on samples obtained from wild-type and iNICD mice, a study with an effect size of 0.80 and power of 80% was initially chosen and required a minimum of $n = 3$ independent biological replicates per group to test this difference at 5% significance using a two-tailed test. In anticipation of a smaller effect size in Notch LOF rescue experiments, a study was designed to test for an effect size of 0.25 and power of 80%, and these also required a minimum of $n = 6$ independent biological replicates per group. This sample size was also subsequently used to power a test for Cx43 expression in iNICD mice when effect size appeared lower than the $Na_V1.5$ effect size. For RNA sequencing, an $n = 6$ biologically independent samples per group was chosen to detect meaningful transcriptional changes in heart tissue based on previous publications[151].

7.2 Human specimen and data collection

This study's clinical component was approved by the Washington University School of Medicine Institutional Review Board (IRB). Patient samples and data were collected under the ENCORE-VT clinical trial. Only patients who provided informed consent prior to specimen collection were included, and all human specimen experiments were performed in accordance with IRB-approved analyses. At the time of heart transplant or death (autopsy), whole heart specimens were obtained from patients who previously underwent noninvasive cardiac radiation for treatment of refractory VT and consented to specimen collection. Each specimen was compared with its corresponding radiation treatment plan to identify regions of the heart that were either treated with 25 Gy (targeted), or anatomically distant from radiation (remote). Across all samples, remote regions of myocardium received radiation exposure that was less than 5 Gy. In specimens obtained from autopsy, targeted and remote regions of patient hearts were resected and fixed in 10% formalin upon collection for histopathology. In one explanted heart collected from transplant, targeted and nontargeted tissue were flash frozen immediately at time of explant for molecular experiments and protein measurements. Remaining specimens obtained from autopsy and formalin-fixed were neither flash frozen nor collected for protein measurements, as these specimens were obtained days after death, during which substantial protein degradation was expected, and were only appropriate for clinical histopathology. Cardiac MRIs were taken according to the ENCORE-VT clinical trial guidelines. Two patients were treated as part of our institution's previously-published case series[17] prior to establishment of the ENCORE-VT clinical trial and for whom MRI was not taken. While quantification of fibrosis using gadolinium enhancement was not feasible due to the presence of imaging artifacts, I include a representative set of images from a single patient that illustrates the lack of any observed change in fibrosis or cardiac injury in this patient cohort.

Patient ECG Interpretation Pre- and Post-RT patient ECGs were taken according to the ENCORE-VT clinical trial (NCT02919618). QRS intervals were measured independently by two blinded investigators, and values obtained were subsequently compared and verified against one another. While some patients exhibited smaller changes in pre- versus post-RT QRS intervals, robust QRS shortening was strictly defined as a decrease in the QRS interval by at least 25ms on serial surface ECGs.

Human Specimen Fibrosis Quantification Trichrome-stained fixed human specimens were scanned into high resolution SVS image files using an Aperio ImageScope (v.12.1 Leica Biosystems). SVS image files contain seven magnification levels stored as Gaussian pyramids. All fibrosis quantification was performed using MATLAB (2017b, MathWorks) through a four-step process of sampling, preprocessing, quantization, and calculation[152]. In the sampling step, each SVS file was parsed into 900 equally-spaced 50px-by-50px images that span the entire high-resolution file in order to allow for parallelization of analysis and prevent out-of-memory errors. Next, preprocessing was performed using simple linear iterative clustering with a compression ratio of 1:50, to generate superpixels while preserving tissue boundaries[153]. Image files were subsequently converted from the RGB Colorspace to the L*a*b* Colorspace for image representation that is independent of brightness and illumination, which may vary across samples that were subject to differences in sample thickness, microscope settings, and batch-dependent differences during staining. Quantization subsequently defined pixel parameters which corresponded to areas of collagen, red blood cells, myocytes, or background, as defined by K-means[154]. Parameters were chosen based on the results obtained from four training samples and

kept constant for all computations. All pixels were then assigned to their corresponding category using Lloyd-Max algorithms[155]. Overall, percent fibrosis was defined by the relationship $fibrosis = \frac{Area_{collagen}}{Area_{collagen}+Area_{RBC}+Area_{myocytes}}$. For fibrosis analyses, the mean computation time was approximately 50 minutes per sample. Fibrosis code and analysis was performed by Uri Goldsztejn in the Rentschler Lab.

7.3 Mouse Studies

Adult male and female littermate outbred wild-type CD-1 mice were purchased (Charles River Laboratories, Wilmington MA). iNICD (*αMHC-rtTA* and *tetO_NICD*)[120,126] and Notch iLOF (*αMHC-MerCreMer* and *R26r*$^{dnMAML/+}$)[111] mice were maintained on a mixed genetic background. iNICD and Notch iLOF mice were genotyped for *rt*TA/*tetO_NICD* and Cre/*Rosa26r*, respectively. In all experiments, age- and gender-matched littermate control animals were used for comparison. In all IR experiments, CD-1 mice aged 8 weeks or greater were used. For experiments involving conditional iNICD expression, doxycycline chow was fed (200 mg/kg, BioServ). Adult iNICD mice were fed doxycycline chow for 3 weeks to transiently activate Notch, followed by a minimum of 16 weeks regular chow to allow for sufficient doxycycline washout and iNICD turnover. In iLOF experiments involving tamoxifen-induced Cre recombination, mice were fed tamoxifen chow for 10 days to allow for Cre recombination, followed by a 4-week washout prior to radiation or sham treatment.

All mice were housed in 12-hour light/dark cycles, at ambient temperatures of 20-22 degrees Celsius, at a humidity range between 40-60%, and with access to food and water ad libitum, in

accordance with animal study guidelines at Washington University. Animal protocols were approved by the Animal Studies Committee at Washington University School of Medicine, and all animals were handled in accordance with the National Institutes of Health (NIH) Guide for the Care and Use of Laboratory Animals.

Murine Cardiac Irradiation (IR) Model Murine IR treatment was performed using the small animal radiation research platform (SARRP, Xstrahl Inc.). The SARRP has an X-ray tube mounted on a gantry, with a motorized stage serving as a couch on which the mouse is placed. These allow for cone-beam computed tomography (CT) imaging (imaging mode) and radiation delivery (therapy mode)[156]. In imaging mode, the SARRP operates at 60–80 kVp and 0.5 mA using 1 mm of aluminum filtration. In therapy mode, the SARRP operates at 175–220 kVp with 0.15 mm of copper filtration. This platform allows for image-guided isocentric radiation of murine hearts and mimics RT therapy in humans.

Mice were first anesthetized using isoflurane, and cone-beam computed tomography (CT) imaging was performed to target the heart. CT images were reconstructed and imported into Muriplan (v.3.0. Xstrahl Inc.), where the isocenter was selected. The heart was then irradiated using anterior-posterior-opposed beams from the 10 mm x 10 mm collimator at a 3.9 Gy/min dose rate. A single-fraction exposure to the entire volume of the mouse heart was delivered at the predetermined dose. For comparisons, all littermate (sham) controls received isoflurane anesthesia and CT imaging, but no isocentric ionizing radiation.

In short-term, nonsurgical murine experiments, one irradiated Notch iLOF mouse spontaneously died at 4 weeks post-IR, while all remaining sham control and IR mice survived to their experimental endpoints. In the aged, long-term murine IR cohort, two sham control mice (each at 35 weeks and 42 weeks after sham treatment) and four IR mice (each at 18 weeks, 19 weeks, 31 weeks, and 41 weeks post-IR) spontaneously died after treatment. On necropsy, there was no evidence of direct cardiac damage or gross structural differences in either treatment group. Of note, 3 of 4 cadaveric IR mice appeared notably cachexic compared to surviving littermates.

Murine MI Model Adult mice were anesthetized with ketamine (100 mg/kg) and xylazine (10 mg/kg) administered intraperitoneally. Under artificial ventilation, a left thoracotomy was performed to expose the left ventricle and LAD artery[130]. The proximal portion of the LAD was ligated with a 9-0 silk suture. After closure of the surgical incision, mice were recovered on a warmer and returned to their cage. The mean time for each surgical procedure was approximately 10 minutes. From 29 mice surviving the initial surgery, eight died before the end of the 2-week postoperative period, and surviving mice were randomly assigned to receive either 25 Gy IR or sham treatment. During the 6-week period following radiation treatment, one sham mouse and zero IR mice died. At the time of optical mapping (8 weeks post-MI, 6 weeks post-IR), hearts from three mice (1 control and 2 IR) were covered in excess surgical adhesions and/or adhered to the anterior thoracic wall. These hearts could not be dissected without causing ventricular wall rupture and were excluded from downstream optical mapping experiments. In both treatment groups, stimulation of myocardium outside the scar region resulted in optical action potentials within the scar region that had <50% upstroke velocity and peak optical voltage when compared to regions

of viable myocardium (**Figure 3.11a**), and thus isochrones below the surgical ligation are masked and omitted.

Murine Electrocardiogram Surface ECGs were performed on mice anesthetized with isoflurane. Lead II ECGs were recorded at a sampling rate of 4 kHz using LabChart (Version 8.0, ADInstruments), and ECG intervals of 100 averaged beats were measured using the LabChart ECG software package[119]. Because the morphology of the QRS complex in mice includes the presence of a J wave that immediately follows the S wave, the end of the QRS interval was strictly defined as the time when the S wave crosses the isoelectric line. During all ECG collection and analysis, investigators were blinded to sample group allocation.

Optical Mapping Murine hearts were explanted, Langendorff-perfused, and optically mapped, as previously described[151,157]. Specifically, hearts were perfused and immersed in an oxygenated Tyrode's solution (128.2 mM NaCl, 4.7 mM KCl, 11.1 mM glucose, 1.19 mM NaH_2PO_4, 20 mM $NaHCO_3$, 1.05 mM $MgCl_2$, 1.3 mM CaCl, pH 7.4) maintained at 37°C. Briefly, the potentiomic dye Di-4-ANEPPS (Life Technologies) and the excitation-contraction uncoupler blebbistatin (Cayman Chemical) were added to the Langendorff perfusate to allow for fluorescent detection of membrane potential changes and to eliminate motion artifacts, respectively. Murine hearts were electrically stimulated at 10 Hz to measure CV or with S1-S2 stimulation protocols of decreasing cycle lengths to determine ERP. A green 524 nm light source was used to excite the voltage sensitive dye. The emitted fluorescence was filtered by a single long-pass 650 nm filter and recorded by CMOS camera (BrainVision LLC). Data was collected through the MiCAM Ultima software (v.2011.11, BrainVision LLC). Data analysis was performed on MATLAB using open

source Rhythm software (Rhythm2014b, http://efimovlab.org/research/resources/rhythm)[157]. With surface coordinate distances and the time of action potential upstroke, defined as maximum voltage derivative $(dV_m/dt)_{max}$ of optical signals, activation maps were generated for calculations of longitudinal and transverse conduction velocities. Velocities were calculated by using isochrone distances and times of action potential upstroke originating from the site of stimulation. All investigators were blinded to the sample group allocation during data collection and analysis.

Histology and Immunohistochemistry Immunohistochemistry was performed on OCT-embedded frozen or paraffin-embedded sections. Gross heart morphology and collagen content were examined using Masson's Trichrome stain (American MasterTech Scientific). Sections were treated with antibodies recognizing γH2AX (R&D Systems AF2288, lot KNH1218111), $Na_V1.5$ (1:100, Alomone Labs, 493-511, lot ASC005AN3002 and ASC005AN3702), Connexin 43 (1:50, Thermo Fisher 71-0700, lot PI209083), N-Cadherin (1:100, Invitrogen 33-3900, lot UC284646), and PCM1 (1:200, MilliporeSigma HPA02337). Secondary fluorescent-conjugated antibodies included Alexa 568 (1:200, Abcam ab175471, lot 1494753) and Alexa 488 (1:200, Abcam ab150077, lot 3244688, and ab150121, lot 3201847). Sections were also treated with wheat germ agglutinin (WGA, Thermo Fisher) to measure cardiomyocyte size and DAPI (Sigma D9542) to identify nuclei. For all digital imaging, investigators were blinded to sample conditions, and, for each immunohistochemical target, all samples were imaged with identical settings on a confocal microscope (Leica Biosystems). Quantification of blinded images was performed using ImageJ (v.2.0.0, NIH).

Hydroxyproline Assay A hydroxyproline assay was performed using a standard 4-hydroxyproline amino acid colorimetric test kit (Sigma). Briefly, 10 mg of flash-frozen tissue was homogenized in water and hydrolyzed at 120°C for 3 hours[126]. After hydrolysis, oxidized hydroxyproline was reacted with 4-(dimethyamino)benzyladehyde to produce a colorimetric product proportional to hydroxyproline concentration. Hydroxyproline content for standard curves and samples was quantified by measuring absorbance at 560 nm using Gen5 software (v.2.0.4, Agilent BioTek) and Excel (v.16.52, Microsoft).

Protein Extraction, Electrophoresis, and Immunoblotting Protein lysates were made from flash frozen mouse or human ventricular samples for immunoblotting[151]. For each biological replicate, approximately 20-30 mg of ventricular tissue was homogenized using a modified RIPA lysis buffer (50 mM Tris-HCl, 150 mM NaCl, 5 mM EDTA, 1% Triton-X, 0.5% Sodium Deoxycholate, 0.1% SDS) treated with a cOmplete Mini EDTA-free protease inhibitor tablet (1 tab/10 mL buffer, Roche). After homogenization, samples were centrifuged for 10 mins at 13200 *g*, and supernatants were aliquoted and stored at -80°C. Protein concentrations were measured using a commercial BCA assay (Thermo Fisher). Gel electrophoresis was performed using pre-cast 4-15% or 4-20% Tris-Glycine gels (BioRad) and pre-cast 10% or 12% NuPage Bis-Tris gels (Invitrogen). After gel electrophoresis, proteins were transferred overnight to PVDF (Millipore Sigma) or nitrocellulose (Invitrogen) membranes. Blots were blocked for 1 hour in milk blocking buffer (5% milk in Tris-buffered saline, 0.05% Tween-20). Immunoblotting was performed using anti-$Na_V1.5$ (1:1000 Alomone Labs, 493-511, lot ASC005AN3002 and ASC005AN3702), anti-Connexin 43 (1:2000 Invitrogen 71-0700, lot PI209083), and anti-GAPDH (1:2000, Cell Signaling Technology 14C10, lot 14) and incubated overnight at 4°C. Secondary detection was performed using

horseradish peroxidase (HRP)-conjugated antibodies (1:5000 Abcam ab6721, lot GR3321356) and Clarity Western ECL Substrate (BioRad). Densitometry analysis was performed using ImageLab software (BioRad) and normalized to GAPDH density. For all immunoblotting experiments, blots were repeated with a minimum of 3 technical triplicates using the same biological samples. For all densitometric quantifications, investigators were blinded to sample conditions.

RNA Isolation Total RNA was isolated from murine ventricles using TRIzol reagent (Invitrogen)[126], per manufacturer instructions, and DNAse-treated using the TURBO DNA-free Kit (Ambion).

RNA Sequencing RNA-seq was performed on murine ventricular tissue from sham control mice (n=6), at 2 weeks post-IR (n=6), and at 6 weeks post-IR (n=6). Total RNA was isolated as described above, and RNA was quantitated and quality-assessed using a 2100 Bioanalyzer (Agilent). RNA-seq was performed by the Genome Technology Access Center at Washington University School of Medicine. Briefly, sequencing libraries were constructed using the Roche KAPA RNA HyperPrep kit per manufacturer's recommendations. Libraries were sequenced with the Illumina NovaSeq S4 (2 x 150 bp) to a median depth of 42.7 million +/- 3.8 million reads.

RNA-Seq Analysis Reads were aligned to the Mus musculus GRCm38.76 genome using STAR (v. 2.7.3a.)[158], and alignment quality metrics were obtained from RNA-SeQC (v. 2.3.5). Transcript abundance was quantified in Salmon (v. 1.0)[159], and downstream analysis was performed in R (v. 3.6.3). Transcript abundance was summarized to gene counts using tximport (v. 3.10). Gene counts were scaled to library size using trimmed mean of M-value (TMM) normalization in EdgeR (v.

3.28)[160]. Genes with a CPM of less than 0.23 (10/median library size) in at least 6 samples were removed. Weighted likelihoods were calculated and differential expression analysis performed in limma (v. 3.42)[161]. Resulting *P*-values were adjusted for multiple comparisons by Benjamini-Hochberg method. Pathway analysis and gene set enrichment analysis were performed in GSEA(v. 4.1.0)[162] for each pairwise comparison using 1000 permutations and otherwise default parameters. Annotated gene sets tested were from the Molecular Signatures Database (MSigDB) using Broad Institute-hosted mouse annotations[163]. RNA-seq analysis performed by Jeff Szymanski in the Department of Radiation Oncology.

RNA in situ Hybridization (ISH) RNA-ISH was performed using the RNAScope Multiplex Fluorescent V2 Assay (Advanced Cell Diagnostics) per manufacturer recommendation. Briefly, formalin-fixed, paraffin-embedded slides were deparaffinized with xylene, washed in 100% ethanol, and incubated with RNAscope Hydrogen Peroxide (Advanced Cell Diagnostics) for 10 min. Target retrieval was performed with RNAscope Target Retrieval Buffer (Advanced Cell Diagnostics) at 100°C for 30 min followed by treatment with RNAScope Protease Plus (Advanced Cell Diagnostics) for 30 min at 37°C. Slides were then hybridized with murine *Scn5a* and *Ryr2* target probes (Advanced Cell Diagnostics) at 40°C for 2h. OPAL fluorophores were added at 1:750 dilution in TSA buffer to visualize targets. Slides were treated with TrueBlack Lipofuscin Autofluorescence Quencher (Biotium), stained with Spectral DAPI (Advanced Cell Diagnostics), and mounted in Vectashield PLUS mounting medium (Vector Labs). For all digital imaging, investigators were blinded to sample conditions, and, for each immunohistochemical target, all samples were imaged with identical settings on a confocal microscope (Leica Biosystems). Quantification of mRNA target foci was performed using ImageJ (v.2.0.0, NIH).

PCM1 Cardiomyocyte Nuclei Isolation Cardiomyocyte nuclei isolation was performed using a modified protocol from previous studies. Forty to 60 mgs of previously snap-frozen or freshly collected murine left ventricle was first diced into 1mm-by-1mm chunks of tissue and washed in PBS. After washing, the excess PBS was discarded and the diced tissue was resuspended in 10 mL homogenization buffer (0.32 M Sucrose, 5 mM $CaCl_2$, 3 mM MgAc, 2 mM EDTA pH8, 0.5 mM EGTA, 10 mM Tris-HCl pH 8, Spermine 0.1 M, and Spermidine trihydrochloride 0.1 M) and supplemented with RNAsin Plus (80 units/mL, ProMega N2615) and protease inhibitor (cOmplete Mini EDTA-free protease inhibitor tablet, 1 tab/10 mL buffer, Roche). The resuspended tissue was then transferred to a 15 mL dounce tissue grinder with glass pestle A (loose pestle, Kimble) and underwent 30 strokes. After 30 strokes, 20 uL IGEPAL CA-630 detergent buffer (Sigma I8896) diluted in 80 uL homogenization buffer was added to the homogenate, followed by 30 additional strokes with pestle A. Following pestle A homogenization, the homogenate underwent dounce homogenization with glass pestle B (tight pestle, Kimble) with an additional minimum of 20 strokes. Progression of nuclei extraction was crudely assessed using trypan blue on a homogenization aliquot. Following homogenization, samples were strained using a 40 um nylon cell strainer (Corning) and centrifuged at 1700g for 8 minutes at 4°C using a swinging bucket rotor. The supernatant was discarded and the nuclei pellet was resuspended in 1 mL supplemented homogenization buffer. Nuclei were then stained using anti-PCM1(1:1000, HPA023370, MilliporeSigma) for 30 minutes on a Nutator shaker at 4°C. After 30 minutes, samples were spun down at 1700 g for 5 minutes, the supernatant was discarded, and the nuclei pellet was resuspended in 1 mL of supplemented homogenization buffer. Samples were then stained with secondary antibody Alexa Fluor 647 (goat anti-rabbit, 1:1000, A21244, Invitrogen), and DAPI (1:45,000,

MilliporeSigma) for 20 minutes on a Nutator at 4°C. Following secondary staining, samples were spun down at 1700g for 5 minutes, the supernatant was discarded, and the nuclei pellet was resuspended in 1 mL of supplemented homogenization buffer. Resuspended stained nuclei were filtered using a 30 uM CellTrics strainer prior to sorting (04-004, 2326 Systmex). Stained nuclei were sorted by FANS using a MoFlo sorter (Beckman Coulter) with a 100 um nozzle at the Siteman Flow Cytometry Core at Washington University to collect DAPI-positive, PCM1-positive populations after size selection and double exclusion. Per-sample single-positive (DAPI-only, or AF647-only) and unstained controls were used for all sample gating. Populations of 2n and 4n nuclei were subsequently quantified using FlowJo softeware (FlowJo LLC).

ATAC-Seq Nuclear DNA was tagmented and ATAC-seq libraries were generated using the OMNI-ATACseq protocol as previously described[164,165]. For all reactions, reagents were obtained from a preassembled ATAC-seq kit (ActiveMotif) using manufacturer recommendations. Briefly, approximately ~100,000 PCM1-positive cardiomyocyte nuclei were sorted into Eppendorf tubes as described above. Following cardiomyocyte nuclei sorting, samples were spun down at 500g for 10 minutes and the supernatant was discarded. Samples were subsequently tagmented in a thermomixer at 37°C, 800 rpm, for 60 minutes. Following the tagmentation reaction, column DNA purification was performed to collect tagmented DNA. Library preparation was performed using Illumina Nextera N7XX and N5XX dual-index primers and PCR amplified with 10 cycles of: 98°C for 10 seconds, 63°C for 30 seconds, followed by 72°C for 1 minute. Following library preparation, double-sided library purification was performed using AMPure XP beads to remove primer dimers and >1,000 bp fragments, according to manufacturer recommendations. Library quality and concentrations were assessed using a High Sensitivity D1000 ScreenTape (Agilent). Samples were

sequenced on a NovaSeq S4 2x150 sequencer at GTAC targeting 50 million reads/library. Following demultiplexing, ATAC-seq peaks were called by MACS2 narrow peak output and consensus peaks were generated by taking the union of peaks of each individual sample. Peak counts were normalized by loess method. Sequencing reads were aligned to the reference genome mm10 using NovoAlign to map out regions of differential accessibility in irradiated cardiomyocytes and compared to sham-irradiated littermate controls. ATAC-seq analyses were tested and performed by Jeff Szymanski.

Statistical Analysis Prism version 8.02 (GraphPad Software Inc.) was used to perform statistical analyses and plot data. Distribution normality was tested using the D'Agostino-Pearson test. Unless otherwise stated, a $P < 0.05$ (95% confidence) was considered statistically significant. For comparisons of two experimental groups, a two-tailed, unpaired Student's *t*-test was used. For comparisons of three or more experimental groups, a repeated-measures one-way analysis of equal variance (ANOVA) with a Tukey post-hoc test of means was used. For statistical comparisons for differences between pre-RT and post-RT QRS intervals in ENCORE-VT patients, a two-tailed Wilcoxon matched-pairs signed-rank test was performed. For all data representation, the *P* value, number of biological replicates, and statistical test used are reported in corresponding figure legend.

Chapter 8: Discussion, Future Directions, and Conclusions

8.1 Discussion

Cardiac RT is an emerging treatment option for patients with refractory VT. The objective of this dissertation was to define the structural, functional, molecular, and epigenetic effects of focused, single-fraction RT in the adult post-mitotic mammalian heart, with an especial focus on cardiomyocyte-specific reprogramming effects. These findings suggest that, rather than achieving an effect of radiation-induced fibrosis, cardiac RT may be used therapeutically to modulate cardiac electrophysiology for VT management in patients.

Through histologic examination and MRI scans of hearts from patients who received cardiac RT, I present evidence from a cohort of human RT patients to show that 25 Gy transmural radiation does not create transmural scar. These findings are consistent with preclinical studies that required doses in excess of 40 Gy to produce fibrotic lesions that interrupted conduction[47,51]. Importantly, emerging preclinical and clinical reports continue to discuss the potential for fibrosis and scar homogenization as preferred biologic effects after RT and often postulate whether 25 Gy treatments result in underdosing to the target. Yet, clinical VT reductions occur within weeks following 25 Gy RT, and radiation-induced fibrosis alone cannot account for the magnitude and timing of these effects. Indeed, these studies further contribute to the growing body evidence to suggest that, for cardiac RT, dose strategies may not necessarily be chosen based on the anticipated effects of late-stage, radiation-induced fibrosis to achieve the desired therapeutic effect.

Previous preclinical studies have reported increases in global levels and lateralization of Cx43 after carbon radiation to the heart[95,101,102], and increased gap junction formation was reported after radiation to other tissue types[88,89]. In these studies, the mechanism of Cx43 upregulation and the functional consequences of lateralization remain unclear. In acute ischemia, lateralization of connexins and diffusion of charge may result in decreased anisotropy and conduction delay and may be therapeutically unfavorable[166]. In this dissertation, using photon-based IR, I also observed IR-associated increases in Cx43 protein; however, I did not observe changes in Cx43 lateralization or conduction anisotropy. Future studies are warranted to determine whether there are differences in $Na_V1.5$ and Cx43 responses, as well as dosing considerations, among different radiation modalities, including X-ray, carbon ion, and proton beam cardiac RT.

Reduced sodium channel expression or availability frequently occur in the setting of heart disease or injury and are major causes of acquired arrhythmias[81,147–149]. Indeed, slowed conduction due to reduced sodium current density is a critical factor in sustaining reentry in regions of fibrosis[82,167]. Previous large animal studies have demonstrated feasibility of gene therapy delivery of skeletal muscle sodium channel SkM1[87,168] and connexins[85] to restore locally suppressed cardiac conduction and subsequently prevent VT recurrence. Here, I observe both acute and persistent increases in electrical propagation within IR-treated hearts, mediated by increases in $Na_V1.5$ and Cx43. Indeed, increases in either sodium channel expression or gap junction coupling are expected to prevent reentrant arrhythmias[82,85,87,167,168] via restoration of cardiac conduction[169,170] (**Figure 1.1**).

Previously, reactivation of developmental signaling pathways, including Notch, was sufficient to epigenetically reprogram cardiomyocytes to produce a conductive "Purkinje-like" conduction phenotype[111,120]. Furthermore, Notch signaling is known to play a role in the radiation response and radio-resistance of several tissue types[106,107]. Through RNA sequencing and transgenic approaches, I identify cardiomyocyte-specific Notch activation as one mechanistic cell signaling contributor to the pro-conductive effect of radiation, via upregulation of the cardiac sodium channel. In this dissertation, I utilized murine model systems to allow for genetic manipulation and testing of direct causality of radiation-induced conduction reprogramming. Specifically, I demonstrate that cardiomyocyte-specific Notch activation using doxycycline-induced overexpression of the NICD in cardiomyocytes is sufficient to persistently increase cardiac conduction and upregulate $Na_V1.5$. Furthermore, through a loss-of-function approach using tamoxifen-induced expression of a dominant-negative mutant of the MAML1 Notch transcriptional co-activator, I demonstrate that Notch is not only sufficient but also necessary to achieve the full effects of radiation-induced conduction reprogramming.

The functional effects of radiation-induced increases to $Na_V1.5$ and Cx43 may act through several electrical mechanisms to prevent conduction block and reentry and explain the antiarrhythmic effect conferred to patients after 25 Gy RT. In the setting of heart disease and conduction heterogeneity, homogenization of conduction through restoration of either membrane excitability or intercellular coupling would reduce the vulnerable window that allows unidirectional block to occur[7]. Additionally, increased intercellular coupling alone may prevent aberrant conduction by increasing the functional sink and reducing the Safety Factor to terminate arrhythmic conduction[170]. However, this phenomenon requires Cx43 upregulation that exceeds the effect size

observed our study. Finally, data from this study suggests that, within surviving cardiomyocytes in the peri-infarct region, upregulation of $Na_V1.5$ and Cx43 results in local increases in conduction velocity to functionally rescue regions of conduction delay necessary for sustained reentry and tachycardia[170]. Future studies are warranted to determine which molecular effects can be best-leveraged in the setting of RT to prevent reentry and tachycardia.

This dissertation presents findings to suggest that an anti-arrhythmic therapy, successfully used in patients with refractory VT, may increase levels of the cardiac sodium channel and improve conduction. Indeed, explanted cardiac specimens obtained from a treated patient with refractory VT revealed 3-fold higher $Na_V1.5$ protein levels in the radiation-targeted region when compared to a nontargeted region of the same heart, restoring $Na_V1.5$ to levels within the range of nonfailing myocardium. As an observation of the potential effect of RT on human physiology, I also report a nonsignificant decrease in mean QRS duration in the ENCORE-VT patient cohort, as well as robustly shortened QRS intervals in at least 4 of the 19 patients.

These findings have direct relevance for patient care. Most surviving patients continue to exhibit reduced VT burden 24 months after a single RT treatment[27]. Our results demonstrate that the functional and molecular effects of RT and Notch reactivation are persistent and expected to directly translate into long-term durability of therapy. A dose of 25 Gy was prescribed in previous clinical studies to minimize cardiotoxic effects of radiation. Although this current dose is proven to be safe and effective[18], there are rare cases of pericardial effusion and a single adverse event of gastropericardial fistula that occurred 2 years after treatment[27]. Here, I show that radiation-induced electrical reprogramming can also occur at lower doses in the range of 15-25 Gy in mice. Indeed,

Notch signaling has been reported to activate in a variety of tissue types following lower doses of radiation[105–107]. These data could warrant future clinical studies of careful downward dose titration to find the lowest effective dose that minimizes risk of late-stage toxicity. Lower dosages may be particularly favorable in instances when the prescribed treatment volume is large, or when the prescribed treatment location is adjacent to nearby radiosensitive organs.

8.2 Limitations and future directions

There are several limitations to the experimental approaches within this dissertation that require additional investigations. Given that each patient is prescribed a target volume and location specific to the individual's scar-related VT, I acknowledge that global electrophysiologic changes reflected by changes to the QRS interval is neither observed nor expected in every patient. Although there were 13 patients with shortened QRS durations after RT, these QRS changes were statistically nonsignificant in the 19-patient cohort, and at least 5 patients exhibited lengthened QRS durations. Overall, these changes in QRS duration cannot be excluded as an unrelated phenomenon in the absence of additional analyses, and a comprehensive analysis of all ECG parameters is outside of the current scope this dissertation. The clinical results presented here are also limited by the trial's single-arm design, low number of patients enrolled, narrow patient selection, and recruitment and treatment conducted at a single academic center, which currently limit generalization of results to other patient populations.

In the preclinical arm, I profiled the cardiac radiation response after whole-heart radiation, while clinically, RT is limited select arrhythmogenic regions. Indeed, future studies are expected to

elucidate relationships among treatment target volume, isodoses, local changes in conduction protein expression, and global changes in ECG intervals. Additionally, I implemented a surgical infarct model of HF, which does not represent the subset of patients with nonischemic cardiomyopathy. Furthermore, while humans and large animals have exhibit HF-associated decreases in conduction proteins, rodent models of heart failure have smaller conduction substrates, exhibit remodeling of repolarizing currents[171], and thus make reentrant tachycardia difficult to demonstrate. Additional studies in larger animal models of VT to demonstrate resolution of VT as the precise antiarrhythmic effect of this radiobiology are still ongoing.

Importantly, there are discrete differences between the ionic currents that make up the action potentials of human and murine cardiomyocytes. While excitatory sodium current I_{Na} is well-conserved among mammals[172], there are several differences in the expression of repolarizing potassium currents across species. For example, the rapidly (I_{Kr}) and slowly (I_{Ks}) activating delayed rectifier potassium channels responsible for repolarization of the human cardiomyocyte action potential do not exist in mice[172]. Although I do not observe effects of IR on ERP, this dissertation does not rule out an effect of radiation on human cardiomyocyte repolarization. Further studies in large animal models that express human repolarization currents are expected to clarify the role of RT effects on cardiac repolarization.

While this dissertation highlights cardiomyocyte Notch signaling as a mechanism by which $Na_V1.5$ may upregulate after radiation, the mechanisms of post-RT reprogramming are likely multifactorial, and future studies are necessary to further define the cellular mechanisms underlying these effects are warranted. Furthermore, on bulk RNA-sequencing, I identify several

proinflammatory pathways at 6w post-IR that were not explored in the scope of this dissertation. Importantly, recent evidence suggests that tissue-resident immune cells in the setting heart disease may have direct electrophysiologic and structural consequences. Future studies using single-cell or single-nucleus RNA-seq approaches are warranted to profile the effects of 25 Gy on changes within the cell populations and composition of the cardiac tissue after IR, and preliminary data in the Rentschler lab suggests broad changes within the non-cardiomyocyte and immune populations within the heart within 6w post-IR (data not shown).

This dissertation presents evidence to suggest that cardiomyocyte nuclear structure and chromatin accessibility are highly sensitive to DNA damage and repair. At 48 hours, I observed significant global chromatin compaction within cardiomyocyte nuclei by an ATAC-seq approach. Furthermore, there was an observed increase in cardiomyocyte nuclear size that did not correlate with nuclear ploidy and DNA content. Importantly, the presence of chronic inflammation at 6w post-IR limited interpretation of FANS-based isolation of PCM1-positive nuclei ATAC-seq data at these long-term timepoints. Thus, this dissertation leaves the question of whether radiation damage induces long-term chromatin "scars" within cardiomyocytes unanswered.

Interestingly, changes in 3D genome structure and segregation of topologically associated domains was recently reported in cultured fibroblasts and lymphoblasts for at least 5 days after 5 Gy radiation[173]. To further investigate effects of 25 Gy RT on cardiomyocyte epigenetics, an *in vitro* approach using post-mitotic human induced pluripotent-derived stem cell cardiomyocytes (hiPSC-CMs) is likely required. Although hiPSC-CMs are not fully matured compared to adult cardiomyocytes *in vivo*, these cells adequately express $Na_V1.5$ and Cx43, are able to exhibit

electrical conduction properties, and are post-mitotic and thus radioresistant. Indeed, as a follow-up to the findings presented in this dissertation[174], a recent report replicated my described increases to cardiomyocyte CV after 20-25 Gy IR in commercially-available hiPSC-CMs using a microelectrode array-based approach[175]. Preliminary data in the Rentschler lab suggests that these hiPSC-CMs also upregulate $Na_V1.5$ and Cx43 within 2 weeks post-IR (data not shown). Thus, this model system is likely appropriate for *in vitro* investigations of radiation-induced electrical reprogramming. The use of these hiPSC-CMs may be especially suitable for profiling long-term, cardiomyocyte-specific transcriptional and epigenetic effects of single-fraction, high-dose radiation. Indeed, sequencing-based (RNA-seq, ATAC-seq, CUT&RUN, and Hi-C/3C) approaches on hiPSC-CMs are expected to identify additional signaling pathways and transcriptional mediators of interest. For example, under immense oxidative stress, the interaction of ROS with guanine bases produces 8-oxoguanine with potential epigenetic consequences. Complete profiling of structural and substructural epigenetic changes after single-fraction RT within cardiomyocytes is warranted for additional mechanistic insights. Furthermore, experiments using this model system are expected to elucidate cardiomyocyte autonomous versus noncardiomyocyte contributors to the reprogramming effects described in this dissertation.

8.3 Concluding remarks

Over the past 5 years, cardiac RT has emerged as a safe and promising treatment approach for management of drug- and CA-refractory VT in patients. While the therapeutic benefit of 25 Gy cardiac RT assumed to occur via its pro-fibrotic effects, described in cancer biology for a variety of actively dividing cell types, the radiation response of adult, post-mitotic cardiomyocytes was not previously described. This dissertation supports a model whereby a single-fraction dose of 25

Gy radiation persistently restores or enhances electrical propagation in diseased hearts without causing transmural fibrosis and scar. Mechanistic insights such as these are expected to lead to refinements in the cardiac radiation clinical protocol and ultimately greater adoption of cardiac RT. Indeed, the ability to noninvasively and functionally eliminate VT circuits, by modulating cardiac electrophysiology in a localized way and without tissue destruction, may allow for safer treatments and prevention of arrhythmias for individuals with myocardial scarring.

Chapter 9: References

1. Natale, A. *et al.* Venice chart international consensus document on ventricular tachycardia/ventricular fibrillation ablation: Special article. *Journal of Cardiovascular Electrophysiology* vol. 21 339–379 (2010).

2. Al-Khatib, S. M. *et al.* 2017 AHA/ACC/HRS Guideline for Management of Patients With Ventricular Arrhythmias and the Prevention of Sudden Cardiac Death. *Circulation* **138**, e272–e391 (2018).

3. de Bakker, J. M. T. *et al.* Macroreentry in the infarcted human heart: The mechanism of ventricular tachycardias with a 'focal' activation pattern. *J. Am. Coll. Cardiol.* **18**, 1005–1014 (1991).

4. Antzelevitch, C. & Burashnikov, A. Overview of Basic Mechanisms of Cardiac Arrhythmia. *Cardiac Electrophysiology Clinics* vol. 3 23–45 (2011).

5. Holmes, J. W., Laksman, Z. & Gepstein, L. Making better scar: Emerging approaches for modifying mechanical and electrical properties following infarction and ablation. *Prog. Biophys. Mol. Biol.* **120**, 134–148 (2016).

6. Quan, W. & Rudy, Y. Unidirectional block and reentry of cardiac excitation: A model study. *Circ. Res.* **66**, 367–382 (1990).

7. SHAW, R. M. & RUDY, Y. The Vulnerable Window for Unidirectional Block in Cardiac Tissue: Characterization and Dependence on Membrane Excitability and Intercellular Coupling. *J. Cardiovasc. Electrophysiol.* **6**, 115–131 (1995).

8. Zhang, D. M. *et al.* Leveraging Radiobiology for Arrhythmia Management: A New Treatment Paradigm? *Clin. Oncol.* **33**, 723–734 (2021).**

9. Sapp, J. L. *et al.* Ventricular Tachycardia Ablation versus Escalation of Antiarrhythmic Drugs. *N. Engl. J. Med.* **375**, 111–121 (2016).

10. Connolly, S. J. *et al.* Comparison of β-blockers, amiodarone plus β-blockers, or sotalol for prevention of shocks from implantable cardioverter defibrillators - The OPTIC study: A randomized trial. *J. Am. Med. Assoc.* **295**, 165–171 (2006).

11. Priori, S. G. *et al.* 2015 ESC Guidelines for the management of patients with ventricular arrhythmias and the prevention of sudden cardiac death: The Task Force for the Management of Patients with Ventricular Arrhythmias and the Prevention of Sudden Cardiac Death of the Europe. *Eur. Heart J.* **36**, 2793-2867l (2015).

12. Kumar, S. *et al.* Multicenter Experience with Catheter Ablation for Ventricular Tachycardia in Lamin A/C Cardiomyopathy. *Circ. Arrhythmia Electrophysiol.* **9**, (2016).

13. Dinov, B. *et al.* Outcomes in catheter ablation of ventricular tachycardia in dilated nonischemic cardiomyopathy compared with ischemic cardiomyopathy: Results from the prospective heart centre of leipzig vt. *Circulation* **129**, 728–736 (2014).

14. Tokuda, M. *et al.* Acute failure of catheter ablation for ventricular tachycardia due to structural heart disease: Causes and significance. *J. Am. Heart Assoc.* **2**, e000072 (2013).

15. Eriksson, D. & Stigbrand, T. Radiation-induced cell death mechanisms. *Tumor Biology* vol. 31 363–372 (2010).

16. Kim, W. *et al.* Cellular Stress Responses in Radiotherapy. *Cells* vol. 8 (2019).

17. Cuculich, P. S. *et al.* Noninvasive Cardiac Radiation for Ablation of Ventricular Tachycardia. *N. Engl. J. Med.* **377**, 2325–2336 (2017).

18. Robinson, C. G. *et al.* Phase I/II Trial of Electrophysiology-Guided Noninvasive Cardiac Radioablation for Ventricular Tachycardia. *Circulation* **139**, 313–321 (2019).

19. Neuwirth, R. *et al.* Stereotactic radiosurgery for ablation of ventricular tachycardia. *Europace* **21**, 1088–1095 (2019).

20. Cvek, J. *et al.* Cardiac Radiosurgery for Malignant Ventricular Tachycardia. *Cureus* (2014) doi:10.7759/cureus.190.

21. Loo, B. W. *et al.* Stereotactic Ablative Radiotherapy for the Treatment of Refractory Cardiac Ventricular Arrhythmia. *Circ. Arrhythmia Electrophysiol.* **8**, 748–750 (2015).

22. Lloyd, M. S. *et al.* Clinical experience of stereotactic body radiation for refractory ventricular tachycardia in advanced heart failure patients. *Hear. Rhythm* **17**, 415–422 (2020).

23. Martí-Almor, J. *et al.* Noninvasive ablation of ventricular tachycardia with stereotactic radiotherapy in a patient with arrhythmogenic right ventricular cardiomyopathy. *Rev. Española Cardiol. (English Ed.* **73**, 97–99 (2020).

24. Jumeau, R. *et al.* Rescue procedure for an electrical storm using robotic non-invasive cardiac radio-ablation. *Radiother. Oncol.* **128**, 189–191 (2018).

25. Haskova, J. *et al.* Stereotactic radiosurgery as a treatment for recurrent ventricular tachycardia associated with cardiac fibroma. *Hear. Case Reports* **5**, 44–47 (2019).

26. Zeng, L. J. *et al.* Stereotactic body radiation therapy for refractory ventricular tachycardia secondary to cardiac lipoma: A case report. *PACE - Pacing Clin. Electrophysiol.* **42**, 1276–1279 (2019).

27. Robinson, C. G. *et al.* Longer Term Results from a Phase I/II Study of EP-guided

Noninvasive Cardiac Radioablation for Treatment of Ventricular Tachycardia (ENCORE-VT). *Int. J. Radiat. Oncol.* **105**, 682 (2019).

28. Gianni, C. *et al.* Stereotactic arrhythmia radioablation for refractory scar-related ventricular tachycardia. *Hear. Rhythm* **17**, 1241–1248 (2020).

29. Lewis, G. D. & Farach, A. Cardiovascular Toxicities of Radiation Therapy. *Methodist DeBakey cardiovascular journal* vol. 15 274–281 (2019).

30. Kiani, S., Kutob, L., Schneider, F., Higgins, K. A. & Lloyd, M. S. Histopathologic and Ultrastructural Findings in Human Myocardium after Stereotactic Body Radiation Therapy for Recalcitrant Ventricular Tachycardia. *Circ. Arrhythmia Electrophysiol.* 1303–1310 (2020) doi:10.1161/circep.120.008753.

31. Salata, C. *et al.* Apoptosis induction of cardiomyocytes and subsequent fibrosis after irradiation and neoadjuvant chemotherapy. *Int. J. Radiat. Biol.* **90**, 284–290 (2014).

32. Somosy, Z. Radiation response of cell organelles. *Micron* vol. 31 165–181 (2000).

33. Yarnold, J. & Vozenin Brotons, M. C. Pathogenetic mechanisms in radiation fibrosis. *Radiotherapy and Oncology* vol. 97 149–161 (2010).

34. Sharma, U. C. *et al.* A Small Peptide Ac-SDKP Inhibits Radiation-Induced Cardiomyopathy. *Circ. Heart Fail.* **11**, e004867 (2018).

35. Shrishrimal, S., Kosmacek, E. A. & Oberley-Deegan, R. E. Reactive oxygen species drive epigenetic changes in radiation-induced fibrosis. *Oxid. Med. Cell. Longev.* **2019**, (2019).

36. Ng, W. K. Radiation-associated changes in tissues and tumours. in *Current Diagnostic Pathology* vol. 9 124–136 (Churchill Livingstone, 2003).

37. Cilliers, G. D., Harper, I. S. & Lochner, A. Radiation-induced changes in the ultrastructure and mechanical function of the rat heart. *Radiother. Oncol.* **16**, 311–326 (1989).

38. Maguire, P. J. *et al.* Cardiac Radiosurgery (CyberHeart^{TM}) for Treatment of Arrhythmia: Physiologic and Histopathologic Correlation in the Porcine Model. *Cureus* (2012) doi:10.7759/cureus.32.

39. Lehmann, B. D. *et al.* A dominant role for p53-dependent cellular senescence in radiosensitization of human prostate cancer cells. *Cell Cycle* **6**, 595–605 (2007).

40. Gewirtz, D. A., Holt, S. E. & Elmore, L. W. Accelerated senescence: An emerging role in tumor cell response to chemotherapy and radiation. *Biochemical Pharmacology* vol. 76 947–957 (2008).

41. Radford, I. R., Murphy, T. K., Radley, J. M. & Ellis, S. L. Radiation response of mouse

lymphoid and myeloid cell lines. Part II. Apoptotic death is shown by all lines examined. *Int. J. Radiat. Biol.* **65**, 217–227 (1994).

42. Verheij, M. & Bartelink, H. Radiation-induced apoptosis. *Cell and Tissue Research* vol. 301 133–142 (2000).

43. Veinot, J. P. & Edwards, W. D. Pathology of radiation-induced heart disease: A surgical and autopsy study of 27 cases. *Hum. Pathol.* **27**, 766–773 (1996).

44. Lehmann, H. I. *et al.* Feasibility Study on Cardiac Arrhythmia Ablation Using High-Energy Heavy Ion Beams. *Sci. Rep.* **6**, (2016).

45. Lehmann, H. I. *et al.* External Arrhythmia Ablation Using Photon Beams. *Circ. Arrhythmia Electrophysiol.* **10**, (2017).

46. Rapp, F. *et al.* Biological Cardiac Tissue Effects of High-Energy Heavy Ions – Investigation for Myocardial Ablation. *Sci. Rep.* **9**, (2019).

47. Suzuki, A. *et al.* Catheter-free arrhythmia ablation using scanned proton beams: Electrophysiologic outcomes, biophysics, and characterization of lesion formation in a porcine model. *Circ. Arrhythmia Electrophysiol.* **13**, 1145–1156 (2020).

48. Chang, J. H. *et al.* Feasibility study on stereotactic radiotherapy for total pulmonary vein isolation in a canine model. *Sci. Rep.* **11**, 1–9 (2021).

49. Blanck, O. *et al.* Dose-escalation study for cardiac radiosurgery in a porcine model. *Int. J. Radiat. Oncol. Biol. Phys.* **89**, 590–598 (2014).

50. Bode, F. *et al.* Pulmonary vein isolation by radiosurgery: Implications for non-invasive treatment of atrial fibrillation. *Europace* **17**, 1868–1874 (2015).

51. Hohmann, S. *et al.* Left ventricular function after noninvasive cardiac ablation using proton beam therapy in a porcine model. *Hear. Rhythm* **16**, 1710–1719 (2019).

52. Scholz, E. P. *et al.* Risen from the dead: Cardiac stereotactic ablative radiotherapy as last rescue in a patient with refractory ventricular fibrillation storm. *Hear. Case Reports* **5**, 329–332 (2019).

53. Taunk, N. K., Haffty, B. G., Kostis, J. B. & Goyal, S. Radiation-induced heart disease: Pathologic abnormalities and putative mechanisms. *Frontiers in Oncology* vol. 5 (2015).

54. Tapio, S. Pathology and biology of radiation-induced cardiac disease. *J. Radiat. Res.* **57**, 439–448 (2016).

55. Boerma, M. *et al.* Effects of ionizing radiation on the heart. *Mutat. Res. - Rev. Mutat. Res.* **770**, 319–327 (2016).

56. Dogan, S. M. *et al.* The effect of radiotherapy on cardiac function. *Coron. Artery Dis.* **23**, 146–154 (2012).

57. Chang, H.-M., Moudgil, R., Scarabelli, T., Okwuosa, T. M. & Yeh, E. T. H. Cardiovascular Complications of Cancer Therapy. *Journal of the American College of Cardiology* vol. 70 2536–2551 (2017).

58. Cheng, Y. J. *et al.* Long-term cardiovascular risk after radiotherapy in women with breast cancer. *J. Am. Heart Assoc.* **6**, (2017).

59. Abe, O. *et al.* Effects of radiotherapy and of differences in the extent of surgery for early breast cancer on local recurrence and 15-year survival: An overview of the randomised trials. *Lancet* **366**, 2087–2106 (2005).

60. Hooning, M. J. *et al.* Long-term risk of cardiovascular disease in 10-year survivors of breast cancer. *J. Natl. Cancer Inst.* **99**, 365–375 (2007).

61. Carr, Z. A. *et al.* Coronary heart disease after radiotherapy for peptic ulcer disease. *Int. J. Radiat. Oncol. Biol. Phys.* **61**, 842–850 (2005).

62. Boerma, M. *et al.* Increased Deposition of von Willebrand Factor in the Rat Heart after Local Ionizing Irradiation. *Strahlentherapie und Onkol.* **180**, 109–116 (2004).

63. De Groot, P. G., Ottenhof-Rovers, M., Van Mourik, J. A. & Sixma, J. J. Evidence that the primary binding site of von Willebrand factor that mediates platelet adhesion on subendothelium is not collagen. *J. Clin. Invest.* **82**, 65–73 (1988).

64. Boerma, M., Bart, C. I. & Wondergem, J. Effects of ionizing radiation on gene expression in cultured rat heart cells. *Int. J. Radiat. Biol.* **78**, 219–225 (2002).

65. Autsavapromporn, N., De Toledo, S. M., Jay-Gerin, J. P., Harris, A. L. & Azzam, E. I. Human cell responses to ionizing radiation are differentially affected by the expressed connexins. *J. Radiat. Res.* **54**, 251–259 (2013).

66. Cha, M. J. *et al.* Early changes in rat heart after high-dose irradiation: Implications for antiarrhythmic effects of cardiac radioablation. *J. Am. Heart Assoc.* **10**, 19072 (2021).

67. Lehmann, H. I. *et al.* Atrioventricular node ablation in langendorff-perfused porcine hearts using carbon ion particle therapy. *Circ. Arrhythmia Electrophysiol.* **8**, 429–438 (2015).

68. Prall, M. *et al.* Treatment of arrhythmias by external charged particle beams: A Langendorff feasibility study. *Biomed. Tech.* **60**, 147–156 (2015).

69. Zhou, X. *et al.* Effects of X-irradiation on mitochondrial DNA damage and its supercoiling formation change. *Mitochondrion* **11**, 886–892 (2011).

70. Yamamori, T. *et al.* Ionizing radiation induces mitochondrial reactive oxygen species production accompanied by upregulation of mitochondrial electron transport chain function and mitochondrial content under control of the cell cycle checkpoint. *Free Radic. Biol. Med.* **53**, 260–270 (2012).

71. Adachi, K. *et al.* Identification of SCN3B as a novel p53-inducible proapoptotic gene. *Oncogene* **23**, 7791–7798 (2004).

72. Görlach, A., Bertram, K., Hudecova, S. & Krizanova, O. Calcium and ROS: A mutual interplay. *Redox Biol.* **6**, 260–271 (2015).

73. Fajardo, L. F., Stewart, J. R. & Cohn, K. E. Morphology of radiation-induced heart disease. *Arch. Pathol.* **86**, 512–519 (1968).

74. Sridharan, V. *et al.* Radiation-induced alterations in mitochondria of the rat heart. *Radiat. Res.* **181**, 324–334 (2014).

75. Takami, M. *et al.* Electrophysiological and pathological impact of medium-dose external carbon ion and proton beam radiation on the left ventricle in an animal model. *J. Am. Heart Assoc.* **10**, (2021).

76. Refaat, M. M. *et al.* Swine atrioventricular node ablation using stereotactic radiosurgery: Methods and in vivo feasibility investigation for catheter-free ablation of cardiac arrhythmias. *J. Am. Heart Assoc.* **6**, (2017).

77. Zei, P. C., Wong, D., Gardner, E., Fogarty, T. & Maguire, P. Safety and efficacy of stereotactic radioablation targeting pulmonary vein tissues in an experimental model. *Hear. Rhythm* **15**, 1420–1427 (2018).

78. Sharma, A. *et al.* Noninvasive stereotactic radiosurgery (CyberHeart) for creation of ablation lesions in the atrium. *Hear. Rhythm* **7**, 802–810 (2010).

79. Jongsma, H. J. & Wilders, R. Gap junctions in cardiovascular disease. *Circulation Research* vol. 86 1193–1197 (2000).

80. Severs, N. J., Bruce, A. F., Dupont, E. & Rothery, S. Remodelling of gap junctions and connexin expression in diseased myocardium. *Cardiovascular Research* vol. 80 9–19 (2008).

81. Zicha, S., Maltsev, V. A., Nattel, S., Sabbah, H. N. & Undrovinas, A. I. Post-transcriptional alterations in the expression of cardiac Na + channel subunits in chronic heart failure. *J. Mol. Cell. Cardiol.* **37**, 91–100 (2004).

82. Campos, F. O. *et al.* Factors Promoting Conduction Slowing as Substrates for Block and Reentry in Infarcted Hearts. *Biophys. J.* **117**, 2361–2374 (2019).

83. Anyukhovsky, E. P. *et al.* Expression of skeletal muscle sodium channel (Nav1.4) or connexin32 prevents reperfusion arrhythmias in murine heart. *Cardiovasc. Res.* **89**, 41–50 (2011).

84. Roell, W. *et al.* Engraftment of connexin 43-expressing cells prevents post-infarct arrhythmia. *Nature* **450**, 819–824 (2007).

85. Greener, I. D. *et al.* Connexin43 gene transfer reduces ventricular tachycardia susceptibility after myocardial infarction. *J. Am. Coll. Cardiol.* **60**, 1103–1110 (2012).

86. Lau, D. H. *et al.* Epicardial border zone overexpression of skeletal muscle sodium channel SkM1 normalizes activation, preserves conduction, and suppresses ventricular arrhythmia an in silico, in vivo, in vitro study. *Circulation* **119**, 19–27 (2009).

87. Boink, G. J. J. *et al.* SkM1 and Cx32 improve conduction in canine myocardial infarcts yet only SkM1 is antiarrhythmic. *Cardiovasc. Res.* **94**, 450–459 (2012).

88. Liu, K. *et al.* Connexin 43 expression in normal and irradiated mouse skin. *Radiat. Res.* **147**, 437–441 (1997).

89. Kasper, M. *et al.* Upregulation of gap junction protein connexin43 in alveolar epithelial cells of rats with radiation-induced pulmonary fibrosis. *Histochem. Cell Biol.* **106**, 419–424 (1996).

90. Ghosh, S., Kumar, A., Tripathi, R. P. & Chandna, S. Connexin-43 regulates p38-mediated cell migration and invasion induced selectively in tumour cells by low doses of γ-radiation in an ERK-1/2-independent manner. *Carcinogenesis* **35**, 383–395 (2014).

91. Glover, D., Little, J. B., Lavin, M. F. & Gueven, N. Low dose ionizing radiation-induced activation of connexin 43 expression. *Int. J. Radiat. Biol.* **79**, 955–964 (2003).

92. Viczenczova, C. *et al.* Irradiation-induced cardiac connexin-43 and miR-21 responses are hampered by treatment with atorvastatin and aspirin. *Int. J. Mol. Sci.* **19**, (2018).

93. Viczenczova, C. *et al.* Myocardial connexin-43 and PKC signalling are involved in adaptation of the heart to irradiation-induced injury: Implication of miR-1 and miR-21. *Gen. Physiol. Biophys.* **35**, 215–222 (2016).

94. Goodenough, D. A. & Paul, D. L. Gap junctions. *Cold Spring Harbor perspectives in biology* vol. 1 (2009).

95. Amino, M. *et al.* Heavy ion radiation up-regulates Cx43 and ameliorates arrhythmogenic substrates in hearts after myocardial infarction. *Cardiovasc. Res.* **72**, 412–421 (2006).

96. Azzam, E. I., De Toledo, S. M. & Little, J. B. Expression of CONNEXIN43 Is Highly

Sensitive to Ionizing Radiation and Other Environmental Stresses. *Cancer Res.* **63**, 7128–7135 (2003).

97. Azzam, E. I., De Toledo, S. M., Spitz, D. R. & Little, J. B. Oxidative metabolism modulates signal transduction and micronucleus formation in bystander cells from α-particle-irradiated normal human fibroblast cultures. *Cancer Res.* **62**, 5436–5442 (2002).

98. De Toledo, S. M., Buonanno, M., Harris, A. L. & Azzam, E. I. Genomic instability induced in distant progeny of bystander cells depends on the connexins expressed in the irradiated cells. *Int. J. Radiat. Biol.* **93**, 1182–1194 (2017).

99. Decrock, E. *et al.* Calcium, oxidative stress and connexin channels, a harmonious orchestra directing the response to radiotherapy treatment? *Biochim. Biophys. Acta - Mol. Cell Res.* **1864**, 1099–1120 (2017).

100. Zhao, Y., De Toledo, S. M., Hu, G., Hei, T. K. & Azzam, E. I. Connexins and cyclooxygenase-2 crosstalk in the expression of radiation-induced bystander effects. *Br. J. Cancer* **111**, 125–131 (2014).

101. Amino, M. *et al.* Year-long upregulation of connexin43 in rabbit hearts by heavy ion irradiation. *Am. J. Physiol. - Hear. Circ. Physiol.* **298**, H1014–H1021 (2010).

102. Amino, M. *et al.* Inducibility of Ventricular Arrhythmia 1 Year Following Treatment with Heavy Ion Irradiation in Dogs with Myocardial Infarction. *PACE - Pacing Clin. Electrophysiol.* **40**, 379–390 (2017).

103. Dadey, D. Y. A. *et al.* The ATF6 pathway of the ER stress response contributes to enhanced viability in glioblastoma. *Oncotarget* **7**, 2080–2092 (2016).

104. Kang, J. H. *et al.* Rhamnetin and cirsiliol induce radiosensitization and inhibition of epithelial-mesenchymal transition (EMT) by miR-34a-mediated suppression of Notch-1 expression in non-small cell lung cancer cell lines. *J. Biol. Chem.* **288**, 27343–27357 (2013).

105. Coleman, M. A. *et al.* Low-dose radiation affects cardiac physiology: Gene networks and molecular signaling in cardiomyocytes. *Am. J. Physiol. - Hear. Circ. Physiol.* **309**, H1947–H1963 (2015).

106. Lagadec, C. *et al.* Radiation-induced notch signaling in breast cancer stem cells. *Int. J. Radiat. Oncol. Biol. Phys.* **87**, 609–618 (2013).

107. Banerjee, D. *et al.* High-Dose Radiation Increases Notch1 in Tumor Vasculature. *Int. J. Radiat. Oncol. Biol. Phys.* **106**, 857–866 (2020).

108. Phillips, T. M., McBride, W. H. & Pajonk, F. The response of CD24-/low/CD44+ breast cancer-initiating cells to radiation. *J. Natl. Cancer Inst.* **98**, 1777–1785 (2006).

109. Bray, S. J. Notch signalling in context. *Nat. Rev. Mol. Cell Biol.* **17**, 722–735 (2016).

110. Tu, L. L. *et al.* Notch signaling is an important regulator of type 2 immunity. *J. Exp. Med.* **202**, 1037–1042 (2005).

111. Khandekar, A. *et al.* Notch-Mediated Epigenetic Regulation of Voltage-Gated Potassium Currents. *Circ. Res.* **119**, 1324–1338 (2016).

112. Lipovsky, C. E. *et al.* Chamber-specific transcriptional responses in atrial fibrillation. *JCI Insight* **5**, (2020).

113. Grego-Bessa, J. *et al.* Notch Signaling Is Essential for Ventricular Chamber Development. *Dev. Cell* **12**, 415–429 (2007).

114. Rones, M. S., McLaughlin, K. A., Raffin, M. & Mercola, M. Serrate and Notch specify cell fates in the heart field by suppressing cardiomyogenesis. *Development* **127**, 3865–3876 (2000).

115. Eldadah, Z. A. *et al.* Familial Tetralogy of Fallot caused by mutation in the jagged1 gene. *Hum. Mol. Genet.* **10**, 163–169 (2001).

116. McCright, B., Lozier, J. & Gridley, T. A mouse model of Alagille syndrome: Notch2 as a genetic modifier of Jag1 haploinsufficiency. *Development* **129**, 1075–1082 (2002).

117. Xue, Y. *et al.* Embryonic lethality and vascular defects in mice lacking the Notch ligand Jagged1. *Hum. Mol. Genet.* **8**, 723–730 (1999).

118. Oka, C. *et al.* Disruption of the mouse RBP-Jκ gene results in early embryonic death. *Development* **121**, 3291–3301 (1995).

119. Rentschler, S. *et al.* Notch signaling regulates murine atrioventricular conduction and the formation of accessory pathways. *J. Clin. Invest.* **121**, 525–533 (2011).

120. Rentschler, S. *et al.* Myocardial notch signaling reprograms cardiomyocytes to a conduction-like phenotype. *Circulation* **126**, 1058–1066 (2012).

121. Gude, N. A. *et al.* Activation of Notch-mediated protective signaling in the myocardium. *Circ. Res.* **102**, 1025–1035 (2008).

122. Kratsios, P. *et al.* Distinct roles for cell-autonomous notch signaling in cardiomyocytes of the embryonic and adult heart. *Circ. Res.* **106**, 559–572 (2010).

123. Croquelois, A. *et al.* Control of the adaptive response of the heart to stress via the Notchl receptor pathway. *J. Exp. Med.* **205**, 3173–3185 (2008).

124. Raya, A. *et al.* Activation of Notch signaling pathway precedes heart regeneration in

zebrafish. *Proc. Natl. Acad. Sci. U. S. A.* **100**, 11889–11895 (2003).

125. Zhao, L. *et al.* Notch signaling regulates cardiomyocyte proliferation during zebrafish heart regeneration. *Proc. Natl. Acad. Sci. U. S. A.* **111**, 1403–1408 (2014).

126. Qiao, Y. *et al.* Transient notch activation induces long-term gene expression changes leading to sick sinus syndrome in mice. *Circ. Res.* **121**, 549–563 (2017).

127. Pannunzio, N. R., Watanabe, G. & Lieber, M. R. Nonhomologous DNA end-joining for repair of DNA double-strand breaks. *Journal of Biological Chemistry* vol. 293 10512–10523 (2018).

128. Kuo, L. J. & Yang, L. X. γ-H2AX- A novel biomaker for DNA double-strand breaks. *In Vivo* vol. 22 305–310 (2008).

129. Olive, P. L. & Banáth, J. P. Phosphorylation of histone H2AX as a measure of radiosensitivity. in *International Journal of Radiation Oncology Biology Physics* vol. 58 331–335 (Elsevier Inc., 2004).

130. Weinheimer, C. J. *et al.* Load-Dependent Changes in Left Ventricular Structure and Function in a Pathophysiologically Relevant Murine Model of Reversible Heart Failure. *Circ. Heart Fail.* **11**, e004351 (2018).

131. Nguyen, T. P., Qu, Z. & Weiss, J. N. Cardiac fibrosis and arrhythmogenesis: The road to repair is paved with perils. *J. Mol. Cell. Cardiol.* **70**, 83–91 (2014).

132. Huang, R. X. & Zhou, P. K. DNA damage response signaling pathways and targets for radiotherapy sensitization in cancer. *Signal Transduct. Target. Ther.* **5**, 1–27 (2020).

133. Milan, D. J., Giokas, A. C., Serluca, F. C., Peterson, R. T. & MacRae, C. A. Notch1b and neuregulin are required for specification of central cardiac conduction tissue. *Development* **133**, 1125–1132 (2006).

134. Koitabashi, N. *et al.* Avoidance of transient cardiomyopathy in Cardiomyocyte-targeted Tamoxifen-induced mercremer gene deletion models. *Circ. Res.* **105**, 12–15 (2009).

135. Li, F., Wang, X., Capasso, J. M. & Gerdes, A. M. Rapid transition of cardiac myocytes from hyperplasia to hypertrophy during postnatal development. *J. Mol. Cell. Cardiol.* **28**, 1737–1746 (1996).

136. Porrello, E. R. *et al.* Transient regenerative potential of the neonatal mouse heart. *Science (80-.).* **331**, 1078–1080 (2011).

137. Herget, G. W., Neuburger, M., Plagwitz, R. & Adler, C. P. DNA content, ploidy level and number of nuclei in the human heart after myocardial infarction. *Cardiovasc. Res.* **36**, 45–51 (1997).

138. González-Rosa, J. M. *et al.* Myocardial Polyploidization Creates a Barrier to Heart Regeneration in Zebrafish. *Dev. Cell* **44**, 433-446.e7 (2018).

139. Kellokumpu-Lehtinen, P., Söderström, K. O., Kortekangas, A. & Nordman, E. Radiation-induced morphological changes and radiocurability in squamous cell carcinoma of the head and neck region: A preliminary report. *Acta Oncol. (Madr).* **29**, 517–520 (1990).

140. Magi-Galluzzi, C., Sanderson, H. & Epstein, J. I. Atypia in nonneoplastic prostate glands after radiotherapy for prostate cancer: Duration of atypia and relation to type of radiotherapy. *Am. J. Surg. Pathol.* **27**, 206–212 (2003).

141. Richardson, G. D. Simultaneous assessment of cardiomyocyte DNA synthesis and ploidy: A method to assist quantification of cardiomyocyte regeneration and turnover. *J. Vis. Exp.* **2016**, 53979 (2016).

142. Bhattacharyya, S., Sathe, A. A., Bhakta, M., Xing, C. & Munshi, N. V. PAN-INTACT enables direct isolation of lineage-specific nuclei from fibrous tissues. *PLoS One* **14**, e0214677 (2019).

143. Bergmann, O. *et al.* Identification of cardiomyocyte nuclei and assessment of ploidy for the analysis of cell turnover. *Exp. Cell Res.* **317**, 188–194 (2011).

144. Burgess, R. C., Burman, B., Kruhlak, M. J. & Misteli, T. Activation of DNA Damage Response Signaling by Condensed Chromatin. *Cell Rep.* **9**, 1703–1717 (2014).

145. Schick, S. *et al.* Dynamics of chromatin accessibility and epigenetic state in response to UV damage. *J. Cell Sci.* **128**, 4380–4394 (2015).

146. Cui, M. & Olson, E. N. Protocol for Single-Nucleus Transcriptomics of Diploid and Tetraploid Cardiomyocytes in Murine Hearts. *STAR Protoc.* **1**, 100049 (2020).

147. Luo, L. *et al.* Calcium-dependent Nedd4-2 upregulation mediates degradation of the cardiac sodium channel Nav1.5: implications for heart failure. *Acta Physiol.* **221**, 44–58 (2017).

148. Van Der Zwaag, P. A. *et al.* Phospholamban R14del mutation in patients diagnosed with dilated cardiomyopathy or arrhythmogenic right ventricular cardiomyopathy: Evidence supporting the concept of arrhythmogenic cardiomyopathy. *Eur. J. Heart Fail.* **14**, 1199–1207 (2012).

149. Du, Y. *et al.* Downregulation of neuronal sodium channel subunits Nav1.1 and Nav1.6 in the sinoatrial node from volume-overloaded heart failure rat. *Pflugers Arch. Eur. J. Physiol.* **454**, 451–459 (2007).

150. Dupont, E. *et al.* Altered connexin expression in human congestive heart failure. *J. Mol. Cell. Cardiol.* **33**, 359–371 (2001).

151. Li, G. *et al.* Differential Wnt-mediated programming and arrhythmogenesis in right versus left ventricles. *J. Mol. Cell. Cardiol.* **123**, 92–107 (2018).

152. Fu, X. *et al.* Segmentation of histological images and fibrosis identification with a convolutional neural network. *Comput. Biol. Med.* **98**, 147–158 (2018).

153. Achanta, R. *et al.* SLIC superpixels compared to state-of-the-art superpixel methods. *IEEE Trans. Pattern Anal. Mach. Intell.* **34**, 2274–2281 (2012).

154. Lloyd, S. P. Least Squares Quantization in PCM. *IEEE Trans. Inf. Theory* **28**, 129–137 (1982).

155. Baldevbhai, P. J. Color Image Segmentation for Medical Images using L*a*b* Color Space. *IOSR Journal of Electronics and Communication Engineering* vol. 1 www.iosrjournals.orgwww.iosrjournals.org (2012).

156. Wong, J. *et al.* High-Resolution, Small Animal Radiation Research Platform With X-Ray Tomographic Guidance Capabilities. *Int. J. Radiat. Oncol. Biol. Phys.* **71**, 1591–1599 (2008).

157. Laughner, J. I., Ng, F. S., Sulkin, M. S., Martin Arthur, R. & Efimov, I. R. Processing and analysis of cardiac optical mapping data obtained with potentiometric dyes. *American Journal of Physiology - Heart and Circulatory Physiology* vol. 303 H753 (2012).

158. Dobin, A. *et al.* STAR: Ultrafast universal RNA-seq aligner. *Bioinformatics* **29**, 15–21 (2013).

159. Patro, R., Duggal, G., Love, M. I., Irizarry, R. A. & Kingsford, C. Salmon provides fast and bias-aware quantification of transcript expression. *Nat. Methods* **14**, 417–419 (2017).

160. Robinson, M. D., McCarthy, D. J. & Smyth, G. K. edgeR: A Bioconductor package for differential expression analysis of digital gene expression data. *Bioinformatics* **26**, 139–140 (2009).

161. Ritchie, M. E. *et al.* Limma powers differential expression analyses for RNA-sequencing and microarray studies. *Nucleic Acids Res.* **43**, e47 (2015).

162. Subramanian, A. *et al.* Gene set enrichment analysis: A knowledge-based approach for interpreting genome-wide expression profiles. *Proc. Natl. Acad. Sci. U. S. A.* **102**, 15545–15550 (2005).

163. Liberzon, A. *et al.* The Molecular Signatures Database Hallmark Gene Set Collection. *Cell Syst.* **1**, 417–425 (2015).

164. Corces, M. R. *et al.* An improved ATAC-seq protocol reduces background and enables

interrogation of frozen tissues. *Nat. Methods* **14**, 959–962 (2017).

165. Buenrostro, J. D., Wu, B., Chang, H. Y. & Greenleaf, W. J. ATAC-seq: A method for assaying chromatin accessibility genome-wide. *Curr. Protoc. Mol. Biol.* **2015**, 21.29.1-21.29.9 (2015).

166. Severs, N. J. *et al.* Gap junction alterations in human cardiac disease. *Cardiovasc. Res.* **62**, 368–377 (2004).

167. Motloch, L. J. *et al.* Increased Afterload Following Myocardial Infarction Promotes Conduction-Dependent Arrhythmias That Are Unmasked by Hypokalemia. *JACC Basic to Transl. Sci.* **2**, 258–269 (2017).

168. Coronel, R. *et al.* Cardiac expression of skeletal muscle sodium channels increases longitudinal conduction velocity in the canine 1-week myocardial infarction. *Hear. Rhythm* **7**, 1104–1110 (2010).

169. Kucera, J. P., Rohr, S. & Rudy, Y. Localization of sodium channels in intercalated disks modulates cardiac conduction. *Circ. Res.* **91**, 1176–1182 (2002).

170. Shaw, R. M. & Rudy, Y. Ionic mechanisms of propagation in cardiac tissue: Roles of the sodium and L-type calcium currents during reduced excitability and decreased gap junction coupling. *Circ. Res.* **81**, 727–741 (1997).

171. Qin, D. *et al.* Cellular and ionic basis of arrhythmias in postinfarction remodeled ventricular myocardium. *Circ. Res.* **79**, 461–473 (1996).

172. Nerbonne, J. M., Nichols, C. G., Schwarz, T. L. & Escande, D. Genetic manipulation of cardiac K+ channel function in mice: What have we learned, and where do we go from here? *Circ. Res.* **89**, 944–956 (2001).

173. Sanders, J. T. *et al.* Radiation-induced DNA damage and repair effects on 3D genome organization. *Nat. Commun.* **11**, (2020).

174. Zhang, D. M. *et al.* Cardiac radiotherapy induces electrical conduction reprogramming in the absence of transmural fibrosis. *Nat. Commun.* **12**, 5558 (2021).**

175. Kim, J. S. *et al.* Impact of high-dose irradiation on human ipsc-derived cardiomyocytes using multi-electrode arrays: Implications for the antiarrhythmic effects of cardiac radioablation. *Int. J. Mol. Sci.* **23**, 351 (2022).

**Certain texts and figures within this dissertation are adapted from a review published in 2021 in *Clinical Oncology*[8] and a research article published in 2021 in *Nature Communications*[174]. (CC by 4.0)

Zhang DM, Szymanski J, Bergom C, Cuculich PS, Robinson CG, Schwarz JK, Rentschler SL. Leveraging Radiobiology for Arrhythmia Management: A New Treatment Paradigm? *Clin Oncol (R Coll Radiol)*. 2021 Nov;33(11):723-734.

D.M.Z performed the literature review, wrote the manuscript, and generated all figures. All other authors provided additional perspective and editorial comments.

Zhang DM, Navara R, Yin T, Szymanski J, Goldsztejn U, Kenkel C, Lang A, Mpoy C, Lipovsky CE, Qiao Y, Hicks S, Li G, Moore KMS, Bergom C, Rogers BE, Robinson CG, Cuculich PS, Schwarz JK, Rentschler SL. Cardiac radiotherapy induces electrical conduction reprogramming in the absence of transmural fibrosis. *Nat Commun*. 2021 Sep 24;12(1):5558. (CC by 4.0)

D.M.Z. performed optical mapping experiments, collected and interpreted murine electrocardiograms, collected tissue, extracted RNA and protein lysates, performed immunohistochemistry, immunoblotting, and colorimetric assays, conducted immunohistochemical staining, analyzed data, generated figures, and wrote the initial draft. R.N. and P.S.C. interpreted patient electrocardiograms. T.Y., and C.K. performed and imaged histology. J.S. generated RNA-sequencing figures. U.G. performed image-segmented pathology analysis. A.L. interpreted pathology. C.M and B.E.R irradiated murine hearts. C.E.L. and S.H. coordinated mouse breedings. Q.Y. and G.L. performed iNICD mouse optical mapping. K.M.S.M. coordinated the ENCORE-VT clinical trial. C.B., J.K.S., and S.L.R. interpreted data, and provided scientific feedback. C.G.R. and P.S.C. planned patient treatments, interpreted data, and provided feedback.

Curriculum Vitae

DAVID MENG ZHANG

508-471-6734 | davidzhang@wustl.edu

EDUCATION

2016-24	M.D. Candidate **Washington University School of Medicine**, Saint Louis, MO	
2016-24	Ph.D. Candidate in Molecular Cell Biology Thesis Advisor: Stacey Rentschler, M.D., Ph.D. **Washington University School of Medicine**, Saint Louis, MO	
2012-16	B.S.E. in Bioengineering, *summa cum laude* **University of Pennsylvania**, Philadelphia, PA	GPA: 3.95/4.00

AWARDS & HONORS

2019-22	T32 HL134635, Integrative and Systems Biology of Cardiovascular Disease Pre-Doctoral Training Fellowship, Washington University
2016	*summa cum laude* Latin Honors, University of Pennsylvania
2016	Exceptional Service Award, University of Pennsylvania
2016	SEAS Senior Design Competition Honorable Mention, University of Pennsylvania
2016	Bioengineering Senior Design Award, University of Pennsylvania
2015	Abraham Noordergraaf Research Fellowship, University of Pennsylvania
2014	Class of 1971 Robert J. Holtz Research Fellowship, University of Pennsylvania
2014	Tau Beta Pi Engineering Honor Society, University of Pennsylvania
2012-16	Dean's List, University of Pennsylvania

PEER-REVIEWED PUBLICATIONS

1. **Zhang DM**, Navara R, Yin T, Szymanski J, Goldsztejn U, Kenkel C, Lang A, Mpoy C, Lipovsky CE, Qiao Y, Hicks S, Li G, Moore KMS, Bergom C, Rogers BE, Robinson CG, Cuculich PS, Schwarz JK, Rentschler SL. Cardiac radiotherapy induces electrical conduction reprogramming in the absence of transmural fibrosis. *Nature Communications*, 2021; 12: 5558. PMID: 34561429
2. **Zhang DM**, Szymanski J, Bergom C, Cuculich PS, Robinson CG, Schwarz J, Rentschler SL. Leveraging radiobiology for arrhythmia management: A new treatment paradigm? *Clinical Oncology*, 2021; **33**: 723-734. PMID: 34535357
3. Lipovsky CE, Jimenez J, Guo Q, Li G, Yin T, Hicks SC, Bhatnagar S, Takahashi K, **Zhang DM**, Brumback BD, Goldsztejn U, Naddur RD, Perez-Cervantez C, Moskowitz IP, Liu S, Zhang B, Rentschler SL. Chamber-specific transcriptional responses in atrial fibrillation. *Journal of Clinical Investigation – Insight*, 2020; 5(18):e135319. PMID: 32841220
4. Bartoli CR, **Zhang DM**, Hennessy-Strahs S, Kang J, Restle DJ, Bermudez CA, Atluri P, Acker MA. Clinical and *in vitro* evidence that LVAD-induced von Willebrand factor degradation alters angiogenesis. *Circulation: Heart Failure,* 2018; 11(9)e004638. PMID: 30354363
5. Bartoli CR, **Zhang D**, Kang J, Hennessy-Strahs S, Restle D, Howard J, Redline G, Bermudez CA, Atluri P, Acker MA. Clinical and *in vitro* evidence that LVAD-associated hemolysis contributes to LVAD thrombosis. *The Annals of Thoracic Surgery*, 2018; 105(3): 807-814. PMID: 28942075
6. Bartoli CR, Kang J, **Zhang D**, Howard JL, Acker MA, Atluri P, Motomura T. Left ventricular assist device design reduces von Willebrand factor degradation: A comparative study between the

HeartMate II and EVAHEART Left Ventricular Assist System. *The Annals of Thoracic Surgery*, 2017; 103(4): 1239-1244. PMID: 27717422

7. Kang J, **Zhang DM**, Restle DJ, Kallel F, Acker MA, Atluri P, Bartoli CR. Reduced continuous-flow left ventricular assist device speed does not decrease von Willebrand factor degradation. *The Journal of Thoracic and Cardiovascular Surgery*, 2016; 151(6): 1747-1754. PMID: 26971377
8. Bartoli CR, Kang J, Restle DJ, **Zhang DM**, Shabahang CR, Acker MA, Atluri P. Inhibition of ADAMTS-13 by doxycycline reduces von Willebrand factor degradation during supraphysiologic shear stress: therapeutic implication for LVAD-associated bleeding. *Journal of The American College of Cardiology: Heart Failure*, 2015; 3(11): 860-869. PMID: 26454844
9. Bartoli CR, Restle DJ, **Zhang DM**, Acker MA, Atluri P. Pathologic von Willebrand factor degradation with a left ventricular assist device occurs via two distinct mechanisms: mechanical demolition and mechanoenzymatic cleavage. *The Journal of Thoracic and Cardiovascular Surgery*, 2015; 149(1): 281-289. PMID: 25439775
10. Restle DJ, **Zhang DM**, Hung G, Howard JL, Kallel F, Acker MA, Atluri P, Bartoli CR. Preclinical models for translational investigations of LVAD-associated von Willebrand factor degradation and blood trauma *Artificial Organs*, 2015; 39(7): 569-575. PMID: 25810063
11. Li G, Brumback BD, Huang L, **Zhang DM**, Yin T, Lipovsky CE, Hicks SC, Jimenez J, Boyle PM, Rentschler SL. Acute glycogen synthase kinase 3 inhibition modulates the human cardiac electrical substrate. *Journal of The American College of Cardiology: Basic to Translational Science*. In Press (Accepted).
12. Brumback BD, Dmytrenko O, Robinson AN, Bailey AL, Ma P, Liu J, Hicks S, Ng S, Li G, **Zhang DM**, Lipovsky CE, Lin C, Diamond MS, Lavine K, Rentschler SL. Human cardiac pericytes are susceptible to SARS-CoV-2 infection. In revision.

Google Scholar Page

CONFERENCE PRESENTATIONS & ABSTRACTS

1. Brumback BD, Li G, Hicks S, Jimenez J, **Zhang D**, Lipovsky C, Bailey A, Diamond MS, Kashentseva E, Curiel D, Rentschler SL. Human organotypic cardiac slices as a translational platform for studying viral tropism. *Biomedical Engineering Society 2020 Conference*. Digital Conference, October 2020.
2. **Zhang DM**, Goldsztejn U, Yin T, Lang A, Szymanski J, Kenkel C, Mpoy C, Rogers B, Robinson C, Cuculich P, Schwarz J, Rentschler SL. Electrical substrate remodeling underlies the anti-arrhythmic effects of cardiac radioablation. *Heart Rhythm Scientific Sessions 2020*. San Diego, CA, USA, May 2020.
3. Hennessy-Strahs S, **Zhang DM**, Kang J, Krause E, Redline G, Howard J, Acker MA, Atluri P, Bermudez C, Bartoli CR. Plasma free hemoglobin activates platelets and protects von Willebrand factor from degradation: Clinical and in vitro evidence that LVAD-associated hemolysis contributes to LVAD thrombosis. *Proceedings of the International Society of Heart and Lung Transplantation*. San Diego, CA, April 2017.
4. Bartoli CR, **Zhang D**, Kang J, Restle D. Kwiatkowski P, Bermudez C, Acker M, Atluri P, McConnell P. LVAD-associated von Willebrand factor degradation fragments alter angiogenesis: A mechanistic link between LVAD support, gastrointestinal angiodysplasia, and bleeding? *American College of Cardiology 66th Annual Scientific Sessions*. Washington, D.C., March 2017.
5. Bartoli CR, **Zhang DM**, Kang J, Restle DJ, Redline G, Howard J, Bermudez C, Acker MA, Atluri P. Clinical and in vitro evidence that LVAD-associated hemolysis contributes to LVAD thrombosis. *Annual Congress of the Society of Thoracic Surgeons*. Houston, TX, January 2017.

6. Maidment ADA, Acciavatti RJ, Vent TL, Conant E, Kwon YJ, Ng S, Kuo J, Ringer PA, Maidment T, Wurtele D, Licata J, Narayan T, **Zhang D**, Higgenbotham D. Construction of a prototype digital breast tomosynthesis system with superior spatial resolution. *Congress of the Radiological Society of North America (RSNA Phys. Basic. Sci.)*. Chicago, IL, November 2016.
7. Bartoli CR, **Zhang DM**, Kang J, Restle DJ, Kwiatkowski P, Bermudez CA, Acker MA, Atluri P, McConnell P. LVAD-associated von Willebrand factor degradation fragments are the mechanistic link between LVAD support and gastrointestinal angiodysplasia. *Annual Congress of the International Society for Rotary Blood Pumps*. Mito, Japan, September 2016.
8. Bartoli CR, Kang J, **Zhang DM**, Acker MA, Atluri P, Motomura T. Reduced LVAD speed decreases von Willebrand factor degradation with the EVAHEART LVAS but not with the HeartMate II: Implications for clinical operation of continuous-flow LVADs. *Annual Congress of the International Society for Rotary Blood Pumps*. Mito, Japan, September 2016.
9. **Zhang DM**, Kang J, Redline G, Howard J, Acker MA, Atluri P, Bartoli CR. Elevated preoperative plasma free hemoglobin and hemin may predict LVAD thrombosis. *Proceedings of the International Society of Heart and Lung Transplantation*. Washington, D.C., April 2016.
10. **Zhang DM**, Kang J, Redline G, Howard J, Acker MA, Atluri P, Bartoli CR. LVAD support increases plasma iron species: Implications for a pathophysiologic relationship between LVAD-associated hemolysis and thrombosis? *Proceedings of the International Society of Heart and Lung Transplantation*. Washington, D.C., April 2016.
11. Kang J, **Zhang D**, Motomura T, Acker MA, Atluri P, Bartoli CR. LVAD Device Design Features and Operational Settings Minimize von Willebrand Factor Degradation. *Proceedings of the International Society of Heart and Lung Transplantation*. Washington, D.C., April 2016.
12. Kang J, **Zhang DM**, Restle DJ, Kallel F, Acker MA, Atluri P, Bartoli CR. Reduced continuous-flow LVAD speed does not decrease von Willebrand factor degradation. *Annual Congress of the International Society for Rotary Blood Pumps*. Dubrovnik, Croatia, September 2015.
13. Kang J, **Zhang DM**, Motomura T, Acker MA, Atluri P, Bartoli CR. Centrifugal-flow LVADs cause less von Willebrand factor degradation than axial-flow LVADs. *Annual Congress of the International Society for Rotary Blood Pumps*. Dubrovnik, Croatia, September 2015.
14. **Zhang DM**, Kang J, Restle DJ, Acker MA, Atluri P, Bartoli CR. LVAD-associated von Willebrand factor degradation alters angiogenesis: a mechanistic link between LVAD support, gastrointestinal angiodysplasia, and bleeding? *Proceedings of the International Society of Heart and Lung Transplantation*. Nice, France, April 2015.
15. Kang J, **Zhang DM**, Restle DJ, Kallel F, Acker MA, Atluri P, Bartoli CR. Reduced continuous-flow LVAD speed does not decrease von Willebrand factor degradation. *Proceedings of the International Society of Heart and Lung Transplantation*. Nice, France, April 2015.
16. **Zhang DM**, Restle DJ, Kang J, Shabahang CR, Acker MA, Atluri P, Bartoli CR. LVAD support alters endothelial cell behavior: Potential implications for LVAD-associated bleeding? *Annual Congress of the International Society for Rotary Blood Pumps*. San Francisco, CA, September 2014.
17. Restle DJ, **Zhang DM**, Shabahang CR, Kang J, Acker MA, Atluri P, Bartoli CR. Novel in vitro models of human blood trauma demonstrate mechanisms of LVAD-associated von Willebrand factor degradation: Shear stress and enzymatic cleavage. *Annual Congress of the International Society for Rotary Blood Pumps*. San Francisco, CA, September 2014.
18. Bartoli CR, Restle DJ, Shabahang CR, Kang J, **Zhang DM**, Acker MA, Atluri P. Inhibition of ADAMTS-13 with Doxycycline may reduce von Willebrand factor degradation during LVAD support: In vitro findings with potential clinical implications. *Annual Congress of the International Society for Rotary Blood Pumps*. San Francisco, CA, September 2014.

INVITED TALKS

1. Cardiac radiotherapy induces electrical substrate reprogramming in the absence of transmural fibrosis. SNORAD (Symposium for Noninvasive Radioablation) and STOPSTORM (Standardized Treatment and Outcome Platform for Stereotactic Therapy Of Re-entry tachycardia by a Multidisciplinary consortium) joint SNOSTORM Mini-Symposium on Radioablation for Ventricular Tachycardia. April 2022.

EXPERIENCES & POSITIONS

2019-21	BioSURF Research Mentor, Washington University, Saint Louis, MO
2014-16	Advisory Board, UPenn Center for Research and Fellowships, Philadelphia, PA
2014-15	Preceptorship in Clinical Bioengineering, Design Engineer, Hospital of the University of Pennsylvania, Philadelphia, PA
2014	Prosthetics Technician Trainee, Hong Kong Polytechnic University, Hong Kong
2013-16	Undergraduate Researcher, University of Pennsylvania, Philadelphia, PA
2013-15	Robotics Coach, Freire Charter School, Philadelphia PA
2013-14	Research Technician, Sicinski Lab, Dana-Farber Cancer Institute, Boston, MA

TEACHING

2018-19	ME 75: Medical School Physiology, Assistant Instructor, Washington University School of Medicine, Saint Louis, MO
2015	BE 301: Bioengineering Signals and Systems, Teaching Assistant, University of Pennsylvania, Philadelphia, PA
2015-16	Undergraduate Satellite Tutor, University of Pennsylvania, Philadelphia, PA
2014-16	CHEM 241/242 Organic Chemistry Peer Tutor, University of Pennsylvania, Philadelphia, PA
2013-16	PHYS 150/151: Engineering Physics Peer Tutor, University of Pennsylvania, Philadelphia, PA

ACADEMIC MENTORSHIPS

Undergraduate Student:	*Last Known Position:*
Camryn Kenkel (2018-2021)	Medical Student, New York U. Grossman SOM

SKILLS

Lab Skills	Optical mapping, sharp microelectrode, flow cytometry, next-generation sequencing (RNA-seq, ATAC-seq, CUT&RUN, CUT&TAG), immunofluorescence and RNA *in situ* hybridization, microscopy, immunoblotting, spectrophotometry, miRNA and RNAi, human cardiac organotypic slice culture, cell culture, transgenic mouse models
Software	Python, MATLAB, C#, Java, ImageJ, SolidWorks, LabChart, Adobe Illustrator, GraphPad Prism, SPSS Statistics